2013

Real-time Expulsion Detection and Characterization in Ultrasound M-scans of the Resistance Spot Welding Process

Anthony C. Karloff

Recommended Citation

Karloff, Anthony C., "Real-time Expulsion Detection and Characterization in Ultrasound M-scans of the Resistance Spot Welding Process" (2013). *Electronic Theses and Dissertations.* Paper 4735.

Real-time Expulsion Detection and Characterization in Ultrasound M-scans of the Resistance Spot Welding Process

by

Anthony C. Karloff

A Dissertation
Submitted to the Faculty of Graduate Studies through
Electrical and Computer Engineering in Partial Fulfillment
of the Requirements for the Degree of Doctor of Philosophy at the
University of Windsor

Windsor, Ontario, Canada
2012

Real-time Expulsion Detection and Characterization in Ultrasound M-scans of the Resistance Spot Welding Process

by

Anthony C. Karloff

APPROVED BY:

Dr. W. Kedzierski
Department of Physics

Dr. J. Wu
Department of Electrical and Computer Engineering

Dr. M. Ahmadi
Department of Electrical and Computer Engineering

Dr. R. Gr. Maev, Advisor
Department of Electrical and Computer Engineering, Physics

Dr. J. Saniie, Outside Reader
Illinois Institute of Technology

18 January, 2013

Declaration of Co-Authorship/Previous Publication

I. Co-Authorship Declaration

This dissertation has build upon joint research undertaken in collaboration with Dr. Chertov who worked on the development of the Inline ultrasound system that is used in this work. The focus of this thesis is to utilize this device in a new and novel way for the detection of expulsions, which is outside the scope of Dr. Chertov's contributions and is the individual work of the author.

I am aware of the University of Windsor Senate Policy on Authorship and I certify that I have properly acknowledged the contribution of other researchers to my thesis, and have obtained written permission from each of the co-author(s) to include the above material(s) in my thesis.

I certify that, with the above qualification, this dissertation, and the research to which it refers, is the product of my own work.

II. Declaration of Previous Publication

This thesis includes four original conference papers that have been presented and published in proceedings as follows:

Thesis Chapter	**Full Citation**	**Status**
Chapter 3,4	A.C.Karloff, A.M. Chertov and R.Gr. Maev. Real-Time Ultrasonic Expulsion Detection and Indentation Measurement in Resistance Spot Welds, QNDE review of Progress in Quantitative NDE, July 2009	Published
Chapter 1	A.C. Karloff, A.M. Chertov, J. Kocimski, P. Kustron, R.Gr. Maev, New developments for in situ ultrasonic measurement of transient temperature distributions at the tip of a copper resistance spot weld electrode, IEEE International Ultrasonics Symposium, Oct. 2010	Published
Chapter 4	A.C. Karloff, A.M. Chertov, R.Gr. Maev. Enhancing real-time ultrasound signatures of molten nugget growth for quality evaluation of resistance spot welds, IEEE International Ultrasonics Symposium, Oct 2009	Published
Chapter 3,	A.C. Karloff, A.M. Chertov and R.Gr. Maev, Detection of Discontinuities in Contact Pressure Between Rough Surfaces, IEEE International Ultrasonics Symposium, Oct 2011	Published

I certify that I have obtained a written permission from the copyright owner(s) to include the above published material(s) in my dissertation. I certify that the above material describes work completed during my registration as graduate student at the University of Windsor.

I declare that, to the best of my knowledge, my dissertation does not infringe upon anyone's copyright nor violate any proprietary rights and that any ideas, techniques, quotations, or any other material from the work of other people included in my dissertation, published or otherwise, are fully acknowledged in accordance with the standard referencing practices. Furthermore, to the extent that I have included copyrighted material that surpasses the bounds of fair dealing within the meaning of the Canada Copyright Act, I certify that I have obtained a written permission from the copyright owner(s) to include such material(s) in my thesis.

I declare that this is a true copy of my dissertation, including any final revisions, as approved by my dissertation committee and the Graduate Studies office, and that this dissertation has not been submitted for a higher degree to any other University of Institution.

Abstract

In this work, ultrasound is used as a non-destructive method of monitoring the welding process in real-time to detect expulsion events. During spot welding, a single element ultrasound transducer placed behind one of the welding electrodes operates in pulse-echo mode and probes the axial center of the welded zone. Acoustic reflections from the electrodes, plate interfaces and liquid metal weld nugget are recorded as A-scans. During welding, the A-Scan reflections change with time, since the material properties of steel (e.g. density and elasticity) change with temperature. Imaging successive A-scans in time forms an M-Scan image of the welding process from which the dynamic formation of the spot weld can be depicted and analyzed.

This thesis focuses on taking a brand new approach to the problem of expulsion detection by identifying and characterizing expulsion events in M-scan data. Expulsion occurs when molten material is ejected from the welded zone as a result of overheating due to: poor electrical/thermal contact, coating thickness and/or excessive weld current. An expulsion can have a significant impact on the final yield strength of the weld, and thus the detection and characterization of expulsion events is significant to the quality assurance of resulting spot welds.

The main contribution of this work was the discovery of M-scan features that provide a means of detecting, predicting and classifying the event. These include:

1) Detection by sudden phase delay change of the workpiece surface reflection.

2) Prediction by ultrasonically measuring the heating rate prior to expulsion.

3) Classification of the weld quality by ultrasonically measuring indentation in the heated workpiece.

In addition, new methods for automatically detecting and measuring these features were developed that utilize a new efficient Hough transform variant proposed in this work.

It was shown using both lab experiments and industrial data that not only does the automatic detection of these features provide a new and robust means of identifying expulsions in a wide range of welding setups, but this research can also be used in the future to provide real-time feedback to dynamic weld controllers and eliminate expulsions from occurring altogether.

To Theresa, for always being there for me.

Acknowledgments

There are many people who deserve to be acknowledged for their contributions to this project and my personal development as a graduate student.

I would first like to express my sincere gratitude and appreciation to Dr. Roman Gr. Maev, my supervisor, for making this work possible. He has been the principal figure throughout my PhD research from formulating the problem, setting strategies and milestones to helping me reach personal research goals, making conference travel and networking possible and particularly for providing a team and environment supportive for completing this work. I would also like to thank Dr. Andrey Chertov, the resident expert for the Inline ultrasound project, for his invaluable guidance and involvement throughout the course of this research. My work would also not have been possible without the assistance of the rest of the Inline welding group: Waldo Perez, Janusz Kocimski, Pawel Kustron and Anthony Lui.

I would also like to acknowledge my fellow collegues for the wealth of knowledge they shared, particularly Dmitry Gavrilov for his expertise in heat transfer and thermography. Jeff Sadler for checking my mathematical formatting and making Maple work when need. Sarah Beneteau for assistance proof reading. Also, Tessonics Inc.

and the helpful staff for providing access to Chrysler and Mini Cooper data and materials.

I would also like to extend a very special thanks to my committee, Dr. Majid Ahmadi, Dr. Johnathan Wu, Dr. Wladislaw Kedzierski and Dr. Jafar Saniie for their feedback during my seminars and in the process of writing this dissertation.

Finally, I would like to express a special thanks to Dr. Roberto Muscedere for his mentor ship and especially Dr. Maher Sid-Ahmed for his guidance, encouragement and constant support throughout my graduate studies.

Contents

List of Figures

List of Tables

List of Abbreviations

2T	Two Thickness (two metal sheets)
3T	Threes Thickness (three metal sheets)
ASIC	Application Specific Integrated Circuit
EM	Electromagnetic
FFT	Fast Fourier Transform
FIR	Finite Impulse Response
FPGA	Field Programmable Gate Array
GA	Galvannealed
GC	Gaussian Chirplet
GI	Galvanized Iron
HAZ	Heat Affected Zone
HDG(I)	Hot Dipped Galvanized (Iron)
HSLA	High Strength Low Alloy
HSS	High Strength Steel
LOTS	Law of Thermal Similarity
MP	Matching Pursuit
PRF	Pulse Repetition Frequency
PRR	Pulse Repetition Rate
RF	Radio Frequency
RIWA	Real-time Integrated Weld Analyzer
RSW	Resistance Spot Welding
SAM	Scanning Acoustic Microscope
SNR	Signal to Noise Ratio
TOF	Time of Flight

List of Symbols

Symbol	Description	Units
γ	adiabatic index	-
κ_s	curvature of asperity peaks	-
η_s	density of asperity peaks	-
ω	frequency	(radians)
ρ	Hough transform parameter	-
ρ_m	material density	$(\mathrm{kg \cdot m^{-3}})$
σ_s	standard deviation of peaks	-
σ_{wp}	workpiece conductivity	$(\Omega \cdot \mathrm{m}^{-1})$
θ	angle	(degrees)
$\boldsymbol{\theta}$	Gaussian Chirplet parameter vector	-
$\theta(f)$	spectrum phase shift	(radians)
θ_c	center frequency phase delay	(radians)
a	attenuation parameter	-
a_m	reflection amplitude	-
A, B, C, D	scalar parameters for a current density model	-
$A(f)$	frequency amplitude attenuation	(dB)
A_{e}	electrode contact area	(m^2)
c	wave velocity	$(\mathrm{m \cdot s^{-1}})$
c_{yx}	cross-correlation of y and x	-
c_{yx}^a	analytic cross-correlation	-
c_p	specific heat capacity	$(\mathrm{J \cdot\ kg^{-1} K^{-1}})$
C_p	heat capacity	$(\mathrm{J \cdot K^{-1}})$
d	distance	(m)
d_1	nugget diameter	(m)

d_2	nugget thickness	(m)
d_3	nugget penetration depth (bottom)	(m)
d_4	nugget penetration depth (top)	(m)
d_{e}	electrode tip diameter	(m)
d_{ind1}	indentation depth (top)	(m)
d_{ind2}	indentation depth (bottom)	(m)
d_{wp}	workpiece thickness	(m)
$e(t)$	noise	-
E^*	plane strain reduced modulus	-
f	frequency	(Hz)
f_c	center frequency	(Hz)
f_p	pulse repetition frequency	(Hz)
f_s	sampling frequency	(Hz)
G	material shear modulus	(Pa)
h_c	thermal conductivity coefficient	($\mathrm{W{\cdot}m^{-2}K^{-1}}$)
$h_{\mathrm{em}}(t)$	transducer transfer characteristic	-
$h(t)$	ultrasound system response	-
$H(f)$	transfer characteristic	-
H_{rx}	transducer transfer characteristic	-
H_{tx}	same as H_{rx}	-
I_{weld}	welding current	(A)
J	current density	($\mathrm{A{\cdot}m^{-2}}$)
j	complex number	-
k	discrete frequency index	-
k_v	linear temperature dependent co-efficient	-
K	material bulk modulus	(Pa)
K_T	isothermal bulk modulus	-
m	mass	(kg)
M	arbitrary constant	-
M_{E}	material elastic modulus	(Pa)
n	discrete time index	-
N	arbitrary constant	-
p	sound pressure	(Pa)
$p(n)$	depth dependent attenuation factor	(dB)
p_{nom}	nominal pressure	(Pa)
q_{loss}	heat flux through the electrode	($\mathrm{W{\cdot}m^{-2}}$)
Q	heat energy	(J)
Q_{weld}	heat energy developed during welding	(J)
r	radial distance	(m)
R_{weld}	resistance of workpiece	(Ω)

R_{12}	acoustic pressure reflection index	-
S	surface area	(m^2)
t_m	reflection delay	(s)
T	temperature	(K)
T_0	initial temperature	(K)
T_{melt}	melting temperature	(K)
T_{12}	acoustic pressure transmission index	-
t	time	(s)
t_θ	phase delay	(s)
t_d	time delay	(s)
t_e	time of expulsion	(s)
t_g	group delay	(s)
t_k	discrete time	-
tof	time of flight	(s)
t_p	pulse repetition interval	(s)
t_s	sampling period	(s)
t_{weld}	total welding time	(s)
u	acoustic displacement	(m)
v	particle velocity	$(\mathrm{m{\cdot}s^{-1}})$
$v_i(t)$	input voltage waveform	(V)
$v_o(t)$	output voltage waveform	(V)
$x(t)$	ultrasound input signal	-
$x_{\mathrm{a}}(t)$	analytic signal	-
$X(f)$	spectrum of $x(t)$	-
$y(t)$	reflected ultrasound signal	-
$Y(f)$	spectrum of $y(t)$	-
Z	specific acoustic impedance	(rayl)

Chapter 1

Background Theory

1.1 Introduction

Resistance spot welding is still one of the most widely used methods of joining metal parts, particularly for the automotive industry that relies heavily on spot welding. A typical car frame has around 3000 to 4000 welds and this number is not expected to change in the near future[1]. In other areas of industry, new applications for spot welding are continuing to emerge. For instance, the construction of structural H-beams from stamped sheet metal is turning to spot welding over rivets, since spot welds can reduce the fabrication cost and improve the strength over the lifetime of these parts. Although spot welding is traditionally used for joining steel plates, research into welding high strength alloys, magnesium alloys, aluminum, and even stacks of mixed materials is ongoing as these materials are being introduced into vehicles and other structures [2, 3]. Of particular interest is the reliable welding of aluminum for aerospace applications and in particular the joining of aluminum to high strength steels for automotive, aerospace and military applications. Despite its long history, resistance spot welding is still an active area of research, particularly in the area of real-time quality control and feedback of the process.

To date, the general method of resistance spot welding remains the same, however faster electronics, intelligent feedback systems and robotic automation of the process has provided a vast palette of tools to improve the quality and reliability of spot welds, especially in the new areas for welding listed above. On the forefront of welding research are methods for monitoring and evaluating the welding process to provide necessary feed-back that ensures high quality welds are made. This is especially true for welding scenarios typically seen as difficult. The two main areas that assure welding quality involve:

1. Development of a suitable welding setup and schedule.
2. Destructive or non-destructive evaluation of the resulting welds.

The primary goal of each area is to assure that each weld has a sufficiently high yield strength with no defects. In a good welding setup, good welds can be reliably produced with minimal degradation over time, as welding repeatedly tends to degrade weld quality due to wear on the equipment. In this case, periodic destructive or non-destructive testing is sufficient to ensure the process is stable and good welds are being produced. With newer materials being welded in shorter times and in harsher manufacturing environments, the consistency between welds is dramatically reduced resulting in an increased uncertainty of each weld's quality. Thus, the periodic testing of welds can no longer ensure each welds quality and so complete real-time inspection of every weld is a topic of high interest.

One particular indicator of a problem in a welding setup is the occurrence of an expulsion during welding. In brief, an expulsion is an undesired event in which a portion of molten metal is ejected from the weld. In most industries expulsions are highly undesired as they affect both the quality and aesthetics of a weld. An expulsion can also have potentially damaging effects on the welding equipment. The detection of expulsions, and especially a means of preventing them, is a highly desirable feature of state-of-the-art welding equipment from major welding equipment providers such as Bosch and Kuka. Yet there is still much room for improvement in these devices, especially for the many, diverse applications for spot welding.

The topic of this dissertation has a role in both the development of welding schedules and quality monitoring of the process, however, the focus is on the later. Using a novel inline ultrasound device (referred to as Inline), quality monitoring of welding takes place *in-process* and performs direct measurements inside the welded zone for every weld. The information collected during welding provides a wealth of knowledge regarding heat generation and material interaction unattainable by any other methods to date. For the purpose of this research, the extracted information is specifically used to predict and detect expulsion events. Expulsion is generally undesired; it is a strong indicator of a problem in the welding setup and can result in weak or undersized welds. Expulsion events may also cause the ultrasonic information gathered from good welds, to appear as bad ones. Although a number of methods of expulsion detection exist to date, it will be shown that the unique data gathered ultrasonically can provide not only a greater understanding of the mechanisms and root causes of expulsion, but a more reliable way to detect and classify the type of expulsion event. In future work, this can aid in the development of welding schedules, provide a method for in-process non-destructive quality monitoring and even be used for real-time dynamic control during welding.

1.2 Overview

In this chapter the basic principals of welding and the relevance of expulsion detection in the welding process are discussed. Using this understanding, the next chapters will outline how knowledge of the welding process combined with real-time ultrasonic monitoring, can provide a suitable solution to the problem of expulsion prediction, detection and classification. The remainder of this work is divided as follows:

In Chapter 2, the Inline ultrasound setup is explained, particularly the acoustic properties of the various interfaces and the expected properties of the reflected signal during the various stages of welding.

Chapter 3 presents the details of expulsion detection using the Inline system. This chapter presents four novel methods unique only to ultrasound inspection. The general algorithms and real-time requirements are presented.

Chapter 4 covers the details of both novel and existing ultrasound image and signal processing techniques used in the algorithms of Chapter 3. This includes: Noise reduction and filtering, spare decomposition of ultrasound echoes, a novel real-time hough transform technique for interface tracking and a unique approach to the detection of weak interfaces.

Finally, Chapter 5 presents the experimental testing and verification of the methods presented in this work, focusing on the various algorithms of Chapter 3. This chapter also summarizes the contributions of this work and more importantly discusses the new future research that is now possible as a result of this dissertation.

1.3 The Resistance Spot Welding Process

In resistance spot welding, heat is generated by passing high electrical current through a stack of metal plates called a stack-up or workpiece. The workpiece is squeezed together between two copper electrodes at a force of (500-7500) kN and welding current is passed through the plates on the order of (5-50) kA, depending on the materials being welded. The applied current is AC, DC or a train of impulses depending on the setup and desired weld properties, and typical welding time for steel is (0.1-0.63) s.

Figure 1.1 shows a schematic cross section of a welding setup for two plates: a) before current is applied, b) during the formation of the weld nugget and c) after the weld has cooled.

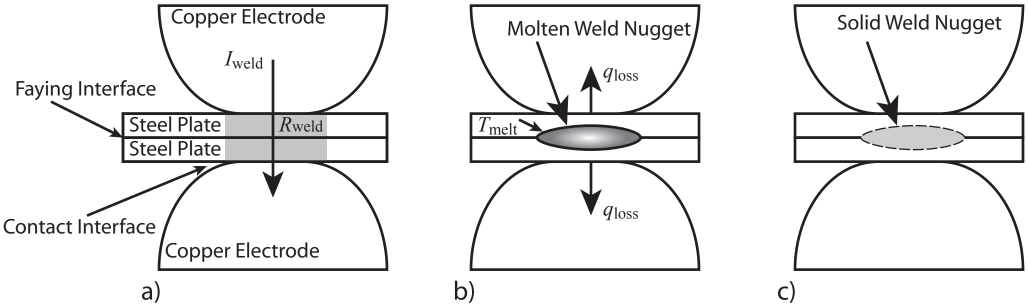

Figure 1.1: a) Initial welding stack when welding current I_{weld} is applied to the workpiece with resistance R_{weld} shown in light gray. b) The workpiece with a molten nugget when welding current is removed at t_{weld} s. Heat flux q_{loss} cools the workpiece. c) The workpiece after solidification of the molten nugget. The outline of the previously molten zone is shown in light gray.

During welding, Joule heating occurs in the workpiece according to Equation (1.1) due to the higher resistivity of the material and the high current density that is generated by a limited contact area between the electrodes and workpiece.

$$Q_{\text{weld}} = I_{\text{weld}}^2 R_{\text{weld}} t_{\text{weld}} \tag{1.1}$$

Q_{weld} in J is the heat energy in the weld region, I_{weld} in A is the welding current, R_{weld} in Ω is the total resistance of the workpiece in the weld zone and t_{weld} in s is welding time in which current is applied. Equation (1.1) is a highly simplified expression for a very complex electro-thermal process that is elaborated on in Section

1.3.2, however, this simple equation suffices to describe the basic process.

Heat is removed through the welding electrodes by a cooling water stream flowing through them, thus localizing the accumulation of heat to the workpiece. When enough localized heat is generated, the workpiece begins to melt. The surfaces in contact with the electrodes remain cooled by thermal conduction through the electrode/workpiece interface with an outward heat flux q_{loss} in $\text{W}\cdot\text{m}^{-2}$, thus, creating a strong temperature gradient in the workpiece. With sustained heat generation, the melting of the material forms a liquid pool of metal contained within the workpiece called the weld *nugget*. When electrical current is removed, the molten nugget begins to solidify as heat is continuously removed through the electrodes by q_{loss}. The region between the plates encompassed by the liquid weld nugget completely solidifies to form a continuous region that joins the various sheets of the workpiece.

1.3.1 Welding Setup

The typical welding setup consists of a: controller, weld gun, and electrodes. The welding controller is responsible for supplying the appropriate welding schedule to the weld gun. A welding schedule is a series of operations performed by the weld gun, but most importantly describes how the welding current is applied to the workpiece.

Current is applied in *cycles* referring to the equivalent period of AC current. The time scale of a cycle is regional, 60 Hz in the Americas and 50 Hz in Europe and other parts of the world, which corresponds to 15 ms and 20 ms per cycle respectively. Thus, welding 10 cycles at 8.5 kA DC on an American weld control means 8.5 kA of DC current is applied to the weld for 150 ms. For impulse welding, AC or DC current is pulsed on a 50% duty cycle, such that current is on for half a cycle and off for half a cycle. More advanced timings for impulse welding exist but are not used enough to further elaborate upon.

The weld gun is made up of a power supply and welding transformer, water cooling, pneumatic or DC servo controlled clamping jaws, shanks that position and align the point for welding, and the electrodes that conduct electrical current through the workpiece. The welding transformer with an energy storage component (typically a capacitor) provides the necessary current through the electrodes according to the welding schedule. The voltage between the electrodes during welding is normally very small, varying between (1 to 1.5) V. However, the open circuit voltage of the welding transformer is usually higher, between (5 to 22) V, providing (30 to 150) kVA of power [4].

The clamping jaws squeeze the workpiece with two primary functions:

1. Ensure good electrical contact at the welding point.
2. Oppose an outward force that results from volumetric thermal expansion of the liquid weld nugget during welding.

Pneumatic valves are traditionally used as an affordable method of generating the required squeeze force, however, DC servo motors are being increasingly used as they provide greater control over pressure during welding.

The weld gun shanks simply position the electrodes at an appropriate distance and angle away from the jaws for welding. The shanks also provide cooling water to the electrodes and act as large conductors to carry the welding current.

Finally, the electrodes are a critical component to producing the spot weld. Electrode size and shape varies depending on the desired application. In general, a large electrode is used for large workpieces so that they can remove a greater quantity of heat from the workpiece. The most important feature of the electrode is the tip surface, which determines the contact area A_e with the workpiece. This is responsible for increasing the current density at the desired weld location, which in turn generates the required heat for welding. In addition, the contact area is also responsible for cooling the surface of the workpiece and can affect the aesthetics of the final weld by the size and depth of the footprint it leaves after welding.

Since there are a large number of welding setups for a wide range of applications, this thesis focuses on setups common to welding mild and high-strength steel (HSS) sheets between 0.6 mm and 2 mm in thickness, for stacks of 2 plates (2T) with plate coatings that include Galvanized Iron (GI), Galvaneeled (GA) and Hot Dipped Galvanized (HDG). Stacks of three plates (3T) are reserved for future research as the ability of ultrasound to penetrate the stack is substantially weaker. Welding was done on both DC and AC impulse weld guns for applications in the automotive industry including roof panel assembly, and front end body-in-white frame assembly.

1.3.2 The Welding Electrothermal Process

The primary mechanism responsible for melting the workpiece and forming the weld nugget is joule heating according to Equation (1.1) in Section 1.3. This is heat energy resulting from resistively dissipated power over time. The easiest way to control the total heat generated is by changing the welding current and welding time. This is the function of the weld gun controller and current transformer.

Heat generation in the weld is a little more complex. First, the total resistance is a combination of bulk resistance of the material, and contact resistance between electrodes and plates. At the start of welding, contact resistance is very high as the imperfect surfaces have limited contact area due to roughness, dirt, oil, oxide and damage from wear. After just a few welding cycles, heat generated at these highly resistive interfaces softens the material and burns away contamination. The softer cleaner interfaces under high pressure from the squeeze force of the weld gun quickly reduce the resistance, resulting in continuous interfaces [5]. Thereafter, the total resistance responsible for melting is predominately that of the bulk material.

Expressing the resistance of the workpiece R_{weld} of Equation (1.1) as:

$$R_{\mathrm{weld}} = \frac{d_{\mathrm{wp}}}{A_{\mathrm{e}}\sigma_{\mathrm{wp}}} \tag{1.2}$$

where d_{wp} is the workpiece thickness in m, A_{e} is the electrode contact area in m^2 and σ_{wp} is the workpiece material conductivity in $\Omega{\cdot}\mathrm{m}^{-1}$, it is clear that for a fixed conductivity and workpiece thickness, the resistance can be varied by changing contact area. This is one function of the electrodes, particularly in cases for welding dissimilar metals.

There is also a secondary mechanism affecting the melting of the workpiece. This is heat removal through the electrode face. The purpose of heat removal is to:

1. Ensure generated heat remains centralized in the workpiece.
2. Prevent melting of the electrodes
3. Direct grain growth during solidification.
4. Promote proper formation of inter-metallic phases.

Heat loss through the electrodes can be expressed as:

$$q_{\mathrm{loss}} = \Delta T h_c A_{\mathrm{e}} \tag{1.3}$$

where, ΔT in K is the temperature difference between the workpiece and electrode and A_{e} in m^2 is the electrode contact area from a tip face diameter d_{e}. The thermal contact conductance co-efficient h_c in $\mathrm{W}{\cdot}\mathrm{m}^{-2}{\cdot}\mathrm{K}^{-1}$ determines how well heat can pass through the contact interface and is a function of a number of surface characteristics as will be discussed in Chapter 3. To complicate matters, material properties including conductivity, density and specific heat capacity change with temperature, and thus theoretically determining a perfect welding setup and schedule becomes a very difficult task.

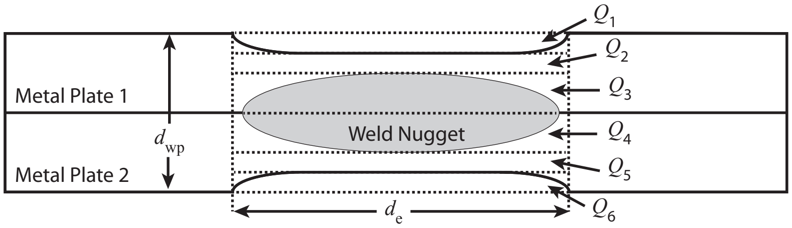

Figure 1.2: Q_1 and Q_6 are the heat energy in the indented regions, Q_2 and Q_5 are the heat energy in the solid regions and Q_3 and Q_4 are the heat energy in the nugget.

There are a number of models used for determining the required welding current, tip face diameters and squeeze forces for producing good welds. A simplified model widely used in the Japanese automotive industry is the Law of Thermal Similarity (LOTS) [6]. LOTS is based on heat flow analysis in which the temperature distributions from known specimens are used to predict the required welding parameters for different plate thicknesses [5]. The simplified law states that to obtain the same temperature distribution in thicker plates, the welding time must be increased in proportion to the square of the plate thickness [7], as in:

$$t_{\text{weld}} \propto d_{\text{wp}}^2 \tag{1.4}$$

Similarly, other setup parameters can be derived. In general, an increase in plate thickness and tip area by an arbitrary factor of N requires an N^2 increase in weld time, and the current density decreased to N times the original, in order to have a temperature distribution equivalent to the reference specimen [6, 8].

Although LOTS has proven successful in many applications with similar plate thickness' in a workpiece, applying LOTS to workpieces with plates of varying thickness and material properties is not always successful. Thus, a modified heat balance model can be used in which the various zones of the weld are separated and the required heat for each zone is derived. Figure 1.2 shows the division of the weld area.

The total heat required to attain an appropriate temperature distribution is then the sum of the heat desired in each region, where the desired heat in each region can be calculated by:

$$Q_i = m_i c_{\mathrm{p}i} \Delta T_i \tag{1.5}$$

where Q_i in J is the total heat energy of region i, m_i in kg is the mass of region i (assumed to be a flat cylinder with cap area A_{e} and height equal to that of the desired region), $c_{\mathrm{p}i}$ in $\mathrm{J{\cdot}kg^{-1}{\cdot}K^{-1}}$ is the specific heat capacity of the region i and ΔT_i in K is the change in temperature in region i as a result of heating.

This model does not account for heat loss through the plates and electrodes, and thus does not represent the total heat generated during welding, but the remaining heat required to create the desired temperature distribution and weld size. This model was verified extensively in [9] and shows that welding schedules can be theoretically determined with some degree of accuracy.

More complex weld schedules may contain a number of different stages in welding, for instance, some aluminum welding schedules pre-heat the workpiece with a few cycles for low current before applying high current to complete the weld. Some high strength steels require short pauses after a number of heating cycles to regulate heating and cooling rates to ensure the proper formation of grains and inter-metallic phases within the weld. Welding schedules vary vastly from application to application and must consider the material properties, plate thicknesses and coatings, in order to produce a weld with a desired size and strength.

1.4 Weld Properties and Quality Factors

The quality of a weld is ultimately determined by its yield strength. This is measured by stressing the weld in the direction in which it was designed to resist. The welded plates of the workpiece are pulled either axially (pull stress) or laterally (shear stress) and the force required to break the weld is measured, however, this destructive form of evaluation is not suitable for in-process testing of large volumes. Thus, the weld features contributing to yield strength have been identified and are measured destructively and non-destructively to ascertain the quality of the weld indirectly [10].

The main factors affecting the strength of the weld are:

1. Nugget geometry.
2. Indentation.
3. Defects (e.g. voids, cracks and inclusions.)
4. Material phases in the heat affected zone (HAZ).

Fig. 1.3 shows a schematic representation of a spot weld between two plates as well as the geometric factors that affect quality. A cross section of an actual weld is shown in Fig. 1.4, where the dimensions and features depicted in Fig. 1.3 are visible.

For this work, quality inspection focuses on nugget geometry, indentation and defects only. The material phases that form during welding, although important, are beyond the scope of this work and thus not covered. Although, it will be shown in the conclusion that information gathered relevant to this dissertation could be used to additionally monitor material phases in future work.

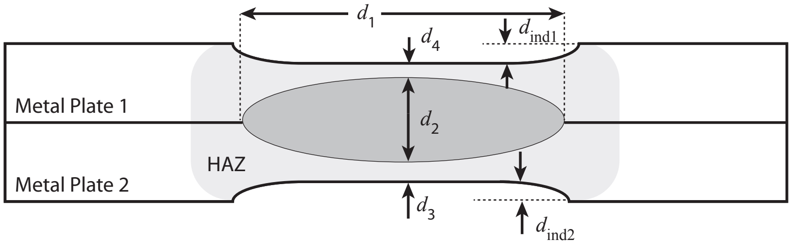

Figure 1.3: Schematic of a spot weld cross-section with nugget diameter d_1, nugget thickness d_2, nugget penetration depth d_3 and d_4 and indentation depths d_{ind1} and d_{ind2}. The heat affected zone is shown in light gray.

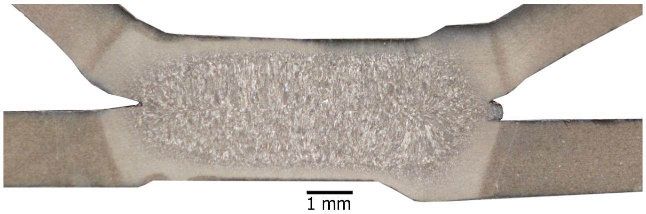

Figure 1.4: Actual cross-section of a spot weld. The metal plates have been peeled apart to highlight the true nugget diameter d_1 as it is shown in Fig. 1.3. The nugget appears as a peppered gray where the columnar grain structure is visible. The heat affected zone is also visible as a lighter shade of gray surrounding the weld nugget.[1]

1.4.1 Weld Geometry

One of the most significant factors that affects weld strength is the diameter of the weld nugget, d_1 in Fig. 1.3. In many repeated studies, larger nugget diameters have been correlated to higher yield strengths and longer fatigue life [11]. The height of the nugget d_2, or equivalently the penetration depth of the liquid nugget towards the outer surfaces d_3 and d_4 of the workpiece is also used by European automakers who rely on tensile test as an additional quality parameter, but a sufficient nugget diameter d_1 is still required in these cases. Nonetheless, for large data sets, obtaining d_1 by physical measurement if far easier where currently the only way to determine d_2 is by a labour and cost intesive process of cross sectioning, polishing and etching each weld to obtain images similar to Fig. 1.4.

The nugget geometry is best determined by metallurgical cross-sectioning shown in Fig. 1.4, where the weld is cut, polished and etched though the center cross-section. This allows physical measurement of the solidified nugget and shows the presence of inter-metallic phases and grain directions. For quality evaluation, this method is extremely slow and labor intensive, so an alternative destructive method is the peel

---

[1] Photo modified from its original source: http://upload.wikimedia.org/wikipedia/en/e/e6/Spot-weld-cross-section.DP590.meb.jpg. The original work is licensed under the Creative Commons Attribution-ShareAlike 3.0 License. This licensing tag was added to this file as part of the GFDL licensing update.

test.

The peel test involves bending back one plate from the workpiece until the plate peels around the weld, leaving a button on the workpiece where the nugget was formed. Measuring the diameter of the nugget by peel test is a common method of determining the nugget size, although only a limited amount of information is obtained. A detailed study of the effects of abnormal welding conditions by Li et. al. [12] showed a very close correlation between peel test diameters and the results obtained from Tensile-shear and Impact testing. A summary of the results show that on average, a peel test measurement results in a 0.14 mm smaller diameter than that determined by a tensile-shear test, 0.07 mm larger than the results of an impact test and overall a peel test generates a measurement with the lowest variation over the other tests. Additional measures taken in this work to ensure accurate physical measurement included B-scan imaging of the weld in a scanning acoustic microscope to image and measure the fused region between the plates.

1.4.2 Indentation

Indentation results when pressure exerted on the workpiece by the electrodes during welding, deforms the plates leaving a dimple or creator at the welding site. Indentation can be seen on the surface of the welded plates in Fig. 1.4 and is schematically shown in Fig. 1.3. Depending on the materials, welding schedule and electrodes, indentation can vary greatly and different setups have different specifications regarding indentation. An acceptable amount of indentation can typically lay between 10% - 30% of the total workpiece thickness and is calculated by:

$$\%ind = \frac{d_{\mathrm{ind1}} + d_{\mathrm{ind2}}}{d_{\mathrm{wp}}} \tag{1.6}$$

A number of studies have shown a relationship between indentation and the yield strength of a weld where welds with significant and/or excessive indentation have a much lower yield strength than welds with minimal indentation. Xiaoyun et al. in [13] showed a number of such measurements summarized in Fig 1.5.

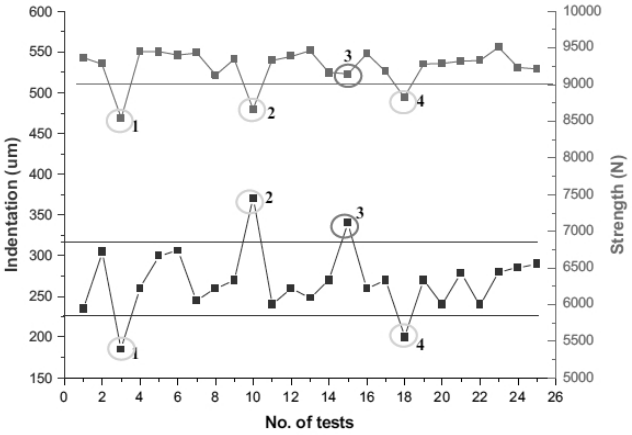

Figure 1.5: [13] Experiment from [13] showing indentation with the corresponding yield strength of the weld. Both excessive and insufficient indentation can result in poor yield strength due to over/under welding.

Indentation can be measured post process using calipers, or during welding by monitoring electrode displacement via DC stepper motor feedback. Physically mounted devices on pneumatic weld guns have also been used to measure indentation during welding [14], however, the extra physical hardware is often undesired in industrial setups due to issues with failure and reliability.

1.4.3 Cracks and Voids

A final contributing factor to weld quality (relevant to this work) is the presence of nugget defects such as surface or internal cracks due to thermal stress and shrinkage during cooling, and the presence of air bubbles or voids in the nugget as a result of material contraction. Fig. 1.6 shows examples of both voids and cracks found in spot welds.

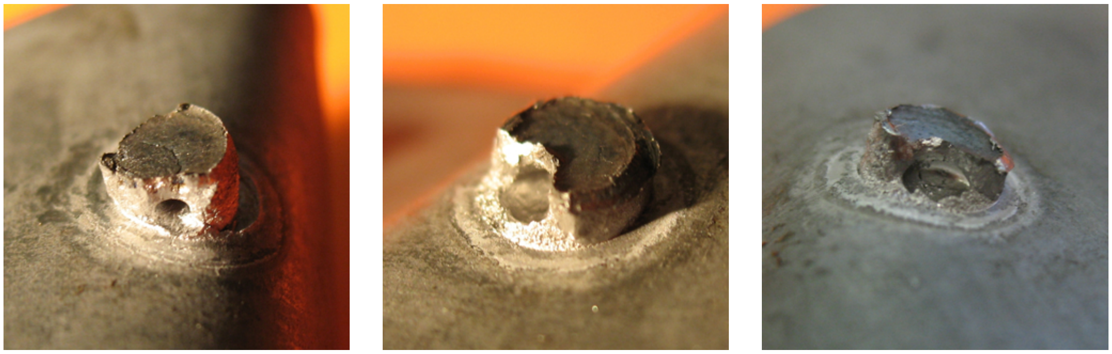

(a) (b) (c)

Figure 1.6: Defects found in peel tests. a) Small void with surface crack. b) Large void. c) Large void with interior cracking.

Under stress, cracks tend to grow and act as failure points in the weld, reducing the overall yield strength of the joint. Voids or inclusions alone may or may not have a substantial effect on the overall yield strength, however, the presence of shrinkage voids are generally accompanied by cracks. The large voids shown in Fig. 1.6 resulted in two plate workpieces (2T) consisting of 2 mm HSS GA plates, which exhibited a substantial surface expulsion. It has been documented that the primary mechanism of formation of these voids is the hold time after welding [15]. It is also believed from observations in this work that when a substantial portion of the molten weld nugget is lost during expulsion, the squeezing force during the cooling of the weld can no longer apply sufficient force to the molten nugget as it cools. This is because the resulting smaller molten region no longer occupies a substantial region below the electrode tip face and pressure from the electrodes is thus exerted on the non-molten region surrounding the nugget. Without squeeze force applied directly to the molten nugget, shrinkage during cooling opens cavities within the nugget which otherwise would have been held closed by a compressive force that displaces the surface of the weld instead.

1.5 Welding Expulsions

Occasionally during welding, a large spark may emit from the weld region. This occurs when the liquid nugget has managed to breach the weld region between the electrodes and is violently ejected from the weld. This event is called an expulsion.

Expulsions are often a sign of improper welding parameters or problems with the physical welding setup such as damaged electrodes, poor contact conditions, or miss-aligned contact with the workpiece. Some industries weld to the point of expulsion to ensure they have indeed melted the metal, but this practice has many disadvantages including a potential compromise of the joints strength. In general, good welds can and should be formed in the absence of expulsion, preserving the life of the electrodes and ensuring excessive material is not lost from the weld zone.

It has been shown in a number of different papers [5, 16, 17] that expulsions significantly reduce the peak load and energy absorption of spot welds, thus, despite individual welding philosophies, expulsions should be reduced, if not eliminated completely from the welding process.

The focus of this dissertation is on expulsion events and how they can be identified, classified and predicted by real-time monitoring of the welding process. In order to monitor the welding process for expulsions, the nature of expulsion events must first be understood. The following sections examine the causes and types of expulsion that can occur and reviews current methods for expulsion detection and prevention.

1.5.1 Types of Expulsion

Expulsions can be categorized into two types:

1. Surface expulsions.
2. Faying interface expulsions.

Surface expulsions result when the liquid nugget manages to melt through the surface of the workpiece, usually near the edge of the electrode. Once the surface melts, the pressure of the growing liquid nugget is released. This often results in a significant loss of material, which is often found as a splash emitting from the site of expulsion as shown in Fig. 1.7 a). The main problem with surface expulsions is the resulting indentation is typically significant. This has two effects on the quality of the weld. Firstly, excessive indentation is prone to surface cracking and correlates to reduced yield strength as was discussed in Section 1.4.2. Secondly, the significant loss of material creates a depressed region under the center of the electrode in which the squeeze force cannot exert sufficient pressure on the molten nugget to prevent shrinkage voids from forming. Such voids were discussed and shown in Section 1.4.3.

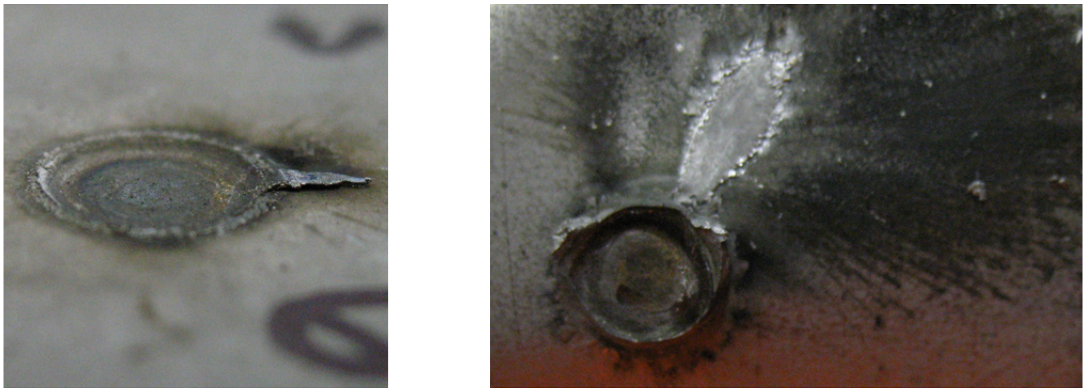

(a) (b)

Figure 1.7: Expulsions occurring a) on the plate surface and b) at the faying interface between plates.

Faying interface expulsions result when the liquid nugget grows significantly in the lateral direction and melts to a point where the interface between two plates is no longer under enough pressure to contain the nugget. At this point, the pressure from the liquid nugget squeezes in between two plates. Faying interface expulsions are less violent and do not result in as much material loss as surface expulsion since the metal between the plate interface quickly solidifies, preventing further removal of material. This is shown in measurements presented in Chapter 5. Faying interface expulsions can also be seen as a similar splash (shown in Fig. 1.7 b) but only after separating the plates of the workpiece.

1.5.2 Root Causes of Expulsion and Prevention

Expulsion occurs when then molten nugget breaches an interface in the welding setup. This happens when pressure from the growing nugget exceeds the pressure exerted on an interface due to either overheating or insufficient cooling. Circumstances that allow this to arise include: electrode misalignment or damaged electrodes that increase current density, or poor thermal contact that reduces heat transfer through the electrode workpiece boundary (reduced h_c.). Simply increasing the weld gun squeeze force can have the undesired effect of creating excessive indentation on good welds and so increasing weld pressure is not necessarily a suitable solution. Alternatively, controlling the pressure of the weld nugget by controlling the heating rate of the weld is a much better way of preventing an expulsion and even ensuring consistently good welds are made.

The best method of preventing expulsion is to have a proper welding setup (schedule and electrode sizes) and maintain constant welding conditions. Unfortunately, each weld has some affect on the condition of the electrodes and the surface conditions from plate to plate vary. Because of this, constant welding conditions are impossible to ensure and the inevitability of such a random and degrading process is undersized welds and expulsions that must be detected.

As presented in Section 1.3.2, the size of the weld nugget is a function of heat generation, which results from joule heating. Thus, controlling the welding current is a suitable method of preventing expulsion. In fact, dynamic weld controllers are currently in use that vary the welding current by measuring the changing resistance of the weld region and are quite effective. The main drawback is that correlation between resistance and the necessary welding current does not consider heat transfer through the electrode, which is the next cause of expulsion to discuss.

Heat generated from the welding current is partly dissipated through the bulk material and mostly dissipated through the contact interface with the copper electrodes. When these electrodes become contaminated with welding residue, oxides, dirt and oil from repeated welds, the thermal transfer through this interface changes drastically. When insufficient heat is removed from the weld zone, the effect is similar to that of excessive current and an expulsion can result. In addition, variable thicknesses in the zinc layers on galvannealed and hot dipped galvanized plates has shown to have a surprising large effect on this thermal transfer between the plates and electrodes; "A discontinuity in temperature exists across the electrode interface. The heat transfer characteristics across this interface significantly affects the nugget development mechanism in zinc coated low carbon steel" [18]. In fact, a one micrometer change in the zinc layer thickness can have up to a 10% change in the thermal transfer coefficient between the workpiece and electrodes [18]. Thus, prevention of expulsions in modern dynamic weld controllers is currently limited and detection of expulsions is widely desired for quality evaluation.

This work will show that the application of ultrasound can both detect and prevent expulsion since measurement of the root causes of expulsion (excessive heating from localized high current densities, poor thermal transfer or insufficient squeeze force) is possible.

1.5.3 Existing Methods of Expulsion Detection

To date, there are number of existing methods for detecting expulsion in resistance spot welding. These methods focus on monitoring three main features during welding, including:

1. Electrode Force/Displacement
2. Acoustic Emission
3. Changes in workpiece resistance

Methods that focus on Electrode Force/Displacement include [19, 20] and rely heavily on signal filtering and processing to distinguish expulsion from regular welding phenomenon. Electrode displacement alone requires additional hardware that may interfere with the workpiece during welding is not desired in production environments.

Acoustic sensors utilized in [21] were shown to be ineffective in production environments due to background noise and again, require additional external hardware.

Electrical signal, such as voltage and resistance used in [22] show promise for median frequency DC welding machines, however, is not applicable to AC welding machines and in both cases in not effective when expulsion occurs near the end of welding since the dynamic resistance can only be calculated reliably at one point per AC cycle [20].

Finally, recent trends have been to combine these signals with additional filtering and fuzzy logic [23, 24] to produce highly reliable detection where single detection methods fail, but these methods still rely heavily on unreliable sources of data, additional mechanisms for collecting this data and most importantly are not suitable for every welding setup (e.g. a pneumatic weldgun without force or displacement data.)

Thus, there is still a significant interest in developing a robust, reliable, non-evasive to production and versatile method for detecting expulsions in resistance spot welding. This work takes a brand new approach by utilizing an Inline ultrasound device embedded in the welding electrode. To date, there has been no ultrasonic investigation on the detection of expulsion. Chapter 2 describes the ultrasound setup used in this work and outlines the advantages of an ultrasonic approach to the problem.

1.6 Finite Element Modeling

To fully understand the mechanisms at work during welding and expulsion, a detailed Finite Element Method (FEM) electro-thermal model of the resistance spot welding process was constructed. This model was completed in two parts:

1. An electrical model to determine the current density distribution within the electrode and workpiece.
2. An electro-thermal model within the weld stack to determine heating and nugget growth.

This simulation was created specifically for this research using Comsol Multiphysics with partial contributions towards object meshing which was completed in collaboration with J. Kocimski and P. Kustron in [25].

First, a DC conductive media model was created to determine how current flows through the stack up. The welding setup for 3/4" B-nose electrodes on 2T 0.7 mm mild steel plates was modeled as this was a common setup in lab testing. The geometry of the model was easily adjustable, and simulation results were obtained for varying stack-ups. The results for the 2T 0.7 mm stack-up is presented in Fig. 1.8 a, b), which shows half of a cross section of the welding setup. To simplify computational time, the welding setup was modeled with axial symmetry.

In this model, a current source was created at the outer ring of the upper electrode and grounded at the outer ring of the lower electrode; these correspond to the contact points of the electrode with the shank. The current density within the setup, and

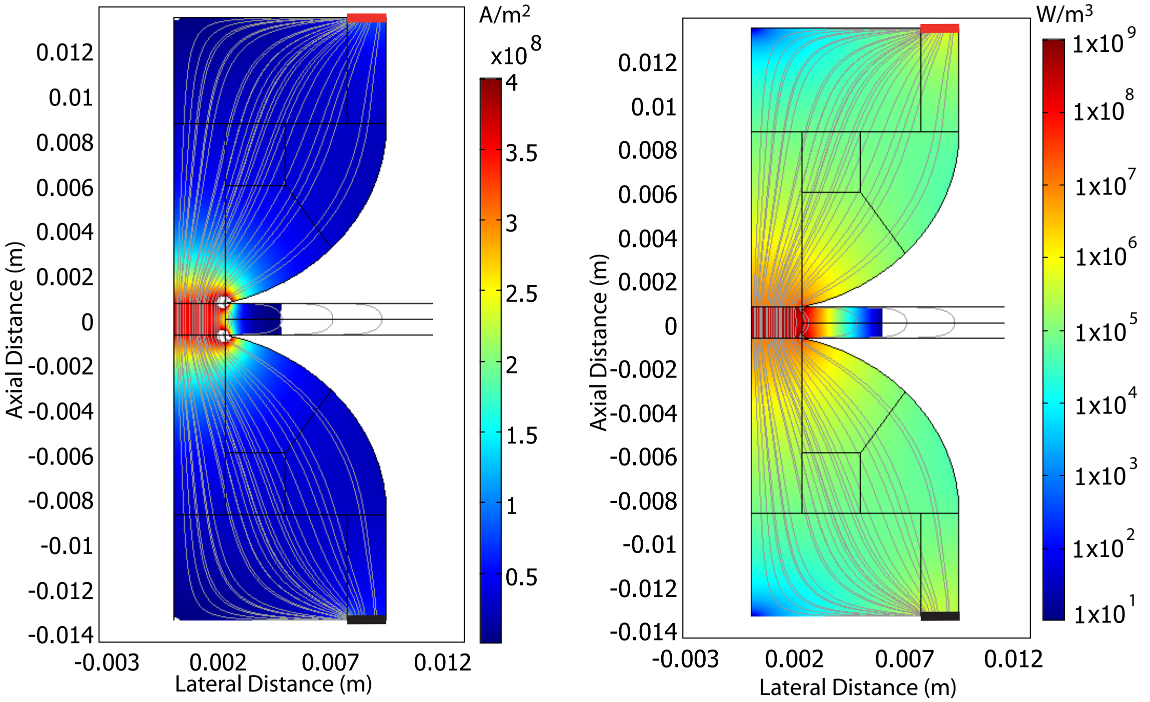

(a) Current density through the electrodes and stack up. $[A/m^2]$

(b) Joule heating in the bulk material of the copper and steel. $[W/m^3]$

Figure 1.8: Finite Element Analysis (FEA) simulation of the electrical current behavior for 3/4" B-nose electrodes and two 0.7 mm plates welded at 9 kA. The axial symmetric model in a) and b) shows current flow (gray streamlines) with current density and joule heating respectively.

particularly the current density profile along the tip of the electrodes was determined at room temperature. Although heat propagating into the weld during welding would alter the profile of this distribution, this mild heating does not substantially change the current density distribution along the electrode tip. From this model, the initial resistive heating of the setup could be extracted as shown in Fig. 1.8b.

The current density distribution was determined using this model for a number of welding currents. This distribution is critical to understanding heat generation in the weld and the sources of expulsion. Since the geometry of the electrode grows narrow at the point of contact with the workpiece, extremely high current density arises at the corner of the B-nose cap where it contacts the workpiece. The current density decreases towards the center of the contact area. This distribution was modeled in this work as a radially dependent source according to:

$$J(r) = Ae^{Br} + Ce^{Dr} \tag{1.7}$$

where $J(r)$ is the current density function in A·m^{-2}, r is the radial distance from the center of the electrode in m and A, B, C and D are parameters determined by a best fit to the simulated distributions. A and C scale proportional to the welding current amplitude while B and D scale with the maximum electrode radius.

Next, a transient electro-thermal interaction model of the welding process was created using the same axial symmetric geometry shown in Fig. 1.8, where a conductive media DC model was used to simulate current density in *only* the stack up using temperature dependent material properties of the stack up from [26] and MPDB v7.11 software. The source of electrical current for this model was the contact surface between the electrode and workpiece, using the current density distribution determined by the electrical model of Fig. 1.8. The compact electrical model within the workpiece was coupled to a thermal conductive heat model of the complete setup, where the electrical simulation of the workpiece acted as a heat source for the thermal model and the ends of the electrodes acted as a heat sink modeled by a constant temperature.

Fig. 1.9 shows the simulated temperature distribution at a number of different stages during welding. For each time step in the simulation, the current density and temperature dependent material conductivity within the workpiece acted as a joule heat source for the heat transfer by conduction model. This heat transfer model then updated the temperature distribution in the workpiece and electrodes which was then used to update the temperature dependent material properties for the subsequent

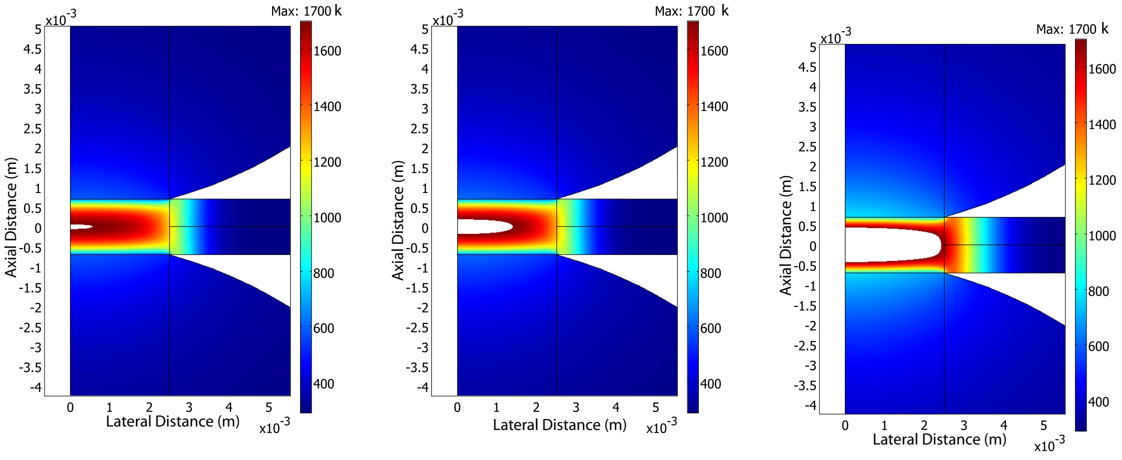

(a) At the start of melting (78 ms.)

(b) During nugget growth (120 ms.)

(c) At current off (166 ms.)

Figure 1.9: Simulated temperature distributions during resistance spot welding of two 0.7 mm steel plates at 8.5 kA. The liquid nugget is shown in white.

iteration of the electrical simulation. This was repeated for a duration corresponding to an appropriate weld time, or weld schedule.

One consideration was the simulation time step for the time dependent thermal model. A parametric simulation with different step sizes resulted in consistent and stable simulation results at 1 ms time step intervals. The maximum change in temperature in the workpiece occurs during the heating stage of the plates. The average temperature change in the workpiece for a 1 ms time step was approximately 10 K, equivalently 10000 $K{\cdot}s^{-1}$ for 9500 A welding current. This information was critical to knowing the timing requirements for sampling the system, which is discussed in further detail in Chapter 2.

To verify the model, a comparison of the simulated nugget diameter with actual welds was performed for different welding currents and plate thicknesses. Due to the number of variables and complexity of simulating a given setup, the model was verified by determining the degree of agreement between the simulated and measured results.

Fig. 1.10 shows the simulated nugget diameter vs. the measured nugget diameter for thirty permutations of welds using three workpieces with varying welding currents. The solid line (linear fit) shows the agreement between the FEM simulation results and the physical measurements and the dashed line shows a perfect fit.

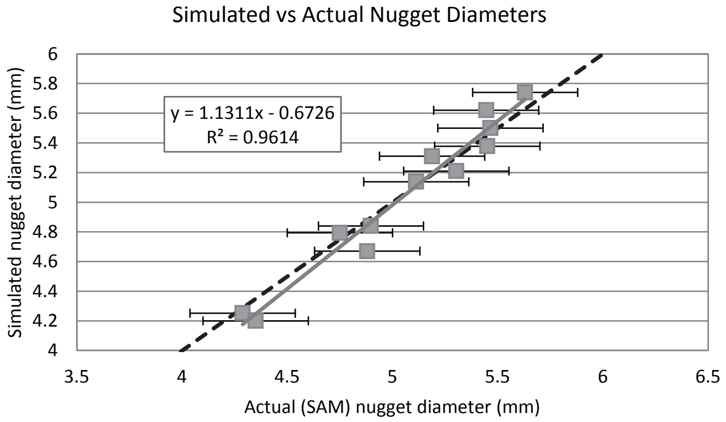

Figure 1.10: Simulated nugget diameters compared to measured diameters for welds conducted on 2T workpieces using 0.7 mm, 1.2 mm and 1.5 mm plates welded at (7-9) kA in 500 A increments.

The actual weld diameter was measured by a Scanning Acoustic Microscope (SAM) with accuracy of ±0.25 mm compared to peel testing as reported in [27]. Due to the elliptical shape of most spot welds, the actual diameter values shown in Fig. 1.10 are the average of six nugget diameter measurements over two welds performed for each workpiece-weld current combination and the error bars show the sum of the standard deviation of the diameter measurements with the measurement accuracy of the SAM.

Using the FEM model of the spot welding process, the main contributers to overheating (and expulsion) were verified. The degree of overheating as a result of increased current density, and/or decreased heat transfer through the electrode could be simulated and observed. These results are important to Chapter 3 where monitoring the heating rate of the weld is presented. From this model, temperature distributions in the workpiece at key moments in welding (melting and solidification) were estimated and these estimates are used in the methods presented in Chapter 3 and Chapter 4. Finally, the model provided the maximum expected change in temperature at any given momet for different setups, providing the timing requirements for scanning nescessary to distinguis expulsions from normal welds.

References

[1] J. Jennings and J. Gould, “A new road for automotive architectures,” *Welding Journal*, vol. 87, no. 10, pp. 2–30, 2008.

[2] M. Crooks and R. Miner, “The ultralight steel auto body program completes phase i,” *Journal of Metals*, vol. 48, no. 7, pp. 13–15, 1996.

[3] Y. Kurihara, “The role of aluminum in automotive weight reduction, part i,” *Journal of Metals*, vol. 45, no. 11, pp. 32–33, 1993.

[4] S. Deb and S. Deb, *Robotics Technology and Flexible Automation.* Tata McGraw Hill, 2010.

[5] H. Zhang and J. Senkara, *Resistance Welding Fundamentals and Applications.* CRC Press Taylor & Francis Group, 2006.

[6] T. Okuda, “Spot welding of thick plates, part 1: The law of thermal similarity, welding technique,” *Japanese Welding Society*, vol. 21, no. 9, 1973.

[7] M. Fong, A. Tsang, and A. Ananthanarayanan, “Development of the law of thermal similarity (lots) for low indentation cosmetic resistance welds,” 2000.

[8] K. Ando and T. Nakamura, “On the thermal time constant in resistance spot welding, report 1,” *Japanese Welding Society*, vol. 26, 1957.

[9] “Welding handbook,” in *Welding Processes, 9th Ed.* American Welding Society, 2001, vol. 2.

[10] M. Zhou, H. Zhang, and S. Hu, “Relationship between quality and attributes of spot welds,” *Welding Journal :Welding Research*, vol. 82, pp. 72–s–77s, 2003.

[11] Y. Rui, R. Borsos, R. Gopalakrishnan, H. Agrawal, and C. Rivard, “Fatigue life predition method for multi-spot-welded structures,” *Society of Automotive Engineers (SAE)*, no. 930571, 1981.

[12] W. Li, S. Cheng, S. Hu, and J. Shriver, "Statistical investigation of resistance spot welding quality using a two-stage, sliding-level experiment," *Trans. of ASME - Journal of Manufacturing*, vol. 123, no. 153, 2001.

[13] Z. Xiaoyun, Z. Yansong, and C. Guanlong, "Weld quality inspection based on on-line measured indentation from servo encoder in resistance spot welding." pp. 1353–1356, April 2006.

[14] C. Tsai, W. Dai, and D. Dickinsion, "Experimental study of weld nugget expansion-contraction behavior of resistance spot welding," in *Proc. Sheet Metal Weld. Conf.*, 1992.

[15] A. Joaquin, A. Elliott, and C. Jiang, "Reducing shrinkage voids in resistance spot welds," *Welding Journal*, vol. 83, pp. 24–27, 2007.

[16] M. Pouranvari, A. Abedi, P. Marashi, and M. Goodarzi, "Effect of expulsion on peak load and energy absorption of low carbon resistance spot welds," *Sci Technol Weld Join*, vol. 21, pp. 39–43, 2008.

[17] F. Nikoosohbat, S. Kheirandish, M. Goodarzi, M. Pouranvari, and S. Marashi, "Microstructure and failure behavior of dp980 dual phase steel resistance spot welds," *Mater Sci Technol*, vol. 26, pp. 738–744, 2010.

[18] E. Kim and T. Eagar, "Measurement of transient temperature response during resistance spot welding," *Welding Research Supp. Welding Journal*, pp. 303s–312s, August 1989.

[19] L. Xinmin, Z. Xiaoyun, Z. Yansong, and C. Guanlong, "Weld quality inspection based on online measured indentation from servo encoder in resistance spot welding," *IEEE Trans. Instrum. Meas.*, vol. 56, no. 4, pp. 1501–1505, 2007.

[20] W. Li, J. Ni, and S. Hu, "On-line expulsion detection and estimation for resistance spot welding," in *NAMRC XXVII*, 1999, pp. 165–1 – 165–5.

[21] S. Vahaviolos, M. Carlos, and S. Slykhouse, "Adaptaive spot weld feedback control loop via acoustic emission," *Material Evaluation*, vol. 39, no. 10, pp. 1057–1060, 1981.

[22] M. Hao, K. Osman, D. Boomer, and C. Newton, "Developments in characterization of spot welds," *Welding J.*, pp. 1s–7s, Janurary 1996.

[23] P. Podrzaj, "Fuzzy logic based expulsion detection in resistance spot welding," in *Proc. ASMCSS'09*, 2009, pp. 222–225.

[24] P. Podrzaj, I. Polajnar, J. Diaci, and Z. Kariz, "Expulsion detection system for resistance spot welding based on a neural network," *Welding J.*, Janurary.

[25] A. Karloff, A. Chertov, J. Kocimski, P. Kustron, and R. Maev, "New developments for in situ ultrasonic measurement of transient temperature distributions at the tip of a copper resistance spot weld electrode," in *Proc. IEEE Int. Ultrasonics Symp.*, 2010, pp. 1424–1427.

[26] V. Kurz and B.Lux, "Lokalisierung der erstarrungsfront beim stranggießen von stahl," *Berg- und Hüttenmännische Monatshefte*, vol. 5, 1969.

[27] A. M. Chertov, R. G. Maev, and F. M. Severin, "Acoustic microscopy of internal structure of resistance spot welds," *IEEE Tran. on Ultrasonics, Ferroelectrics, and Frequency Control*, vol. 54, no. 8, pp. 1521–1539, 2007.

Chapter 2

Inline Ultrasound System

2.1 NDE in Resistance Spot Welding

There are currently a wide range of Non-Destructive Evaluation (NDE) methods used for assessing the quality of a spot weld, usually performed post process. Some of these include: ultrasonic, x-ray and optical inspection. There are, however, very few methods that can accurately monitor the quality of the welding process in real-time (in-process) by actually probing the workpiece. Since heat generation in the weld stack is responsible for the formation of the weld, monitoring heat generation is considered the best means of assessing the welding process [1]. Aside from placing thermal couples in the weld region, which destroys the thermal couple and can compromise weld strength, there are currently no practical solutions to *directly* monitor the internal heat generation for repeated cycles. Since the internal temperature of the workpiece is not physically accessible for measurement (e.g. via thermocouples), indirect approaches to real-time quality assessment have been implemented for adaptive control which include: voltage/current measurement [2], plate distortion (indentation) measurement [3], and correlated ultrasonic time of flight for pulse echo and through transmission modes [4, 5, 6].

Deficiencies with indirect methods of monitoring weld quality (used in the methods listed above) result from the large variability in welding conditions, even with a constant setup. For instance, monitoring voltage and current effectively measures the total joule energy responsible for heat generation, but fails to account for current density distributions in the weld zone resulting from variable contact area of the electrodes. Resistive contributions from poor contact must also be accounted for and this changes from weld to weld. The electrode contact condition also governs heat conduction to the electrodes and is a major factor in the formation of the weld that is unaccounted for. Unlike previous in-line devices and methods, the ultrasonic device utilized in this work directly measures: weld heating, indentation and liquid nugget penetration. Using this information, the weld nugget diameter can additionally be estimated through correlations as described in this chapter.

2.2 Inline System Equipment and Setup

The Inline Ultrasound system, henceforth called the Inline system or simply Inline, was developed explicitly for real-time monitoring of the resistance spot welding process [7]. The existing Inline system utilizes a single element ultrasound transducer placed in the cooling water stream within the welding shank, and probes the weld through the copper electrode. The cooling water both protects the transducer from high temperatures conducted through the welding electrode and provides a means of coupling acoustic pressure from the transducer to the solid electrode.

Fig. 2.1 shows a schematic of the Inline setup. The transducer is driven by a

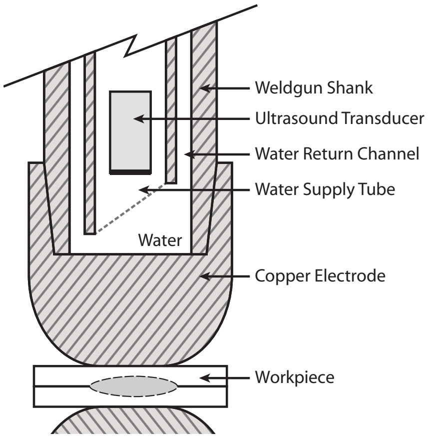

Figure 2.1: Inline transducer placement.

custom electronic controller with a pulser and receiver. The pulser is capable of producing 10 MHz pulses at (100-150) V amplitude in (2-10) ms intervals. This pulse interval is called the pulse repetition rate (PRR) or denoted as t_p. The pulse interval can also be expressed as a pulse repetition frequency (PRF) denoted as $f_p = 1/t_p$. The receiver samples incoming acoustic pressure from the transducer at a sampling frequency $f_s = 66$ MHz with 12 bits per sample. The data is transfered via a serial or USB interface and stored on a computer, where post processing takes place.

2.3 Ultrasound Imaging

Ultrasound data can be recorded and displayed in a number of different ways to convey different information. The main data modes used in this work include: A-scan and single element M-scan modes. For both, the ultrasound transducer was operated in pulse-echo mode where a single element transducer performs both pulsing and receiving of acoustic echoes through the axial center of the electrode and workpiece. Pulsing and receiving are typically called transmission and reception, notated as Tx and Rx on most devices.

In transmission, the ultrasound transducer generates an acoustic pulse.To generate an acoustic pulse, the transducer (a piezoelectric element) is excited by a voltage waveform with an approximate center frequency and pulse length equal to the desired ultrasound pulse. Of course, the response of the transducer shapes the actual emitted pulse. Thus, the emitted acoustic wave in time $y(t)$ from an ultrasound transducer is a function of both the driving voltage $v_o(t)$ and the transfer characteristics of the transducer $h_{\text{em}}(t)$.

Similarly, any pressure exerted on the transducer $y(t)$, generates a corresponding voltage $v_i(t)$ by the same transducer transfer characteristic $h_{\text{em}}(t)$. The received voltage waveform is bandpass filtered with an upper stop band frequency defined by half Niquist $(f_s/2)$, which is then sampled by a low noise A/D converter and stored digitally. The voltage to pressure and pressure to voltage response of the transducer can be modeled in the time domain by:

$$x(t) = h_{\text{em}}(t) * v_o(t) \tag{2.1}$$

$$v_i(t) = h_{\text{em}}(t) * y(t) \tag{2.2}$$

Assuming that the system produces a reflected signal composed of a series of M linear, planar reflections of our input pulse, then the system $h(t)$ can be described by:

$$h(t) = \sum_{i=1}^{M} a_i \delta(t - t_i) \tag{2.3}$$

where a_i is the relative amplitude of the i^{th} reflection and t_i is the time delay of i^{th} reflection in s.

Given the input ultrasound pulse $x(t)$ and the measured reflected output of the system is $y(t)$, then $y(t)$ resulting from the unknown system $h(t)$ can be expressed as a convolution with additive noise:

$$y(t) = x(t) * h(t) + e(t) \tag{2.4}$$

where $e(t)$ is system noise.

The amplitude and delay of the reflected ultrasound signals is a function of the propagation of sound through the medium and characteristics of the reflectors of sound. Understanding these mechanistic can provide the information required to determine the nature of the physical system $h(t)$, in this case, the spot weld.

2.3.1 Ultrasound Wave Propagation

In general, the propagation of an acoustic wave in a media is modeled by the wave equation:

$$\frac{\delta^2 u}{\delta t^2} = c^2 \bigtriangledown^2 u \tag{2.5}$$

where u in m models the displacement of particles as the wave traverses with wave velocity c in m·s^{-1}. Sound pressure p in Pa is often used instead of displacement and represents the local instantaneous deviation in pressure. Pressure is related to displacement by the specific acoustic impedance of a material, defined as:

$$z = \frac{p}{v} \tag{2.6}$$

where z is the specific acoustic impedance in Rayleigh and v is the particle velocity in m·s^{-1}. The pressure of an acoustic wave is related to the displacement of particles by the wave frequency f in Hz such that:

$$u = \frac{v}{2\pi f} = \frac{p}{2\pi f Z} \tag{2.7}$$

The specific acoustic impedance normalized over surface area S in m^2 gives rise to the characteristic acoustic impedance Z such that:

$$Z = z/S = \rho_m c \tag{2.8}$$

In the Inline setup, only longitudinal waves are utilized, where displacement u is parallel to the direction of wave propagation. The general wave velocity, c in Equation (2.5), can be expressed as in Equation (2.9a). The longitudinal wave velocity can be expressed specifically for liquids, such as the cooling water and molten nugget, and isotropic solids like copper and steel, by Equations (2.9b) and (2.9c) respectively.

$$c = \sqrt{\frac{M_{\mathrm{E}}}{\rho_m}} \tag{2.9a}$$

$$c_0 = \sqrt{\frac{\gamma K_T}{\rho_{m0}}} \tag{2.9b}$$

$$c_l = \sqrt{\frac{K + \frac{4}{3}G}{\rho_m}} \tag{2.9c}$$

For Equation (2.9b) γ is the adiabatic index of the liquid, K_T is the isothermal bulk modulus and ρ_{m0} is the density at standard temperature and pressure. For Equation (2.9c) K and G are the bulk and shear modulus of the material in Pa and ρ_m is the material density in $\mathrm{kg{\cdot}m^{-3}}$. Equation (2.9c) exemplifies how the longitudinal (compressive) waves depend on both the compressive and shear properties of the material.

2.3.2 Acoustic Reflection at Continuous Boundaries

When an acoustic pulse reaches a continuous boundary, part of the acoustic pressure is transmitted through the boundary and part of the acoustic pressure is reflected

reflected back. Acoustic transmission and reflection at a boundary depends on the characteristic acoustic impedance of the materials on either side of the boundary and are represented by the coefficients of transmission and reflection. If the acoustical impedance on the incident side of the acoustic wave is Z_1 and the acoustical impedance is Z_2 on the other side of the continuous boundary, then the transmission and reflection coefficients for acoustic pressure T_{12} and R_{12} can be written as:

$$T_{12} = \frac{2Z_2}{Z_2 + Z_1} \tag{2.10}$$

$$R_{12} = \frac{Z_2 - Z_1}{Z_2 + Z_1} \tag{2.11}$$

This is only the case for perpendicular incidence of the acoustic wave on the boundary. Since a single element transducer is utilized, perpendicular incidence can be assumed for the ideal condition. Also, since the ultrasound transducer is sensitive to acoustic pressure, Equations (2.10) and (2.11) will be used when analyzing ultrasound data as opposed to alternative expression for particle displacement and velocity.

2.3.3 A-scan construction

Each pulse and subsequent reception of reflected acoustic pressure forms an A-scan. The typical recording time for an A-scan in the Inline setup is 200 samples at a sampling frequency of 66 MHz, or equivalently 3.9 μs, in which time probing the weld can be considered a quasi-stationary process since the thermal properties do not vary significantly in this time. This was verified by the thermal FEM model presented in Chapter 1 where the maximum acceptable heating rates for thin workpieces was determined to be 10000 $\text{K}\cdot\text{s}^{-1}$ resulting in a 0.4 K change in a 4 μs sampling period.

Acoustic reflections are expected from various material interface, which may be present at different stages of welding. The source of these reflections are shown in Fig. 2.2 and the corresponding A-scans are shown in Fig. 2.3, where x_i is the i^{th} reflection due to $x(t)$ interacting with $a_i\delta(t-t_i)$ in $h(t)$. For simplicity in this work, let $x_i = x_i(t-t_i) = a_i x(t-t_i)$.

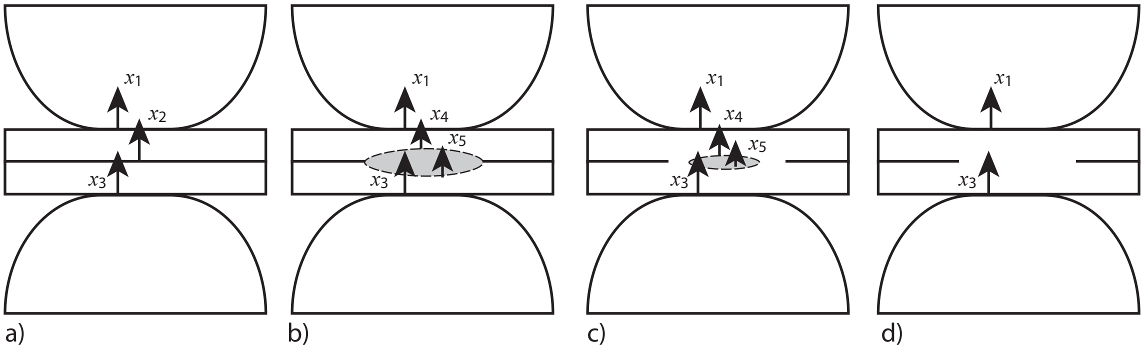

Figure 2.2: Sources of A-scan reflection in the welding setup.

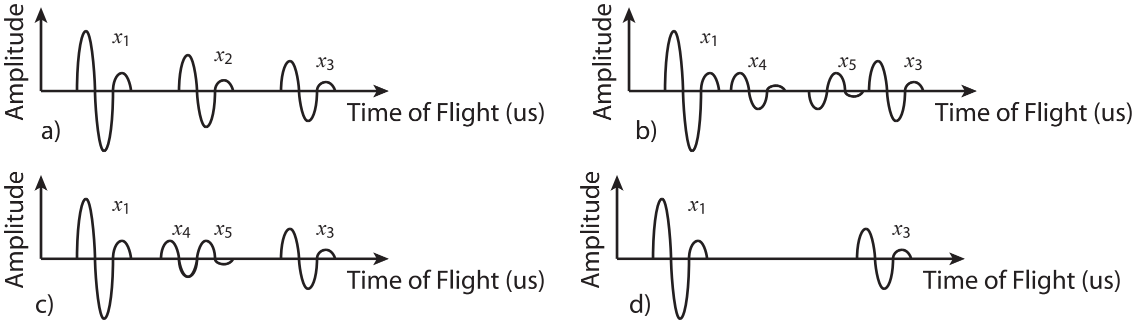

Figure 2.3: Resulting A-scans for the reflectors shown in Fig. 2.2 a) - d) respectively.

The stages of the resistance spot welding process shown in Fig. 2.2 and Fig. 2.3 can be divided into four stages as follows:

1. Weld jaws close and clamp the workpiece to be welded in place. Ultrasonically, reflections from each interface of Fig. 2.2 a) are visible as a pulse train. Initially the setup is at room temperature and the distance between reflection can

be determined by TOF measurement between reflections with a known wave velocity.

2. Welding current is applied to the workpiece to heat the plates. Shortly after melting, the boundaries of the liquid nugget becomes visible as in Fig. 2.2 b). As the nugget grows vertically and continues to heat up, the reflections shown in Fig. 2.3 b) move further apart as the geometric size of the weld increases.
3. After a fixed welding duration, current is removed and the nugget begins to solidify as the plates cool. Interfaces from the front and back of the nugget move towards one another as the vertical size of the liquid region shrinks, shown in Fig. 2.2 c) and Fig. 2.3 c). Eventually the reflections from the liquid nugget join at the moment of complete nugget solidification.
4. After the liquid nugget has completely solidified, there is finally a continuous region between the front wall and back wall reflections without additional reflections between the two plates, shown in Fig. 2.2 d) and Fig. 2.3 d).

The transducer frequency was selected as 10 MHz with 80% bandwidth to provide an axial resolution in steel such that a reflections between 0.7 mm plates could be separated by one wave length. Further increasing the frequency with the current setup resulted in greater attenuation when imaging through the copper electrode and dry rough contact between the electrode and the plates. In addition, the current sampling rate of 66 MHz is very close to the Niquist limit and further increasing the transducer frequency can result in A-scan artifacts.

The transducer used in the work is unfocused, but with a 3 mm aperture the far field sound waves are collimated with a beam width of approximately 2 mm. Nonetheless scattering at the various reflection boundaries between water and copper, and copper and steel result in reverberations and interference that can obscure the weak reflections from the weld zone. Part of this problem is discussed in Chapter 4 when filtering the undesired interference from scattering and subsequent reverberation is handled.

Finally, reverberation in the workpiece can pose an interesting problem, however, reflection intensity is typically so low that multiple reverberations are generally below the noise level and do not pose a substantial problem. Problems can arise in workpiece with drastically different plate thicknesses where the thin plate is nearest the transducer, but this only occurs up to the point of melting, where the only required information is between x_1 and x_3 and thus reverberations between the plates due to the faying interface are not considered.

2.3.4 Sound Speed and Temperature

In the welding processes, strong temperature gradients are present in the weld zone. Temperature can range from 700 K at the surface of the electrodes to 2500 K in the center of the molten nugget [1].

Since the modulus of elasticity and density of a material are dependent on temperature, it follows that the speed of sound in a material also changes with temperature. For this reason, interfaces within the weld that produce ultrasound reflections may appear to be moving, when in fact the temperature is simply changing.

The speed of sound in steel (as well as other isotropic solids) changes approximately lineally with temperature and can be expressed in terms of the a linear coefficient k_v, such that:

$$c_l(T) = c_l(T_0) + k_v \cdot (T - T_0) \tag{2.12}$$

where T is temperature in K, and T_0 is room temperature (295 K), such that $c_l(T_0)$ is the speed of sound of the material at room temperature.

For most isotropic solids, k_v is negative, indicating that the speed of sound *de-*

creases with an *increase* in temperature. For this reason, the interfaces of Fig. 2.2 a) will actually appear to move further apart as heat is generated in the weld prior to melting. Similarly, the effect of cooling reduces the TOF in the weld making it difficult to tell the true thickness of the heated sheets after welding. This issue was uniquely addressed in this research as is described in Chapter 3.

A graph of the temperature dependence of the longitudinal speed of sound for steel (as measured by [8]) is shown in Fig. 2.4, where k_v is the slope of the linear fit through the data points. Similar graphs can be extracted for the variety of metals being welded using the Inline device, since the TOF is measured to the point of melting and sheet thickness can be monitored by DC motor feedback and the nature of the temperature distribution in the weld can be estimated from FEM simulations.

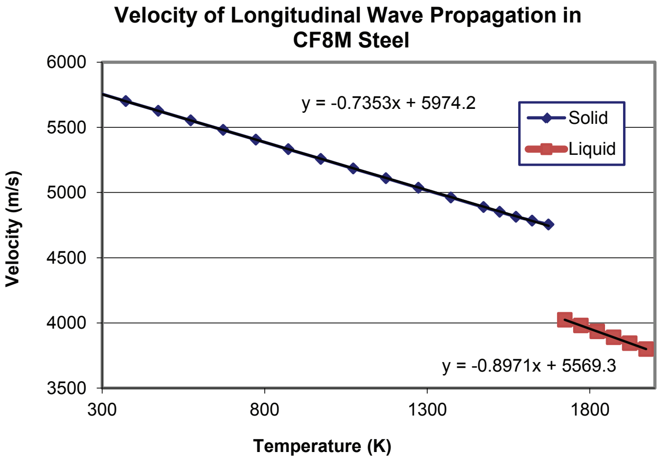

Figure 2.4: The speed of sound in mild steel.[8]

2.3.5 Single Element M-Scans During Welding

When A-scan amplitude is plotted in gray scale with sequential A-scans in time placed next to one another, an M-Scan image of the welding process if formed. Schematically, we would expect the reflections from A-scan to appear as in Fig. 2.5 a). The actual

M-scans acquired during welding follow this expected form as shown in Fig. 2.5 b).

The formation of the M-scan of Fig. 2.5 can be divided as follows:

1. Prior to time t_0 the weld gun jaws are closed to hold the workpiece in place and no weld current is applied. The reflections x_1, x_2 and x_3 appear as presented in Fig. 2.3 a).
2. At time t_0 the welding current is applied and the workpiece begins to heat up. The reflections appear to move apart due to the change in the longitudinal speed of sound, which increases TOF with temperature.
3. At time t_1 enough heat has been generated to melt the steel. Melting generally occurs at the faying interface, so ideally the faying interface reflection x_3 will split and become the upper and lower interface of the molten nugget x_4 and x_5 respectively. In reality, the geometry of the early nugget does not produce an observable reflection since it may form off axis from the ultrasound and/or is irregular in shape. When the nugget forms from the faying interface, the first stages of melting fuse the plates together eliminating reflection x_2. If the welding current were turned off at this point, before the molten nugget formed, a stick weld would result.
4. When welding current is maintained the molten nugget grows, however, the

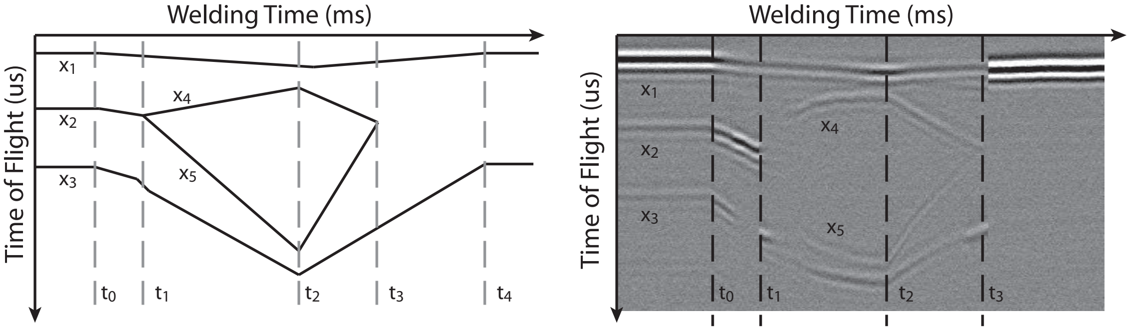

Figure 2.5: The M-scan acquired by successive A-scans during welding: a) Schematic expectation of reflections. b) Actucal M-scan acquired in real-time during welding.

nugget does not always begin to grow in the axial center of the electrodes. In this case, the nugget may not appear in the M-scan until it encompasses the region being probed by the transducer, at which time it may already have a measurable thickness. In addition, the irregular, or curved surface of the nugget can often scatter or reflect sound away from the transducer in its early stages of growth.

In Fig. 2.5 b) both mechanisms of 3) and 4) above are present and can be seen by observing reflection x_3. Immediately after melting time t_1, the reflection from x_3 increases in intensity as x_2 disappears. In this case, more sound is transmitted through the faying interface x_2 and reflected from the lower interface x_3 since the plates have begun to fuse, but no molten nugget has formed. Shortly after, there is a sudden shift in time of flight for interface x_3 accompanied by a drastic decrease in amplitude. This due to the presence of a small and irregular shaped molten nugget that both increase the time of flight (due to the abrupt decrease in speed in sound between solid and liquid steel) as well as the last of reflection from either the nugget or lower interface since sound is being scattered and reflected away from the transducer instead of transmitted through and reflected back.

5. At time t_2 the welding current is turned off. The weld then begins to cool by conducting heat through the cooled electrodes, causing the molten nugget to begin solidifying. During this colling process the upper and lower boundaries of the nugget grow closer together. Unlike the irregular or off center nugget that may be present when the nugget forms, the cooling process generally maintains and flat nugget surface. This is likely because heat is removed axially through the electrodes so that the nugget cools faster axially than laterally. This is particularly convenient for imaging. At time t_3 the liquid nugget has completely solidified and the two steel plates are now joined by a continuous region, thus

reflection x_2 is no longer present.

2.4 Quality Evaluation Using the Inline Setup

The Inline system is currently being used to estimate the size of the weld nugget. This is accomplished by establishing a correlation between the maximum time of flight through the weld with a physically measured nugget diameter [9]. This is possible because the maximum time of flight when welding current is turned off is results from the maximum temperature reached in the workpiece. Since the speed of sound decreases substantially in liquid steel, the time of flight is closely related to the thickness of the weld nugget. The diameter of the weld nugget can only be inferred from the thickness of the nugget, and so using time of flight alone is not a reliable indicator for weld quality.

2.4.1 Why Detect Expulsion using Inline?

A specific case where time of flight measurements alone do not correlate well to a nugget diameter is the case of expulsion. When an expulsion occurs, estimating the nugget diameter using the maximum TOF alone may give a false indicator of weld quality in one of two ways:

1. The expulsion removes some heat from the center of the weld zone (decreasing time of flight) making the weld appear undersized when it fact it is not.
2. The expulsion removes some material from the peripheral of the weld while maintaining heat in the probed region making the weld appear to be good, when it is not.

For these reasons, the detection and classification of expulsion is essential to improving the reliability of the current method for quality evaluation. In the process of investigating expulsion using the Inline setup, a number of other methods have been discovered that can help improve the estimation of the weld diameter, even in the presence of expulsion. In the next chapters, the new methods for detecting and classifying expulsions will be describe. In addition, it will be shown how these methods can also help estimate the nugget diameter to improve upon the current Inline system.

2.5 Summary

In this chapter, the Inline ultrasound system and setup was introduced with a brief review of existing in-process and post-process methods of performing NDE on spot welds. The general specifications of the Inline system were defined and the basics of ultrasound wave propagation were covered. The principals of acoustic transmission and reflection, as well as the temperature dependence of the speed of sound (linearly approximated using k_v) were applied to A-scan and M-scan data acquired using the Inline setup to describe the dynamics of ultrasound reflections during welding. The ultrasound A-scans were described during key moments in welding, including: heating the workpiece, melting the bulk material, cooling the bulk material and solidification of the weld nugget. This is important in the following Chapters where the properties of reflected ultrasound pulses and the temperature dependence of sound speed are exploited to predict and detect expulsion events. The sampling and pulsing rates of the Inline system defined in this chapter provided the constraints for real-time processing covered in Chapters 3 and 4. Finally, the current use of the Inline system for quality estimation was described and the importance of expulsion detection to improving the Inline system's quality estimation was added to the growing reasons why expulsion is such a critical event to detect.

References

[1] H. Zhang and J. Senkara, *Resistance Welding Fundamentals and Applications.* New York and London: CRC Press Taylor and Francis Group, 2006.

[2] P. Podrzaj and S. Simoncic, “Resistance spot welding control based on fuzzy logic,” *Int. J. Adv. Manuf. Technol.*, vol. 52, pp. 959–967, 2011.

[3] L. Xinmin, Z. Xiaoyun, Z. Yansong, and C. Guanlong, “Weld quality inspection based on online measured indentation from servo encoder in resistance spot welding,” *IEEE Trans. Instrum. Meas.*, vol. 56, no. 4, pp. 1501–1505, 2007.

[4] R. G. Maev and A. Ptchelintsev, “Monitoring of pulsed ultrasonic waves’ interaction with metal continuously heated to the melting point,” *Review of Prog. in Quantitative Nondestructive Evaluation*, vol. 20, pp. 1517–1524, 2001.

[5] A. Ptchelintsev and R. G. Maev, “Method of quantitative evaluation of elastic properties of metals at elevated temperatures,” *Review of Prog. in Quantitative Nondestructive Evaluation*, vol. 20, pp. 1509–1516, 2001.

[6] A. Chertov and R. G. Maev, “A one-dimensional numerical model of acoustic wave propagation in a multilayered structure of a resistance spot welds,” *IEEE Trans. UFFC*, vol. 52, no. 10, pp. 1783–1790, 2005.

[7] A. Chertov, A. Karloff, W. Perez, A. Lui, and R. Maev, “In-process ultrasound nde of resistance spot welds,” *BINDT Insight Journal*, vol. 54, no. 5, pp. 257–261, 2012.

[8] V. Kurz and B.Lux, “Lokalisierung der erstarrungsfront beim stranggießen von stahl,” *Berg- und Hüttenmännische Monatshefte*, vol. 5, 1969.

[9] A. Chertov and R. Maev, “A one-dimensional numerical model of acoustic wave propagation in a multilayered structure of a resistance spot weld,” *IEEE UFFC*, vol. 52, no. 10, pp. 1783–1790, October 2005.

Chapter 3

Expulsion Detection in Ultrasound M-Scans

Through the research conducted in this work, three identifiable signs of expulsion were discovered in ultrasound M-scans of the resistance spot welding process. These include:

1. Sudden changes in time of flight (measurable by phase delay) of certain reflectors due to geometric contraction, heat loss and changes in the non-linear reflection co-efficient.
2. Excessive heating due to poor electrical and/or thermal contact between plates and electrodes.
3. Excessive indentation after welding, measurable in the M-scan.

Prior to this work, the only observable indicator of expulsion was found by tracking the TOF position of the envelope of x_1 (group delay) for sudden changes. Attempts to rely solely on changes in this TOF measurement proved to be only somewhat reliable. In this work, additional indications of expulsion were identified in M-scan data and methods for detecting these indicators were developed. These methods are outlined in this chapter including the necessary theory, models and measurements used to verify them.

3.1 Detection Requirements

Before attempting to detect an expulsion, the physical nature of an expulsion must first be examined in terms of an ultrasound M-scan. Since expulsion can range from very weak surface sputtering to multiple expulsion events that remove a substantial portion of heat and material from the weld, the identifiable signs of expulsion should be sensitive only to events that compromise the overall weld strength without falsely detecting acceptable welds, weak expulsions, and sometimes unavoidable welding phenomenon like surface sputtering. In addition, not every expulsion produces a bad a weld and not every minor expulsion leaves a good weld, and so the classification of the severity of the expulsion must also be considered.

3.1.1 Pulse Repetiton Rate (PRR) Requirements

The first requirement for expulsion detection is the sampling rate of the M-scan. The A-scan pulse repetition rate must be fast enough to capture the expulsion event and distinguish it from natural welding phenomenon such as periodic heating and cooling when welding with AC or impulse current. Scanning with an ultra-high speed PRF of 12000 kHz was performed to determine the duration of an expulsion event. Fig. 3.1 shows one example of the data acquired with the high speed device where the primary reflections of the front surface were recorded with a PRF of 12 kHz and the through

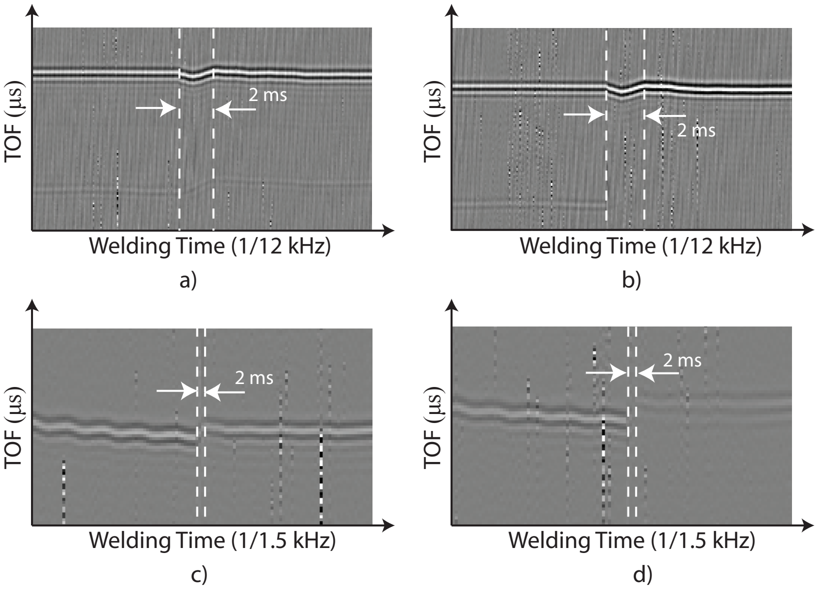

Figure 3.1: High speed M-scan images capturing the duration of an expulsion event. a) Front wall reflection during a faying interface reflection. b) Front wall reflection of a surface expulsion. c) and d) through transmission scans of a) and b) respectively.

transmitted signal was recorded at a PRF of 1.5 kHz to confirm the expulsion event.

A 5/8” electrode with a small tip face ($d_\text{e} = 4$ mm) was used to ensure expulsions would occur for a range of welding currents and also ensure that acoustic contact was not lost during the expulsion event. The average duration of an expulsion was approximately 3 ms with a minimum recorded expulsion time of approximately 1.5 ms and a maximum expulsion time of approximately 4.5 ms for this setup. This data was obtained for a series of 38 welds (30 expulsions) using 2T 1.5 mm bare mild steel plates and AC welding current that ranged from (8 to 12) kA. This setup was selected as a typical welding case not likely to generate substantial expulsions so that the weakest expulsions could be used to determine the minimum detection requirements. From this, the minimum required PRR for expulsion detection was obtained, showing ideally a PRR < 1.5 ms is required to detect the most mild cases of expulsion. Unfortunately, as described in Chapter 2, the current Inline hardware is capable of a stable PRR of 2 ms, which is used whenever possible throughout the remainder of this work, with an exception noted in Chapter 5. Generally, expulsions of shorter duration, such as those shown in Fig. 3.1 do not have a substantial impact on weld quality and can be ignored, while more sever instances of expulsion shown in the following sections are still detectable using a PRR of 2 ms.

3.1.2 Signal Integrity Requirements

Next, setup dependent issues with ultrasound signal integrity, such as lack of acoustic transmission during welding (due to electrode degradation) as well as physical and electrical noise, must be considered. Detection of expulsion must be robust against both the possibility that the internal weld structure may not be visible as well as cases where noise may obstruct the reflected ultrasound pulse or produce false signs of expulsion. The requirements for different levels of detection and classification are outlined as follows:

1. In order to fully detect and classify all cases of expulsion, all interfaces shown in Fig. 2.5 must be present and detectable.
2. For maximum detectability of expulsion phenomenon with uncertain classification, both the front wall and back wall reflections (x_1 and x_3 shown in Fig. 2.5) must be present and detectable in the M-scan prior to expulsion.
3. The minimum requirement for detection of expulsions is that the front wall (x_1 of Fig. 2.5) be present and detectable.
4. Finally, severe noise or hardware data errors cannot corrupt A-scans relevant to the moment of expulsion or obstruct the detection of reflected pulses.

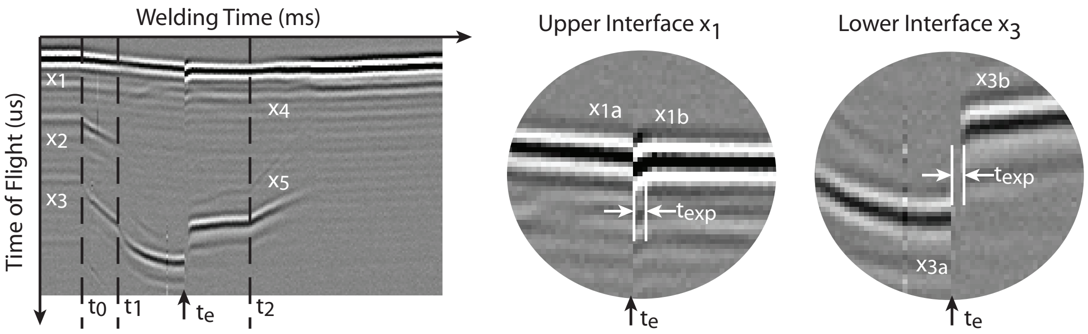

Figure 3.2: An example of an expulsion event captured in an M-scan image.

3.1.3 Classification Requirements

Finally, detected expulsions should be classified depending on their severity and the extent to which the expulsion may affect the yield strength of the weld determined by:

1. An undersized weld nugget.
2. The presence of large pits or voids.
3. Excessive indentation.
4. Substantial surface cracking.

Expulsions resulting in any or all of these signs must be fully detected in M-scans and classified as significant where possible.

3.2 Method 1: Expulsion Detection by Changes in Time Of Flight

The most prominent sign of an expulsion event during welding is a sudden change in the total time of flight through the weld zone. A good example of this observation is shown in Fig. 3.2.

The decrease in TOF between x_1 and x_3 at the time of expulsion t_e results from the sudden shift in interface x_3, which is measured by comparing the arrival time of x_{3a} with x_{3b} in Fig. 3.2. Corresponding to this, is a change in the reflection of the upper interface x_1, which is measured by comparing x_{1a} with x_{1b} in Fig. 3.2.

Theses changes in time of flight generally appear together, however, the cause of each has been identified as separate mechanisms. As such, these may appear alone or together, depending on the exact nature and cause of an expulsion. A surface expulsion can produce excessive indentation and create a pocket between the steel plate and electrode. This increase the current density at the contacting regions and increases heat generated at the tip of the electrode. When the upper interface x_1 exhibits a large shift, it is most likely due to a surface expulsion. A faying interface expulsion, on the other hand, does not always produce substantial indentation and good contact between the electrode and plates remain. In this case, there is little change in the upper interface reflection x_1.

The shift in interface x_3 is the result of two effects:

1. Physical indentation as material between the two electrodes is ejected from the weld resulting in a closer distance between electrodes (and hence a shorter TOF between x_1 and x_3.
2. A decrease reduction in the average temperature in the weld region between x_1 and x_3 as a result of molten material being removed from the weld zone, where the average speed of sound in this region increases with a decrease in temperature.

Both causes for this change in TOF are indicators of an expulsion that may have adverse effect on the final strength and quality of the weld.

The shift in interface x_1 results from a more complex interaction between the surface of the plate and electrode. Although this shift tends to appear with every expulsion event, it may be absent in M-scans where a weak expulsion has occurred. Before work in this thesis was conducted, it was believed that this shift in interface x_1 was the best indicator of an expulsion, since the interface x_1 appears most consistently between M-scans and tracking this interface for changes is quite simple. At that time the reason for this shift appearing was still unknown. Most peculiarly, the direction of the shift showed an increase in TOF from x_{1a} to x_{1b} which implies either a sudden expansion of the electrode or increase in temperature in the electrode. It was originally thought that this perturbation was more of a result of the mechanical energy exchanged and released as molten material was forcefully squeezed from the weld, however, further research into this event has revealed a more predictable nature and provides a plausible explanation, which can in turn be used to further classify the nature, severity and type of expulsion. This is explained in detail in the following section. Nonetheless, identifying this event is also crucial to reliably detecting and classifying expulsion.

Thus, the first form of expulsion detection is performed by measuring sudden changes in TOF in the upper and lower interfaces x_1 and x_3 which may occur *only* when welding current is on *and* after melting has occurred. Perturbations in these interfaces prior to melting and after current has been turned off result from changing contact conditions and loss of acoustic transmission into the workpiece, but *not* from expulsion.

3.2.1 Detecting Upper Interface Shifts

Prior to this work, expulsion detection in M-scans was performed by tracking the changes in group delay of adjacent A-scans. The group delay was found by the peak cross-correlation of adjacent A-scans. This proved to be quite ineffective as the resolution of the group delay is limited to one sample, or approximately 15 nS. Since the upper interface is continuously shifting due to heating and cooling of the system, single sample shifts occur quite frequently and non-periodically, and so only severe expulsions resulting in a shift larger than 30 nS (such as that shown in Fig. 3.2) could be detected by group delay alone.

In this work, shifts in the upper interface x_1 are detected by examining the phase delay of adjacent A-scans. It was observed that the phase delay of the center frequency component of the reflected pulse shows a more distinguishable shift at the moment of expulsion. The results in lab experiments show that even minor expulsions exhibiting a phase delay of less than 3 ns can be detected providing an order of ten improvement in the resolution for expulsion detection over group delay alone.

By comparing adjacent reflection x_{1a} with x_{1b}, significant phase delays should be present during expulsions but not during normal heating. For this to be true, the pulse repetition interval t_p should be set according to the requirements in Section 3.1.1. In this case, we can express adjacent A-scans as:

$$x_{1a}(t) = x_1(t) \tag{3.1}$$

$$x_{1b}(t) = x_1(t + t_p) \tag{3.2}$$

where t_p is the pulse repetition interval (time between A-scans.) For a real valued signal $x(t)$ the analytic signal $x_{\mathrm{a}}(t)$ can be formed such that:

$$x_{\mathrm{a}}(t) = x(t) + j\hat{x}(t) \tag{3.3}$$

where $\hat{x}(t)$ can be computed by the Hilbert Transform of $x(t)$.

In the frequency domain, this can be expressed as:

$$X(f) = X_{\mathrm{a}}(f - f_c)/2 + X_{\mathrm{a}}^{*}(-f - f_c)/2; \tag{3.4}$$

where X^* denotes the complex conjugate.

Assuming $x_{\mathrm{a}}(t)$ is the analytic signal of $x_{1a}(t)$ and assuming $y(t) = x_{1b}(t)$ is a real valued signal derived from $x_{1a}(t)$ with attenuation A, time delay t_d and center frequency shift θ_c, this transform can be expressed in the frequency domain as $G(f)$ with real-valued for $H(f)$:

$$G(f) = Ae^{-j(2\pi f t_d + \theta_c)} \tag{3.5}$$

$$H(f) = G(f - f_c) + G^*(-f - f_c) \tag{3.6}$$

In Equation (3.6), $H(f)$ is the equivalent transform applicable to real valued signals such that:

$$\begin{aligned} Y(f) &= H(f)X(f) \\ &= \frac{1}{2}G(f - f_c)X_{\mathrm{a}}(f - f_c) + \frac{1}{2}G^*(-f - f_c)X_{\mathrm{a}}^*(-f - f_c) \qquad (3.7) \\ y(t) &= Ax(t - t_d)\cos(2\pi f_c[t - t_d] + \theta_c) - jA\hat{x}(t - t_d)\sin(2\pi f_c[t - t_d] + \theta_c) \qquad (3.8) \end{aligned}$$

For an arbitrary transform $H(f) = A(f)e^{j\theta(f)}$, the group delay t_g and phase delay t_θ were found in [1, 2] as;

$$t_g = -\frac{1}{2\pi}\frac{d\theta(f)}{df}\bigg|_{f=f_c} = -\frac{\theta'(f_c)}{2\pi} \tag{3.9}$$

$$t_\theta = -\frac{1}{2\pi}\frac{\theta(f)}{f}\bigg|_{f=f_c} = -\frac{\theta(f_c)}{2\pi f_c} \tag{3.10}$$

For example, taking $\theta(f) = -2\pi[f - f_c]t_d + \theta_c$ from (3.6) and substituting into Equations (3.9) and (3.10), the result is $t_g = t_d$ and $t_\theta = \theta_c/(2\pi f_c)$.

The method applied to determine t_d and θ_c above was the analytic cross-correlation [3] as it has an efficient FFT based implementation with low computational complexity. In this method, the analytic cross-correlation between real valued signals $x(t)$ and $y(t)$ is defined by [2] in the frequency domain as:

$$C^a_{yx}(f) = \begin{cases} 2Y(f)X^*(f), & \text{for } f > 0 \\ Y(0)X^*(0), & \text{for } f = 0 \\ 0, & \text{for } f < 0 \end{cases} \tag{3.11}$$

It is shown in [3] that the equivalent time domain signal $c^a_{yx}(t)$ yields:

$$t_g = \max_t \left\{ |c^a_{yx}(t)| \right\} \tag{3.12}$$

$$t_\theta = \arg\{c^a_{yx}(t_g)\} \tag{3.13}$$

This was implemented using discrete time signals by [3] with $x[n] = x(nt_s)$ and $y[n] = y(nt_s)$ and $X[k] = \mathcal{F}\{x[n]\}$ and $Y[k] = \mathcal{F}\{y[k]\}$, where $\mathcal{F}$ denotes the Fast Fourier Transform.

The B-scan is first segmented to isolate the upper interface from the rest of the scan. A Hamming window is applied to the segmented data for reduce spectral leakage when performing spectral analysis on the interface data. The windowed data is zero padded to form the 2N-point FFT

Finally, the discrete-time 2N-point analytic cross-correlation transform is computed:

$$C^a_{yx}[k] = \begin{cases} Y[0]X^*[0], & k = 0 \\ 2Y[k]X^*[k], & 1 \le k \le N-1 \\ Y[N]X^*[n], & k = N \\ 0, & N+1 \le k \le 2N-1 \end{cases} \tag{3.14}$$

Zero padding C^a_{yx} by a factor of M in Equation (3.14) allows interpolation of the

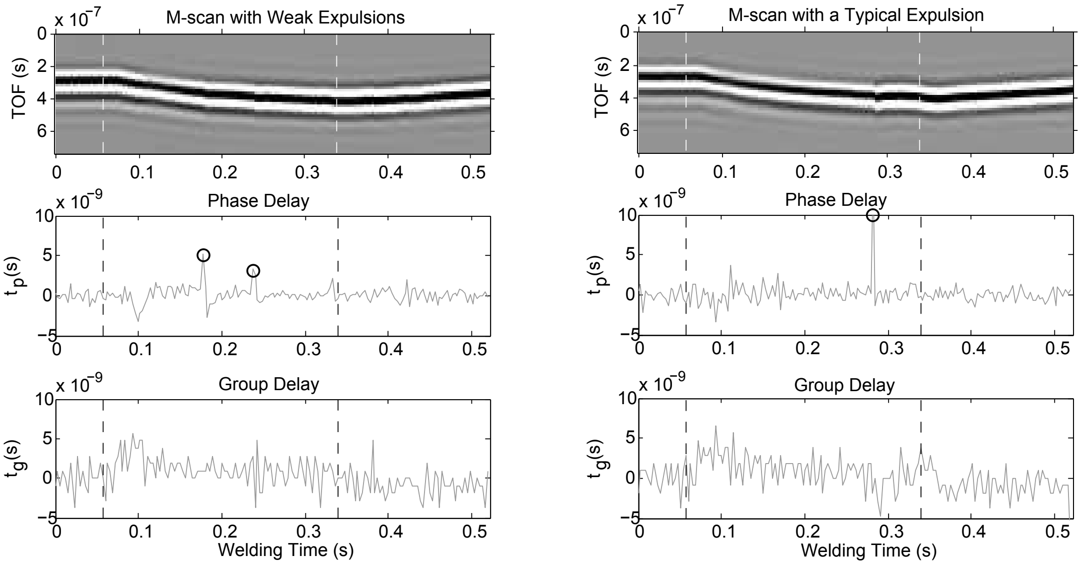

(a) (b)

Figure 3.3: Group delay t_g and phase delay t_θ plotted for the upper interface x_1 with: a) weak expulsions and b) a strong expulsion. The peaks in t_θ are circled at the moment of expulsion.

time domain cross-correlation $c^a_{yx}[n]$ to yield a $(2NM-1)$-point cross-correlation in which the time resolution increases from t_s to t_s/M. Similar to Equations (3.12) and (3.13), the group delay and phase delay are determined by:

$$n' = \max_n \left\{ |c^a_{yx}[n]| \right\} \tag{3.15}$$

$$t_g = n' t_s \tag{3.16}$$

$$t_\theta = \frac{\arg\{c^a_{yx}[n']\}}{2\pi f_c} \tag{3.17}$$

where f_c is take as the frequency location of the maximum in $|X[k]|$. Although $X[k]$ may not be exactly symmetric about it's peak, the discrepancy is negligible for the added simplicity of finding the peak value over the spectrum band edges.

Fig. 3.3 shows two example M-scan images with expulsions. Welding current was on between the two dashed lines, and in this region only is the phase delay data relevant. The widowed upper interface and the result of phase delay and group delay are shown for $M = 8$.

It is clear that even the very weak expulsions of Fig. 3.3a exhibited a significant change in phase delay, where as the interpolated group delay exhibits little to no distinguishable change over the regular interface shifts. The phase delay exhibits a positive peak because of an increase in TOF and so negative peaks can be ignored when searching for an expulsion.

3.2.2 Detecting Lower Interface Shifts

The best confirmation of an expulsion event in an ultrasound M-scan is when a sudden shift in the lower interface (x_3 in Fig. 3.2) can be observed. The same approach as above can be performed, only interpolation is not necessary since the expected shift in the interface is very large. The large shifts also makes it possible to detect the expulsion by simply considering the group delay as the peak of the cross-correlation of the real valued signals x_{3a} and x_{3b} where similar to Equations (3.1) and (3.2), $x_{3a}(t) = x_3(t)$ and $x_{3b}(t) = x_3(t + t_p)$. The problem with detecting shifts in the lower interface is that changing contact condition can results in loss of acoustic transmission through the workpiece and thus an absence (or very weak) reflection of the back wall.

Fig. 3.4 shows two examples of the the group delay and phase delay for the lower interface with and without expulsion. Again, welding current is only during the welding time between the dashed lines and only the group delay in this region is valid. In both cases the lower interface amplitude is strong enough to produce a reliable result. In cases where amplitude of the lower interface is too weak, the upper interface alone must be used. In both examples, a negative peak in the group delay occurs at the moment of expulsion since there is a decrease in TOF. Positive peaks

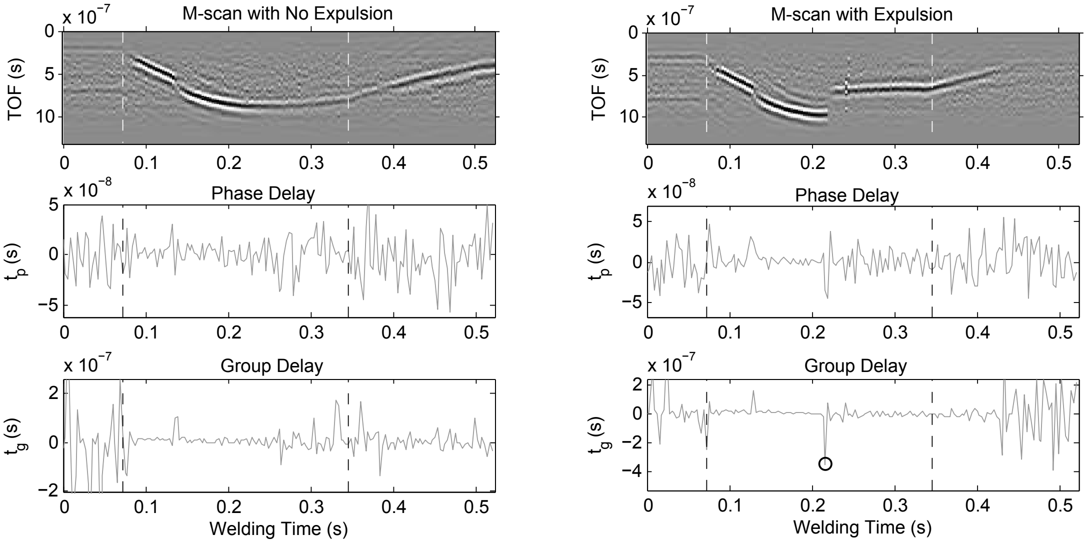

(a) (b)

Figure 3.4: Group delay t_g and phase delay t_θ plotted for the lower interface x_3 with: a) no expulsion and b) a normal expulsion. The peak in t_g is circled at the moment of expulsion.

can be ignored when detecting expulsion.

The condition used to determine whether or not the lower interface refection is strong enough to detect expulsion was the amplitude of the analytical cross-correlation $|c^a_{yx}|$. When the amplitude falls below a certain threshold, the group delay data for this interface can be ignored. In almost all industrial setups, the lower interface is weak at times when welding current is applied and thus not reliable enough for the outright detection of expulsions. In addition, the disappearance of the interface in the duration of the expulsion event makes tracking this interface non-trivial and so group delay shifts of x_3 are not considered further in this work.

3.3 Method 2: Measuring Heating Rates by Ultrasound

In this section, a novel method of measuring the heating rate of the workpiece in ultrasound M-scans has been employed and used as both an indicator and predictor of an expulsion. Direct observation of heating rates via high-speed cinematography of an edge weld was performed in [4] and effects of heating rates was extensively investigated in recent works [5].This new Inline ultrasonic work is likely one of the most significant contributions to the field of expulsion detection since direct and non-invasive monitoring of internal temperatures of the weld zone was not possible to this point in time.

The premise behind this method is that for a good welding schedule, an expulsion will result when excessive heat is generated due to:

1. Increased current density (electrode damage and misalignment.)
2. Decreased thermal conduction through the electrode-workpiece interface (as a result of cumulated oxide and debris on the tip face.)

One, or both cases will result in heat accumulating in the workpiece faster than expected. Detecting this with ultrasound is possible in real-time because the time of flight through the workpiece changes with temperature.

Thus, a simple model of heat generation and the relationship between TOF and the change in the average workpiece temperature was established considering the effects of both contact area and the electrode-workpiece thermal conduction co-efficient. This model was verified experimentally and used to establish threshold conditions in which expulsion, and even undersized welds, could be identified before they occur.

3.3.1 Heat Generation in Resistance Spot Welding

Fig. 3.5 shows the various interfaces and temperatures of interest when monitoring the spot welding process. When weld current is applied, T_0 remains constant at room temperature while temperatures T_1 and T_2 increase until T_2 reaches melting. At melting, temperature T_1 continues to increase as the molten nugget grows and the temperature T_{melt} at the solid steel to liquid nugget interface remains constant. Tracking the initial temperature increase at T_2 prior to melting ensures adequate heat generation while tracking the position of the interface at T_{melt} after melting occurs is necessary to measure the nugget penetration depth d_1. Both are critical to ensure a proper sized nugget is formed during the welding process. [6]

The focus in this work is on monitoring the temperature in the workpiece between interfaces T_1, T_2 and T_3 up to the melting point of interface T_2. This is accomplished by ultrasonically monitoring the average temperature in this region (between T_1 and T_3). Melting of interface T_2 occurs when the average temperature is sufficiently high enough to sustain a peak temperature equal to the melting temperature of the material. This average temperature at melting can be determined empirically, or via finite element simulations using the model in Chapter 1.

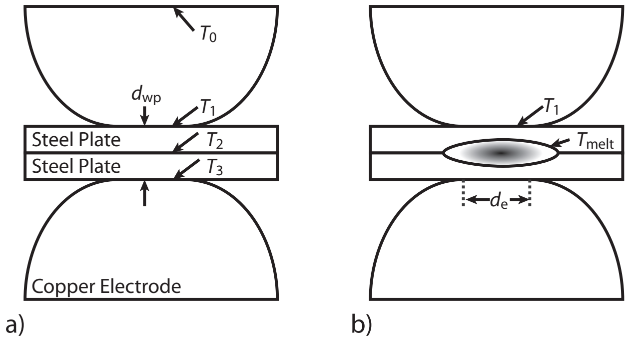

Figure 3.5: a) Initial welding stack prior to melting of two plates with workpiece thickness d_{wp}. b) Welding stack with a molten nugget interface temperature T_{melt}.

When welding current is applied to the workpiece, melting of the metal between the electrodes is achieved by joule heating according to 1.1, from which the instantaneous heat energy is:

$$q_{\text{heat}} = I_{\text{weld}}^2 R_{\text{weld}} \tag{3.18}$$

where q_{heat} is heat generation in W, I_{weld} is electrical current in A, and R_{weld} is the total electrical resistance of the work-piece between the electrodes in Ω. Additionally, heat loss through the electrodes, described in equation 1.3 must be considered, and can be expressed in terms of the the interfaces T_1 and T_0 as:

$$q_{\text{loss}} = (T_1 - T_0)\, h_c \pi \left(\frac{d_e}{2}\right)^2 \tag{3.19}$$

where q_{loss} is in W, T_1 is the temperature on the steel side of the work-piece in K while T_0 is the cooled copper electrode temperature in kelvin. For simplicity, T_0 is assumed to be constant in the electrode despite a temperature gradient present between T_0 and T_1 interfaces. Also, h_c is the thermal contact conductance coefficient of the interface express in W·K^{-1}·m^{-2}. This coefficient differs depending on contact condition, pressure, and surface coatings and is primarily responsible to variations in heating for constant weld setups. For general copper steel welding, h_c can vary by an order of magnitude of 10, ranging from 25 kW·K^{-1}m^{-2} to 250 kW·K^{-1}m^{-2} [7, 8].

During the first few cycles of welding, the interface T_1 softens and deforms giving rise to a large change in h_c, however, during this time the temperature difference across the interface T_1 is very low and so the effects of h_c on q_{loss} are low. By the time the temperature difference across T_1 becomes significant, h_c remains constant for the duration of the heating process. Thus, the value of h_c can be considered constant for the duration of welding.

Finally, the total heat energy in J generated over elapsed time t in s can be expressed as:

$$Q_{\text{total}}(t) = (q_{\text{heat}} - q_{\text{loss}})\, t \tag{3.20}$$

This heat energy is responsible for heating the steel workpiece from equation 1.5, which can be expressed as a function of time:

$$Q_{\text{weld}}(t) = mc_p \Delta T(t) \tag{3.21}$$

where m is the mass of the heat affected zone in kg, c_p is the specific heat capacity of the material in $\text{J}^{-1}{\cdot}\text{kg}^{-1}{\cdot}\text{K}^{-1}$ and $\Delta T(t)$ is the change in temperature in K, also expressed as function of current temperature $T(t) - T(0)$.

Additionally, m can be expressed as a function of the volume of material between the electrodes:

$$m = \pi \left(\frac{d_e}{2}\right)^2 \rho_m d_{\text{wp}} \tag{3.22}$$

where ρ_m in kg m^{-3} is the density of the material in the region being heated, with thickness d_{wp} in m under the tip contact area with diameter d_e in m. It is important to note that both R_{weld}, ρ_m and c_p are temperature dependent material properties that change over time with T during the welding process. Also, thermal expansion of the workpiece increases the value of d_{wp} with temperature, and thus d_{wp} must also be considered using the co-efficient of linear thermal expansion dL/L. In addition, the material properties change between the interfaces in the presence of strong temperature gradients. To simplify the heat transfer problem, the average temperature in the heat affected zone at a specific point in time t is considered:

$$\bar{T}(t) = \frac{1}{d_{\text{wp}}} \int_0^{d_{\text{wp}}} T(t, z) dz \tag{3.23}$$

where z is the distance from interface T_1.

Since material properties also vary with temperature, the temperature dependent material properties $R(T)$, $\rho(T)$ and $c_p(T)$, as well as the workpiece thickness $d_{\mathrm{wp}}(t)$, are simplified by writing:

$$\bar{R}(t) = R(\bar{T}(t)) \tag{3.24}$$

$$\bar{\rho}(t) = \rho(\bar{T}(t)) \tag{3.25}$$

$$\bar{c_p}(t) = c_p(\bar{T}(t)) \tag{3.26}$$

$$d_{\mathrm{wp}}(t) = d_{\mathrm{wp}}(0)(1 + dL/L(T(t))) \tag{3.27}$$

Equating equation 3.21 to 3.20 for a short duration of time δt, and substituting equations 3.24 - 3.26, we can express the corresponding increase in average temperature $\delta\bar{T}(t) = \bar{T}(t) - \bar{T}(t - \delta t)$ as:

$$\delta\bar{T}(t) = \frac{I_{\mathrm{weld}}^2 \bar{R}_{\mathrm{weld}}(t) - \pi\left(\frac{d_e}{2}\right)^2 h_c\left(\bar{T}(t) - T_0\right)}{\pi\left(\frac{d_e}{2}\right)^2 d_{\mathrm{wp}}(t)\bar{\rho}(t)\bar{c_p}(t)}\delta t \tag{3.28}$$

Since the change of temperature with time $\delta\bar{T}(t)/\delta t$ is a function of $\bar{T}(t)$ as well as non-linear temperature dependent functions $\bar{R}(t)$, $\bar{\rho}(t)$ and $\bar{c_p}(t)$, solving $\bar{T}(t)$ must be done numerically for small time increments $\delta t \approx \Delta t$. This is accomplished by solving the temperature at a discrete time step n, and using this temperature to determine the material properties and resulting increase in temperature $\delta\bar{T}[n] \approx \Delta\bar{T}[n]$, where $n = t/\Delta t$:

1) Starting with n=0, set the temperature for the current iteration:

$$\bar{T}[n] = \begin{cases} T_0, & \text{for } n = 0 \\ \bar{T}[n-1] + \Delta\bar{T}[n-1], & \text{otherwise} \end{cases}$$

2) Set the material properties for the current temperature.

$$\begin{aligned}\bar{R}[n] &= R(\bar{T}[n])\\ \bar{\rho}[n] &= \rho(\bar{T}[n])\\ \bar{c_p}[n] &= c_p(\bar{T}[n])\\ d_{\text{wp}}[n] &= d_{\text{wp}}[0](1 + dL/L(\bar{T}[n])\end{aligned} \tag{3.29}$$

3) Solve for the change in temperature:

$$\Delta\bar{T}[n] = \frac{\left(I_{\text{weld}}^2\bar{R}_{\text{weld}}[n] - (\bar{T}[n] - T_0)h_c\pi\left(\frac{d_e}{2}\right)^2\right)\Delta t}{\pi\left(\frac{d_e}{2}\right)^2 d_{\text{wp}}[n]\bar{\rho}[n]\bar{c_p}[n]} \tag{3.30}$$

4) Repeat from 1) using $n = n + 1$.

It should be re-enforced that unlike other methods where the temperature distribution between two interfaces is approximated by ultrasound measurement [9] [10], the proposed method for thermal process monitoring operates on the average temperature in a region and how it changes over time as a result of joule heating.

During monitoring, the estimated heat generation model above can be used to predict expected heating given a specific setup and know variability, and determine the real-time changes in the coefficient of thermal conduction at the copper steel interface. The first point can act as a basis of comparison when evaluating the quality of the weld/welding process, while the second point can be used in real-time feedback systems, where control over welding current I_{weld} can counteract overheating and under heating that result in variation of the thermal contact conductivity co-efficient h_c.

Fig. 3.6 shows the simulated heating rate using the simple heating model above

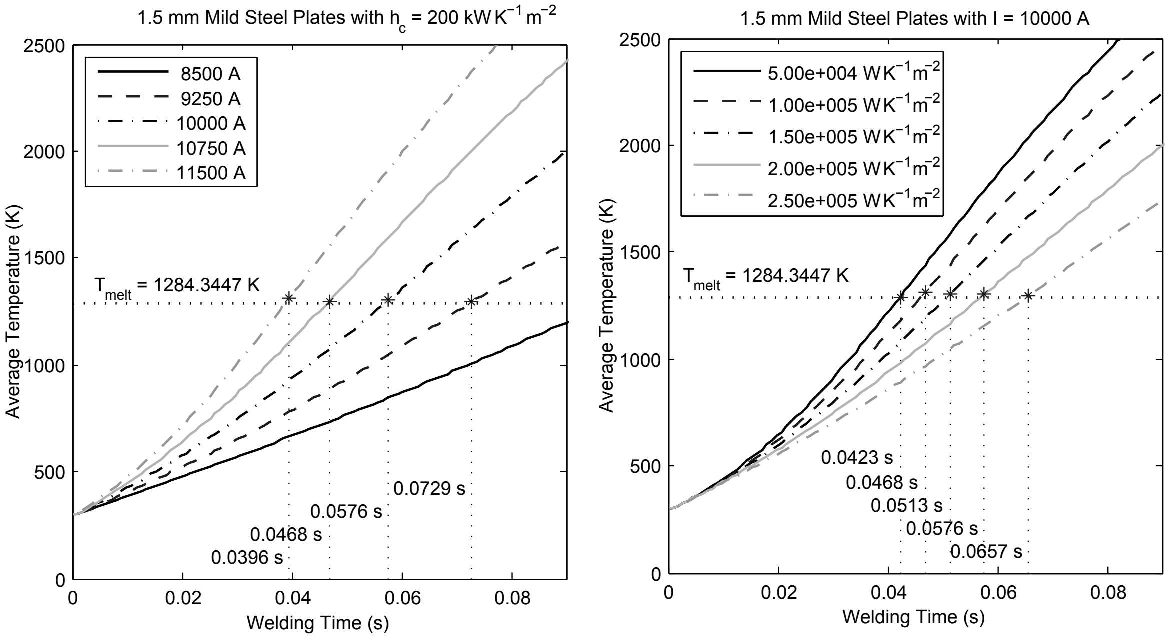

(a) Variation in melting time for constant h_c and changing weld currents.

(b) Variation in melting time for constant welding current with changing h_c.

Figure 3.6: Melting time as a result of changing welding current and thermal conduction coefficient h_c.

for cases of varying current in Fig. 3.6a and for varying thermal conduction coefficient h_c in Fig. 3.6b. The model considered the temperature dependent properties of 1080 steel from MPDB v7.11 welded with 3/4" electrodes with 5 mm tip face diameter and 2T 1.5 mm thick, uncoated, polished plates. A threshold for the heating rate (melting time) that results in an expulsion is experimentally determined, after which the modeled heating rates above can be used to ensure welding remains within an acceptable range. From previous experiments it is generally accepted that for the setup modeled in Fig. 3.6 that melting time < 0.06 s results in expulsion, melting time between (0.07-0.1) s produces good welds and melting time > 0.1 s results in undersized welds or stick welds. These melting times correspond to 12 cycle DC welding of 2T (1.5-1.5) mm GI HSS and Mild steel plates.

3.3.2 Ultrasound Monitoring

The primary mechanism for monitoring the dynamic thermal process is observing changes in TOF of reflected ultrasound pulses from the upper and lower interfaces T_1 and T_3 of Fig. 3.5 with corresponding ultrasonic reflection x_1 and x_3, since the longitudinal speed of sound in isotropic solids changes with temperature T. Fig. 2.4 of Chapter 2 showed the longitudinal speed of sound for a mild steel.

At this point, the measured TOF of a reflected pulse $x_i(t)$ for an A-scan taken at time $t = nt_p$ is the offset time $t_i(t)$. In Chapter 2, t_i was defined as the TOF delay from the i'th reflector in $h(t)$. Since $h(t)$ changes from A-scan to A-scan, the position of a reflector t_i also changes with time, hence $t_i(t)$. So, for simplicity, we can consider that the delay t_i for a given reflector at A-scan time t can simply be expressed as:

$$tof(x_i(t)) = t_i(t) \tag{3.31}$$

Thus, the TOF difference between x_1 and x_3 for a given A-scan is:

$$tof_{31}(t) = tof(x_3(t)) - tof(x_1(t)) \tag{3.32}$$

The change in time of flight between A-scan is thus:

$$\Delta tof_{31}(t) = tof_{31}(t) - tof_{31}(t - t_p) \tag{3.33}$$

In order to know the average temperature in the workpiece at a given A-scan, the rise in temperature between each A-scans $\Delta\bar{T}(t)$ must be known, and can be determined from the change in TOF $\Delta tof_{31}(t)$.

Substituting $\Delta\bar{T}(t) = \bar{T}(t)-\bar{T}(t-t_p)$ in Equation (2.12), the change in longitudinal velocity $\Delta c_l(\Delta\bar{T}(t))$ resulting from the change in temperature is:

$$\Delta c_l(\Delta\bar{T}(t)) = c_l(\bar{T}(t-t_p)) + k_v\Delta\bar{T}(t) \tag{3.34}$$

which is simplified to:

$$\Delta\bar{c}_l(t) = \bar{c}_l(t-t_p) + k_v\Delta\bar{T}(t) \tag{3.35}$$

The resulting change in TOF for a pulse echo traveling through the workpiece and back can then be expressed as:

$$\Delta tof_{31}(t) = 2\left[\frac{d_{\text{wp}}(t)}{\bar{c}_l(t-t_p)+k_v\Delta\bar{T}(t)} - \frac{d_{\text{wp}}(t-t_p)}{\bar{c}_l(t-t_p)}\right] \tag{3.36}$$

Since $d_{\text{wp}}(t)$ changes by less than once percent for a temperature change of 1000 K for most steels, the difference between $d_{\text{wp}}(t)$ and $d_{\text{wp}}(t-t_p)$ can be considered negligible and so Equation (3.36) can be written as:

$$\Delta tof_{31}(t) = 2d_{\text{wp}}(t-t_p)\left[\frac{1}{\bar{c}_l(t-t_p)+k_v\Delta\bar{T}(t)} - \frac{1}{\bar{c}_l(t-t_p)}\right] \tag{3.37}$$

Equation 3.37 can then be solved for the increase in temperature between two A-scans, which in turn can determine $d_{\text{wp}}(t)$ and $\bar{c}_l(t)$ for the next A-scan. The total average temperate of the workpiece is simply:

$$\bar{T}(t) = \int_0^t \Delta\bar{T}(t')dt' + \bar{T}(0) \tag{3.38}$$

Equation (3.37) can also be used to prediction the next ultrasound pulse location from the backwall x_3, but more importantly, provides a means of tracking temperature for real-time feedback control. If $\bar{T}(t)$ determined by Equations (3.38) and (3.37) using measured $\Delta tof_{31}(t)$ is lower than a modeled $\Delta\bar{T}$ from Equation (3.28) for a good weld, then the present heating rate is insufficient and the welding current must be increased. On the other hand, if the measured $\Delta\bar{T}(t)$ exceeds a modeled threshold, then excessive heating is occurring and an undesired expulsion event is likely to occur. In this case, the welding current must be decreased.

Since small changes in TOF result from relatively large changes in temperature, the accuracy of monitoring the temperature in thin plates depends highly on the accuracy of Δtof measurements. Thus, a robust method for accurately determining TOF must be employed that is suitable for real-time operation. The most difficult part of Inline temperature monitoring is accurately identifying the precise change in TOF between the physical interfaces x_1 and x_3. The method of pulse detection used for real-time interface tracking is presented in full in Chapter 4.

3.3.3 Verifying the Heating Model

The heating model and relationship to TOF determined in this section was verified using real welding setups in the lab setting. In these experiments, h_c was controlled by polishing both the steel plates and electrodes after each weld. This ‘perfect’ interface was used to determine the initial h_c value of 2.25×10^5 W·K^{-1}·m^{-2}. Stacks of dissimilar thickness were welded to assure that the model which considered a continuous workpiece thickness and disregarded contact resistance could still be applied.

Fig. 3.7 shows a comparison of the modeled heating rate vs. the Inline heating rate in terms of measured vs. modeled TOF. The time of melting is plotted to compare the accuracy of both the model and real results, including the estimated time at which melting began. All parameters were kept constant between models with the exception of the welding current which was used to control the heating rate. Similar comparisons were performed on varying plate thicknesses, materials and coatings and

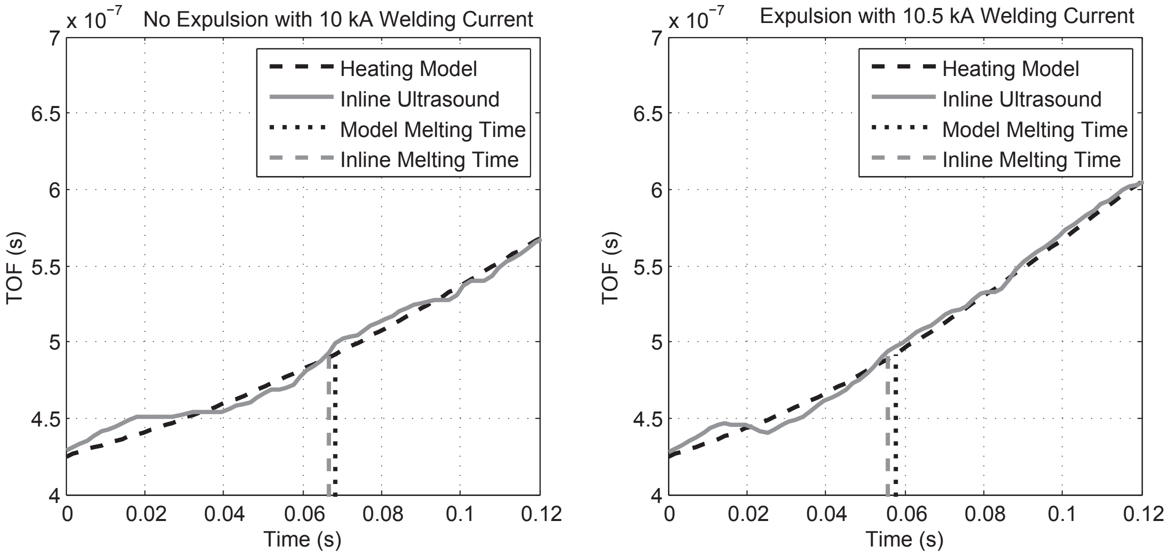

(a) (b)

Figure 3.7: 2T workpiece (1.15 mm - 1.35 mm) HDG HSS plates welded: a) 10 kA without expulsion and b) 10.5 kA with faying interface expulsion.

are presented in Chapter 5. An interesting thing to note is the initial overheating in both Fig. 3.7a and Fig. 3.7b, which is likely due to the imperfect contact and the presence of finite contact resistance. By about 0.02 s, the interfaces soften and the interface resistance no longer plays a significant role, as per the modeled assumptions, and both TOF curves continue as expected.

Although the model seems in close agreement, the most important feature to extract for the prediction and detection of expulsions is the melting time. The modeled melting time in Fig. 3.6 was taken as the mean of a Gaussian distribution with peak at the melting temperature of mild steel taken as 1700 K and interfaces T_1 and T_3 taken at 725 K from [11]. The actual melting time in Fig.3.7 was empirically determined by manually inspecting a number of M-scans and measuring $tof_{31}(t_{\mathrm{melt}})$ by observing the disappearance of the faying interface x_2. The average TOF determined temperature value for the workpieces of Fig.3.7 was 1284.10 K with a corresponding wave velocity $\bar{c}_l(t_{\text{melt}}) = 5030\ \text{m}\cdot\text{s}^{-1}$, showing good agreement.

3.3.4 Heating Rate Thresholds

Monitoring the heating rate of the workpiece can be used to detect the time it takes for melting to take place. This is the welding time from when the welding current is turned on, until the first onset of melting in the workpiece. This time can be used to estimate the heating rate of the plates and can proved a threshold for the detection of expulsion.

Since the melting time is determined by monitoring the TOF between the upper and lower interfaces of the workpiece x_1 and x_3 in a given A-scan, the accuracy of determining the melting time is a function of:

1. The M-scan PRR.
2. Variation in TOF at melting.

As outlined in Section 3.1, the maximum required PRR for accurate detection of expulsion is 2 ms. The variation in TOF was determined experimentally using 165 welds over three different setups. The results of this data for establishing a heating rate threshold with error considerations are presented in Chapter 5.

3.4 Method 3: Excessive Indentation

One major cause of excessive indentation is an expulsion, where molten material is ejected from the heat affected zone during welding; although not every instance of an expulsion results in a bad weld. This section discusses how the measurement of indentation can be used to detect expulsions and even assess the severity of the expulsion and the resulting quality of the weld joint. The relationship between indentation and weld quality was first shown by Wu [12] and subsequently used to assess quality in real-time [13, 14, 15, 16]. Particularly, the distinction between indentation resulting from expulsions, good welds and stick welds was reported on in [16]. Thus, it seemed to remain in line and competitive with current methods of expulsion detection and quality evaluation, indentation also needed to be monitored using the Inline system. This is another significant contribution to ultrasound NDE of spot welds since real-time in-process measurement of indentation using ultrasound has not been accomplished, until now.

The amount of indentation depends on a number of various welding factors includeing: material hardness, squeeze force, duration of welding and the geometry of the caps. Thus, the acceptable amount of indentation depends on the specifiec setup, workpiece and quality requirements of the industry. For this reason, classifying a weld based on the ultrasonic measure of indentation is only possible to the accuracy in which indentation can be measured.

3.4.1 Determining Indentation in a Heated Plate

The primary challenges that arise when performing accurate ultrasonic measurements during the welding process results from strong temperature gradients and the dependence of ultrasound velocity on temperature. The temperature dependence of the speed of sound in steel was outlined in Chapter 2 and was shown to be inversely proportional to temperature, characterized by k_{v}. Thus, the effects of heating increases TOF through the weld and the thickness of the plates due to thermal expansion. Contrary to this, indentation decreases the distance between copper electrodes, resulting in a decreased TOF.

Prior to this research, it was thought that separating these effects in an M-scan image was impossible and thus the only way to measure indentation was to wait for the weld to cool to room temperature where the speed of sound was known and only the final plate thickness affected the total TOF. One major contribution in this work was the idea that the effects of heat on TOF could be separated from the geometric contraction and thermal expansion of the plates. In order to accurately measure geometric dimensions in real-time M-scans, the temperature profile, or a suitable average temperature, at the point in time of measurement must be known. The proposed method for measuring indentation is based on the premise that the temperature distribution in the weld stack is constant and known at one specific time in the M-scan; the point of nugget solidification. The conditions for which the liquid nugget solidifies does not vary greatly from weld to weld, and at this precise point during the cooling process t_{ind}, the average speed of sound through the workpiece is known.

With a measured TOF through the workpiece, expressed in terms of Equation (3.32) at the moment of solidification, is given by:

$$tof_{31}(t_{\text{ind}}) = tof(x_3(t_{\text{ind}})) - tof(x_1(t_{\text{ind}})) \tag{3.39}$$

where again $tof(x_3(t_{\text{ind}}))$ is the TOF position of the reflection x_3 at the moment of solidification t_{ind} (and the same applies to x_1), then the total thickness of the workpiece at this point in time can be calculated as:

$$d_{\text{ind}} = \big(k_v(\bar{T}_{\text{ind}} - T_0) + c_l(T_0)\big)\;\; tof_{31}(t_{\text{ind}}) \tag{3.40}$$

where,

$$\bar{T}_{\text{ind}} = \frac{1}{d_{\text{ind}}} \int_{-d_{\text{ind}}/2}^{d_{\text{ind}}/2} T_{\text{ind}}(x)dx \tag{3.41}$$

Given that the temperature distribution during cooling can be approximated by a quadratic, determined from the FEM simulations of Chapter 1 to have the following form:

$$T(d) = -Ad^2 + B \tag{3.42}$$

where the average temperature in the workpiece at the moment of solidification has a peak temperature T_{melt} and temperature at the contact interface T_1. Thus, the temperature through the workpiece at time t_{ind} can be expressed as:

$$T_{\text{ind}}(d) = -4\frac{(T_{\text{melt}} - T_1)}{d_{\text{ind}}^2}d^2 + T_{\text{melt}} \tag{3.43}$$

Substituting Equation (3.43) into Equation (3.41) yields:

$$\bar{T}_{\text{ind}} = T_{\text{melt}} - \frac{1}{3}(T_{\text{melt}} - T_1) \tag{3.44}$$

which can be substituted into Equation (3.40) to determine the plate thickness.

Finally, thermal expansion of the plates must be considered. For most low carbon steel, the linear expansion co-efficient at the mean temperature at solidification ($\bar{T}_{\text{ind}}$ ≈1500 K) is approximately $dL/L = 0.01$ (from MPDB v7.11). Thus d_{ind} from Equation (3.40) should be corrected by this factor, in a similar manner in which the thermal expansion of d_{wp} was considered in Equation (3.27).

3.4.2 Identifying the Solidification Point

The main objective behind the proposed algorithm is to locate and trace reflections in the B-scan data during the welding process in order to identify the point in time when the liquid nugget completely solidifies. The details of finding the boundaries of the liquid nugget during it's solidification and tracing these boundaries to the point

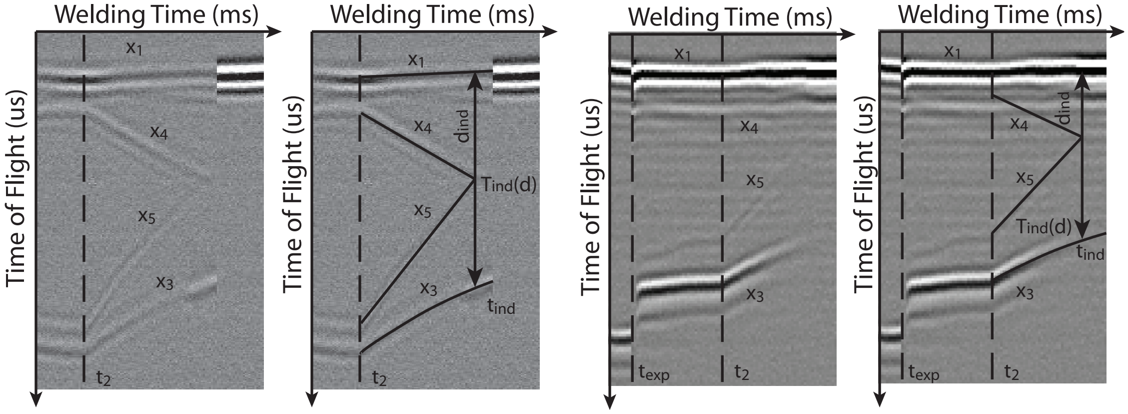

(a) Solidification of a good weld.

(b) Solidification after an expulsion.

Figure 3.8: The solidification of the nugget boundaries x_4 and x_5 join at the point t_{ind} at which indentation can be determined.

of complete nugget solidification is outlined in greater detail in Chapter 4.

The interfaces of interest are the two that result from the upper and lower boundaries of the nugget during solidification, shown as x_4 and x_5 in Fig. 2.5.

Fig. 3.8 shows an example of two M-scans, highlighting the region where the liquid nugget solidifies. In order to measure indentation in the M-scan, all four interfaces (x_1, x_3, x_4 and x_5) must be accurately identified. For most good welds, the interfaces are clear, however, in cases of expulsion, it is common for the interfaces to appear weak as a result of poor acoustic contact. Tracing x_4 and x_5 is only possible after processing the M-scan as discussed in Chapter 4.

3.4.3 Indentation in Real Welds

A series of welds with varying welding currents were made using 2T 1.5 mm GI HSS plates, where indentation and the TOF from the corresponding M-scan at the point of solidification were both measured. The measurements were compared to the theoretically determined plate thickness using Equations (3.40) and (3.44) with

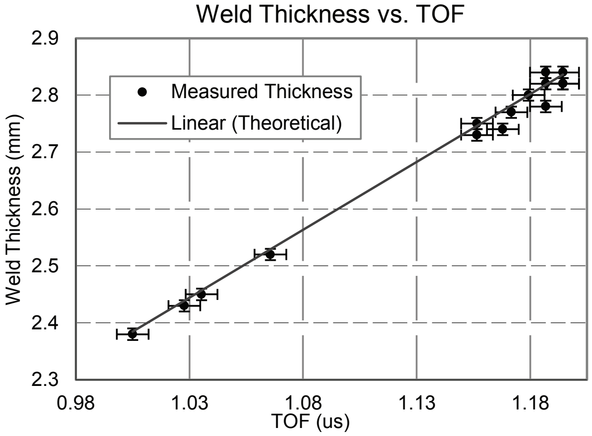

Figure 3.9: Measured weld thickness vs Ultrasound TOF in a 2T 1.5 mm workpiece.

$T_{\text{melt}} = 1700°K$ and $T_1 = 850°K$ determined by the FEM model of Chapter 1 and measurements performed in [11]. The results were plotted in Fig. 3.9. The thickness of the workpiece was physically measured using a digital caliper at three points and averaged with accuracy of ±0.01 mm and TOF at solidification was determined from the M-scans at the point where x_4 and x_5 merged with accuracy of ±7.6 ns. Fig. 3.9 shows the very strong correlation between TOF at the point of solidification and the final weld thickness, indicative that even for varying weld currents and nugget sizes, the assumption of a constant temperature distribution from weld to weld remains true. The results also show that the theoretical model for measuring indentation is quite accurate.

The lack of data points in Fig. 3.9 between TOF of 1.08 μs and 1.13 μs is naturally occurring and represents the significant increase in indentation when an expulsion occurs. The four welds with TOF less than 1.08 μs where all expulsions where as all welds with TOF greater than 1.13 μs were all good welds.

Since there is a strong linear relationship between TOF and weld thickness, the proposed method can still be used in the absence of accurate material data and temperature information at solidification simply by empirically determining the equivalent average velocity through the workpiece at the moment of solidification for a specific setup. For the data acquired in Fig. 3.9, a linear fit through the data points yields an R-squared value of 0.9919 and by considering the expansion of the workpiece to simply decrease the equivalent average wave velocity, indentation can be measured simply by:

$$d_{\text{ind}} = tof(t_{\text{ind}})c_{l\text{eq}} \tag{3.45}$$

where, $c_{l\text{eq}}$ is one over the slope of the linear fit through the data points of Fig. 3.9.

3.4.4 Indentation and Expulsion Detection

To validate the assumption that the temperature distribution through similar plate stacks remains constant from weld to weld, an additional series of 1.5 mm and 2 mm GA HSS plates were welded and evaluated using the proposed method. The results are shown in Fig. 3.10a and Fig. 3.10. The shaded region shows the range of indentation acceptable for producing good welds as outlined in [15] and [17].

To validate successful expulsion detection, each weld was visually monitored during welding and the observed results compared with the ability of the proposed algorithm to detect the event. The minimum indentation resulting from welds that exhibited expulsion was averaged with the maximum indentation resulting from welds that did not exhibit expulsion to determine an expulsion limit (Fig. 3.10a and Fig. 3.10b). Welds with expulsion identified in M-scan data were marked with a star. The results indicate that each case of expulsion was successfully identified by the proposed method.

Finally, the mean squared error (MSE) of M-scan measurements was evaluated for both 1.5 mm and 2 mm plate stacks to ensure the empirically derived average velocity from a 2T 1.5 mm workpiece can be applied to similar setups (e.g. 2 mm

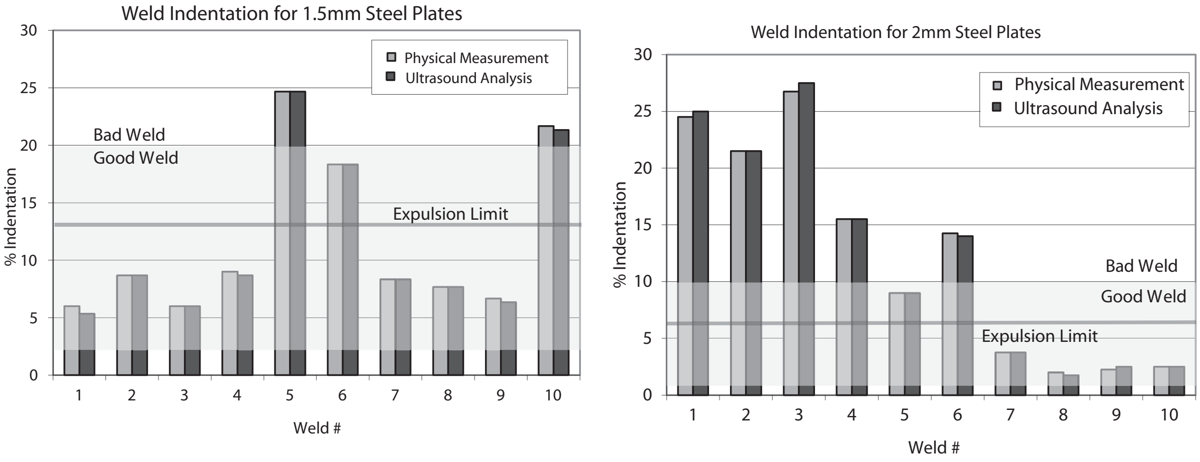

(a) 1.5 mm plates with expulsions on welds 5, 6 and 10.

(b) 2 mm plates with expulsions on welds 1-6.

Figure 3.10: Physically measured vs. Inline Ultrasound determined percentage indentation in 2T HSS plates.

plates.) Standard error was computed as the root of the MSE and was calculated to be 0.0084mm and 0.0126mm for 1.5mm and 2mm plates respectively.

3.4.5 Expulsion Classification by Indentation

This method demonstrated how expulsions can be detected by measuring indentation ultrasonically in-process. It has been confirmed that expulsions generally result in excessive indentation, but not always to the point of generating what is considered a bad weld by various industrial standards. The indentation measured via Inline ultrasound was able to distinguish expulsion events that resulted in good and bad welds. Thus the proposed method provides not only an adequate method for detecting expulsion, but for using indentation to additionally assess the quality of the welded joint.

3.5 Summary

In this Chapter, three methods for expulsion detection were presented. Method 1 demonstrated a very reliable way to detect expulsions by observing the effects of changing TOF due to cooling and sudden plate deformation. Of particular significance are methods 2 and 3, which present not only means of reliably detecting expulsion events, but in the case of Method 2, predicting events and in the case of Method 3, classifying events.

References

[1] J. Bendat and A. Piersol, *Random Data Analysis and Measurement Procedures S.E.* New York: Wiley, 1986.

[2] A. Papoulis, *Signal Analysis.* New York: McGraw-Hill, 1977.

[3] S. Marple, "Estimating group delay and phase delay via discrete-time "analytic" cross-correlation," *IEEE Trans. Signal Processing*, vol. 47, no. 9, pp. 2604–2607, 1999.

[4] C. Lane, C.D.Sorensen, G.B.Hunter, S.A.Gedeon, and T.W.Eagar, "Cinematography of resistance spot welding of galvanized steel sheet," *Welding J.*, vol. 66, no. 9, pp. 260–s – 265–s, 1987.

[5] T. loulou, P. L. Masson, and P. Rogeon, "Thermal characterization of resistance spot welding," *Numerical Heat Transfer, Part B*, vol. 62, no. 5.

[6] A. Chertov, A. Karloff, W. Perez, A. Lui, and R. Maev, "In-process ultrasound nde of resistance spot welds," *Insight NDT and Cond. Mon.*, vol. 54, no. 5, pp. 257–261, 2012.

[7] T. Eagar, "The physics of welding," in *Adv. Tech. in Weld 5th Proc.*, vol. 1, April 1990, pp. 11–16.

[8] H. Zhang and J. Senkara, *Resistance Welding Fundamentals and Applications.* CRC Press Taylor & Francis Group, 2006.

[9] I. Ihara and M. Takahashi, "Ultrasonic method for measuring internal temperature profile in heated materials," *Review of Prog. in Quantitative Nondestructive Evaluation*, vol. 27, pp. 1505–1511, 2008.

[10] A. Chertov and R. G. Maev, "Inverse problem solution to find real-time temperature distribution inside the spot weld medium using ultrasound time of fight

methods," *Review of Prog. in Quantitative Nondestructive Evaluation*, pp. 1492–1498, 2003.

[11] A. Karloff, A. Chertov, J. Kocimski, P. Kustron, and R. Maev, "New developments for in situ ultrasonic measurement of transient temperature distributions at the tip of a copper resistance spot weld electrode," in *Int. Ultrason. Symp.*, Oct 2010, pp. 1424–1427.

[12] K. Wu, "Electrode indentation criterion for resistance spot welding," *Weld. J.*, vol. 10, pp. 472–478, Oct. 1968.

[13] C. Ji and Y. Zhou, "Dynamic electrode force and displacement in resistance spot welding of aluminum," *Trans. ASME, J. Manuf. Sci. Eng.*, vol. 126, no. 3, p. 605610, Aug. 2004.

[14] J. Z. Chen and D. F. Farson, "Electrode displacement measurement dynamics in monitoring of small scale resistance spot welding," *Meas. Sci.Technology*, vol. 15, no. 12, pp. 2419–2425, Dec. 2004.

[15] Z. Xiaoyun, Z. Yansong, and C. Guanlond, "Weld quality inspection based on on-line measured indentation from servo encoder in resistance spot welding," in *Proc. Instrumentation and Measurement Technology Conf.*, April 2006, pp. 1353–1356.

[16] L. Xinmin, Z. Xiaoyun, Z. Yansong, and C. Guanlong, "Weld quality inspection based on online measured indentation from servo encoder in resistance spot welding," *IEEE Trans. Instr. and Meas.*, vol. 56, no. 4, pp. 1501–1505, Aug. 2007.

[17] D. Stocco, R. Magnabosco, and R. Barros, "Analysis of spot weld joints by ultrasonic inspection, fem and residual stress measurements," in *16th World Conference on NDT*, vol. 9, 2004.

Chapter 4

Ultrasound M-scan Processing

4.1 A-scan Noise Reduction and Filtering

Noise in the Ultrasound M-scans is problematic, especially in a noisy industrial environment. The following sources of noise were identified from an analysis that was part of this work and include:

1. Strong electromagnetic (EM) fields induced from the large welding currents.
2. Thermal excitation of the workpiece in strong temperature gradients.
3. Mechanical vibration of the workpiece and equipment.
4. Capacitive and resistive coupling of the welding voltage to the embedded transducer.
5. Conducted and radiated EM interference from industrial electric motors and robot servos and DC stepper motors that are nearby or contacting the welding equipment.

6. Noisy supply voltage and ground loops.

Previous experience with a number of welding environments has shown that the nature of the noise in an M-scan is highly setup and location dependent. Of the many sources of noise present in an Inline M-scan, the most difficult to deal with is noise induced from DC stepper motors, as this noise is broadband and overlaps with the spectrum of the ultrasound used in the system. DC stepper noise is non-periodic in the intervals in which it appears and can be strong enough to saturate the acquired data.

To combat random noise, a number of A-scans are averages after A/D conversion. The number of A-scan that can be averaged is limited due to the maximum PRR of the system and the fact that the system being probed is only quasi-stationary in a short windows of time. For this reason, 4x A-scan averaging is permitted with 250 μs delays between averaged A-scans. Faster scanning results in overlapping signals where multiple reflections from the previous acoustic pulse are still present during subsequent A-scans. Fig. 4.1 shows some results of A-scan averaging. The averaged A-scans are then transmitted to a PC where they must be further filtered to remove deterministic noise, electronic noise and noise signal overlapping the signal band.

The primary method of filtering noise in A-scans is by Band-pass filtering. The frequency spectrum of the desired ultrasonic radio frequency (RF) data was first determined. It was determined that the desired passband of the filter should encompass frequencies in the range of 5 MHz to 22 MHz and to reduce the order of the filter, the transition bands were permitted to be 4 MHz. The resulting Type-I FIR bandpass filter is used extensively to filter the A-scan data prior to any further processing and is effective at removing sources of noise 1-4 and 6 above.

The remaining coherent noise and noise within the bandwidth of the ultrasound signal is quite difficult to deal with. The most troublesome noise resulted from stepper

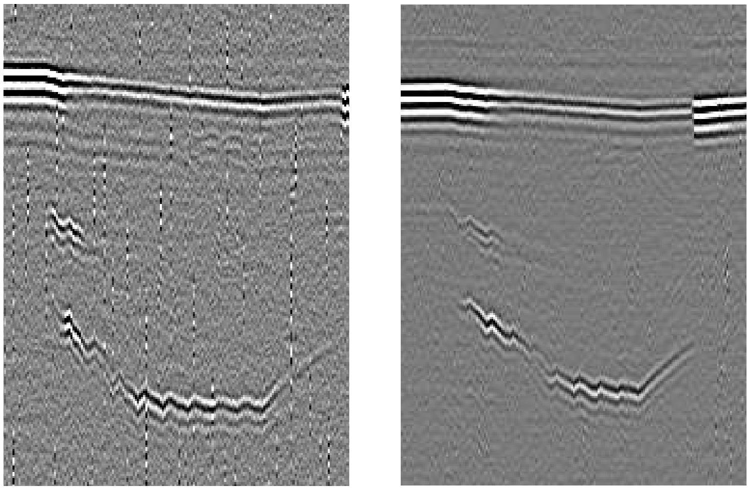

(a) (b)

Figure 4.1: Examples of noise reduction by averaging. a) No averaging. b) 8x A-scan averaging.

motors, which exhibited a varying spectrum in the range of 5 MHz to 15 MHz. This noise would appear at random intervals and for random durations in an M-scan. When stepper motor noise interferes with reflections from the desired interfaces, the result is detrimental to further processing of the M-scan. Examples of the levels of noise potentially present in an industrial M-scan are shown in Fig. 4.2.

One of the primary discoveries by the author regarding noise in the setup was that the main source of noise found in M-scans resulted from conduction through the water channel. It was observed that the strength of the servo noise present in M-scan data was inversely proportional to the resistance between the welding electrode (where servo noise was physically measured) and the isolated terminals of the transducer. It was postulated that repeated heating and cooling of the electrodes in the welding environment degraded the insulation around the electrical contacts to the transducer and that ionization of water surrounding these failure points resulted in a finite resistance between the welding electrode and transducer terminals. It was observed that dry or new transducers had extremely high resistance between

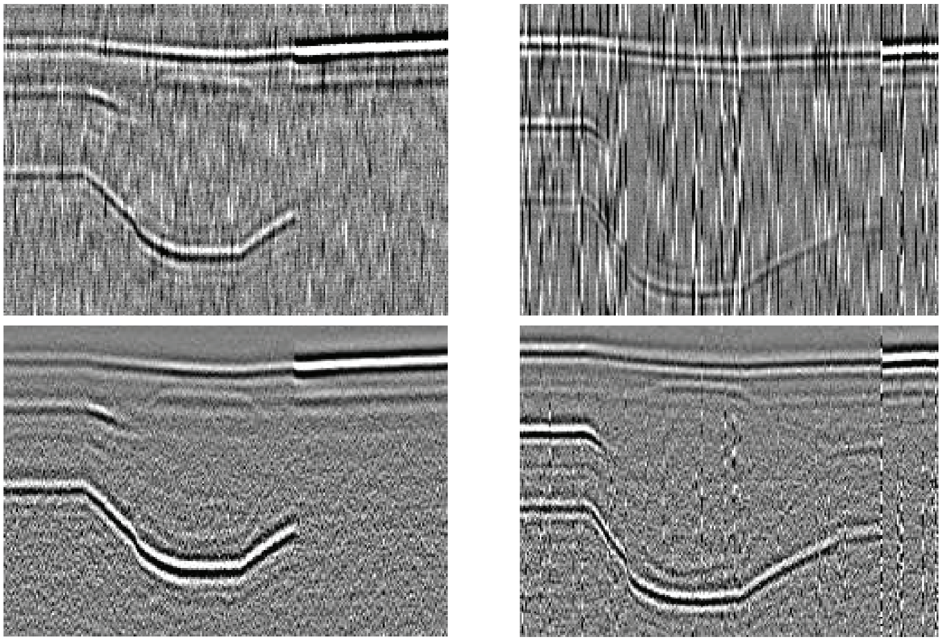

(a) (b)

Figure 4.2: Examples of Servo motor noise in industrial M-scans without A-scan averaging: a) $R > 250k\Omega$ before filtering (top) and after bandpass filtering (bottom) b) $R < 10k\Omega$ before filtering (top) and after bandpass filtering (bottom)

the electrode and transducer and thus exhibited very little stepper motor noise while frequently used transducers had a decreasing resistance over time when left in the cooling water stream and a corresponding increase in the appearance and strength of stepper motor noise in M-scans. A suitable solution to protecting the transducer is outside of the scope of this dissertation, but this discovery is essential to evaluating the performance of the expulsion detection algorithms fairly.

4.2 Sparse Signal Decomposition

Measuring group delay showed promising results for tracing the dominate reflection from the upper and lower interfaces x_1 and x_3 in most M-scan data, however, weak, overlapping and attenuated interfaces pose a very difficult problem when utilizing cross-correlation as a means tracking interfaces. The problem of sparse signal decomposition has been dealt with extensively in ultrasound over the last two decades and a variety of methods exist for finding the sparse location of an ultrasound reflection, particularly when reflections are weak and overlapping. In many of these cases, high speed performance is seldom a concern and precision tends to dominate performance. For this reason, the method of model based signal decomposition was applied to the M-scan data, but simplified to ensure real-time performance was possible in the 2 ms window available for processing an A-scan during the acquisition of an M-scan. This section shows that accuracy is not lost for this specific application when reduced to a simplified problem.

4.2.1 Methods

Hayward and Lewis performed an early comparison on a number of deconvolution techniques [1], concluding that Wiener filters are best suited for on-line applications. Other studies have since been conducted on improving the resolution of Wiener filters by combining them L1-Norm deconvolution [2] and autoregressive spectral extrapolation [3] [4]. Such methods have actively been applied to the deconvolution of seismic waves [5], adhesive bonded joints [6] and various other NDE applications with reasonable complexity.

Problems arise in the presence of dispersive and attenuative material, where selective attenuation of certain frequencies results in distortion of reflected pulses. In such cases, more complex methods such higher order spectrum deconvolution and bispectrum analysis [7] and minimum entropy deconvolution with sparse [8] [9] and semi-sparse [10] solutions can be powerful tools at the expense of complexity, processing time and the ability to estimate certain attenuation parameters.

Matching Pursuit (MP) based methods [11] have also been used but focus primarily on feature extraction by best modeling the reflector given an excitation. Certain applications focus on pulse detection [12], which is the focus of this work.

Thus, a sparse deconvolution method based on simplifying current iterative search approaches [9] was implemented which exhibits a general robustness to minor pulse distortion, improved sparsity over Wiener filtering methods, an extremely low complexity/cost and fully parallel structure suitable for hardware implementation.

4.2.2 Estimates and Residuals

One of the simplest methods for pulse detection is by peak envelope detection. In poor signal to noise ratio (SNR) measurements, the envelope peak of overlapping pulses is difficult to distinguish from noise. In addition, the precise location of a pulse is difficult to determine in distorted pulses, where the envelope peak position is often shifted from the envelope peak of a reference pulse. A more reliable method is detection of the peak cross correlation between a measured signal and reference pulse.In this case, overlapping pulses become indistinguishable where only the dominate pulse in amplitude is detectable.

The approach taken in this work sequentially determines the impulse response of the specimen $h(t)$ though a "closest match" approach. In early iterative search methods, pulses were detected using maximum likelihood detectors [13] and recently improved for computational complexity by exploiting signal sparsity and pre-computing the response from scatters in [9]. Although these methods provide a very elegant solution to the deconvolution problem, particularly by modeling discrepancies in the reflector response as part of the signal noise, limitations in the real-time spot-welding environment make the computational simplifications either ill-suited or insufficient for meeting the timing requirements. Model-based estimation pursuit for sparse decomposition [14] presents a well suited approach except that estimating the pulse for every reflector can be slow and in some cases the proposed maximum a-priori (MAP) parameter estimation failed to model the reflection.

Thus, the search criteria for pulse locations was simplified to a sequential search for M maximum cross correlations on residues formed by subtracting the last detected pulse, using a single modeled pulse (similar to [14] only without estimation after partitioning.) This was tested against other real-time candidates in literature using data specific to the M-scans acquired using the Inline device, where the number of reflectors are know and a reference pulse exist for generating a suitable pulse model.

4.2.3 Modeling the Reflected Pulse

The reflected ultrasound pulses in the dispersive multi-layered workpiece were modeled using a Gaussian Chirplet (GC) as this model was used in similar applications in [15, 16]. The following model was used similar to [14]:

$$g[\boldsymbol{\theta}; n] = \beta e^{-\alpha(n-\tau)^2} \cos\left(2\pi f_c(n-\tau) + \psi(t_k-\tau)^2 + \phi\right) \tag{4.1}$$

where $\boldsymbol{\theta} = [\alpha\ \tau\ f_c\ \psi\ \phi\ \beta]$

At the start of the M-scan, before welding begins, a number of A-scans are averaged and segmented to perform pulse estimation. The estimated pulse is segmented using a fixed width window starting from the first zero crossing prior to the first A-scan envelope peak. This simple approach is possible because the front wall reflection is always the first reflection in an M-scan and minor overlap or distortion of the pulse due changes in the rough contacting boundary from weld to weld are ignored by the optimization approach.

The Maximum Likelihood Estimate (MLE) Gauss-Newton (GN) iteration approach [17] was taken to best estimate the pulse $x(n)$ by the following.

For iteration k:

1. Guess $\boldsymbol{\theta}(0)$, set $k = 0$.
2. Compute the gradients $\mathbf{H}(\boldsymbol{\theta}(k))$
3. Compute $s(\boldsymbol{\theta}(k))$
4. Solve $\boldsymbol{\theta}(k+1) = \boldsymbol{\theta}(k) + (\mathbf{H}^T(\boldsymbol{\theta}(k))\mathbf{H}(\boldsymbol{\theta}(k)))^1\mathbf{H}^T(\boldsymbol{\theta}(k))(x - s(\boldsymbol{\theta}(k)))$.
5. Check for convergence
   If $\boldsymbol{\theta}(k+1) \quad \boldsymbol{\theta}(k) <$ tolerance, stop.
6. Set $k = k + 1$ and repeat from 2).

4.2.4 Forming Residuals

First, the true measured signal $y[n]$ must be re-expressed in terms of the modeled reflections uniquely characterized by $g[\boldsymbol{\theta}]$ from x_1 such that:

$$y[n] = \sum_{i}^{M} g[\boldsymbol{\theta}_i] + e[n] \tag{4.2}$$

where M is the number of reflectors and $\boldsymbol{\theta}_i$ determines the modeled pulse properties including scale $\beta = a_i$ and position $\tau = n_i$.

The dominate pulse in this representation can be found by the cross-correlation $< y, g[\boldsymbol{\theta}] > [n]$, which will have a maximum at $n = n_i$. In this case, model parameter τ takes on the value n_i. Once the dominate pulse location is determined, a new pulse estimate must be performed at that location to solve $\boldsymbol{\theta}_i$. For fast performance, only the amplitude parameter β is considered and is determined by the envelope magnitude at pulse location n_i. A residual signal $R^i y[n]$ is then formed by subtracting the scaled pulse from the current residual:

$$R^{i+1}y[n] = R^i y[n] - g(\boldsymbol{\theta}_i) \tag{4.3}$$

where $R^0 y[n] = y[n]$ and $g(\boldsymbol{\theta}_i)$ is a scaled version of the modeled pulse $g(\boldsymbol{\theta})$. If greater precision for pulse estimation is required, optimization of additional model parameters f_c and ϕ via MAP or MLE done in the initial modeling of the pulse can be added to the scaling β, but at the expense of computation time. For a perfect estimation, the residual signal no longer correlates with the reference pulse at n_i, however, for weak estimations based on only the scaling parameter, the residual can contain remnants of a weakly correlated signal. This is often the case in this simplification, however, the next detected pulse location is the subsequent maximum cross correlation and so the weakly correlated residual is generally insignificant. Since decomposition stops after M reflections are found, weakly correlated positions are ignored.

The number of iterations for real-time weld evaluation is fixed by the number of expected reflections, but stopping criteria can also be based on a convergence criteria, for instance, with error defined as:

$$error = \sqrt{\frac{1}{N}\sum_{n=0}^{N}\left(R^{i+1}y[n] - R^{i}y[n]\right)^2} \tag{4.4}$$

4.2.5 Biased Position Tracking

Due to the predictable nature of the thermal process responsible for generating and changing the acoustic reflectors of the system, the cross correlation approach can be improved by biasing the correlation at a prior estimated position for a reflection. This has the benefit of reducing false detections for a semi-stationary reflector. The imposed biased can be implemented as a simple window in the estimated region of time where a pulse reflection is likely to exist. The window width can be sized based on a known maximum displacement between ultrasound A-scans governed, in this case, by the nature of the thermal process.

4.2.6 Real-time Hardware Considerations

For real-time hardware processing, the constraints of an algorithms are principally governed by the ability to perform parallel computations and minimize sequential operations. Performance is also gained and cost reduced by avoiding complex operations and significant data storage. The proposed implementation is only one of many, have the general focus is on emphasizing the suitability of the proposed pulse detection algorithm for critical timing applications.

First, consider the measured data as a vector $\mathbf{y} = [y_1 ... y_N]'$ resulting from a system of M reflectors $\mathbf{h} = [h_1 ... h_M]'$ with finite length pulse $\mathbf{x} = [x_1 ... x_P]'$, where $\mathbf{x} = g[\boldsymbol{\theta}]$. This work now proposes an iterative hardware based method for estimating $\mathbf{h}$ that can be divided into the following steps:

Step 1: For the first iteration, it is necessary to determine the amplitude envelope $A = [A_1 ... A_N]'$ of $\mathbf{y}$. The most effective real-time approach is to low-pass filter the absolute value of the incoming signal. The amplitude envelope is later used to scale the estimated pulse when forming the next residual iteration. When a dominate pulse is identified and a new residual formed, only the envelope on the window of identified pulse must be recomputed eliminating the need to recompute a new envelope for the entire residual.

Step 2: The cross correlation vector $\mathbf{c}$ between the current residual and estimated pulse must be calculated to determine the position of the maximum n_i. A number of fast algorithms have been proposed for time domain cross correlation [18], however, are slower than transform domain approaches at moderate sizes [19]. For optimized speed and to exploit efficiency of modern DSPs, cross correlation can be computed as a convolution with a time reversed feature, in this case:

$$\begin{aligned} c[n] \quad =< y, x > [n] \quad &= \sum_{i=1}^{P} y[n]x[n-i] && (4.5) \\ &= F^{-1}\left\{F\left\{\mathbf{y}\right\}F^{*}\left\{\mathbf{x}\right\}\right\} && (4.6) \end{aligned}$$

It should be noted that the time domain approach of 4.5 can be implemented in parallel with *Step 1*, while the transform domain approach of 4.6 requires fewer resources. Since cross correlation of relatively short signals was required and the current application of the fast tracking algorithm required speed optimization, a time domain cross correlation was performed in parallel with the amplitude envelope calculation of *Step 1.* Additionally, the maximum of the cross correlation must be determined for each residual. With the time domain approach, the maximum can be found while computing the cross correlation by comparing the actively calculated value to a previous maximum, where as for the transform domain cross correlation, the maximum must be found as part of a separate process.

Step 3: Once the position of a dominate pulse n_i is determined, the i'th residual signal is calculated according to 4.3. First, the estimated pulse $\mathbf{x}$ is scaled by the amplitude envelope value at n_i and then subtracted from $\mathbf{y}$ such that:

$$r^{i+1}[n] = \begin{cases} r^{i}[n] - A[n_i]x[n-n_i] & n_i < n \leq n_i + P \\ r^{i}[n] & otherwise \end{cases} \qquad (4.7)$$

The simplifed complexity of the residual method is clear as only P multiplications and additions are required for calculating the residual of signal length N, where pulse length P is much smaller.

Step 4: The process is repeated from *Step 1* on the new residual until a specified stopping criteria is satisfied. In the most simple case, the process is repeated for the number of desired pulses to be identified, however, in very poor SNR scans, or when the estimated pulse does not sufficiently remove dominate pulses from the residual, a greater number of iterations may need to be performed to better estimate the location of all desired reflection.

4.2.7 Simulation Results

The performance of the simplified method (called Fast Tracking in the sections to follow) was evaluated for three scenarios: a) several overlapping echoes, b) noisy signals, c) echoes exhibiting frequency attenuation. The results were compared with methods producing semi-sparse to sparse results including: Wiener filtering, Frequency Extrapolation [4] and Minimum Entropy Deconvolution [9]. These methods were selected because of their low computational complexity and real-time suitability, where other algorithms such as Expectation Maximization require specific initial conditions and significant iterations for solving the system.

4.2.7.1 Overlapping Echoes

A test sample with closely overlapping echoes was first considered, since most sparse deconvolution approaches are very successful at estimating the correct phase and amplitude of these pulses where cross correlation alone fails. Constructive and destructive interference of Gaussian pulse echoes were considered for center frequency pulses of 10 MHz and 80% bandwidth. Fig. 4.3a shows the simulated signal and the results of each method, where the stopping criteria for the proposed algorithm was set to $M = 5$.

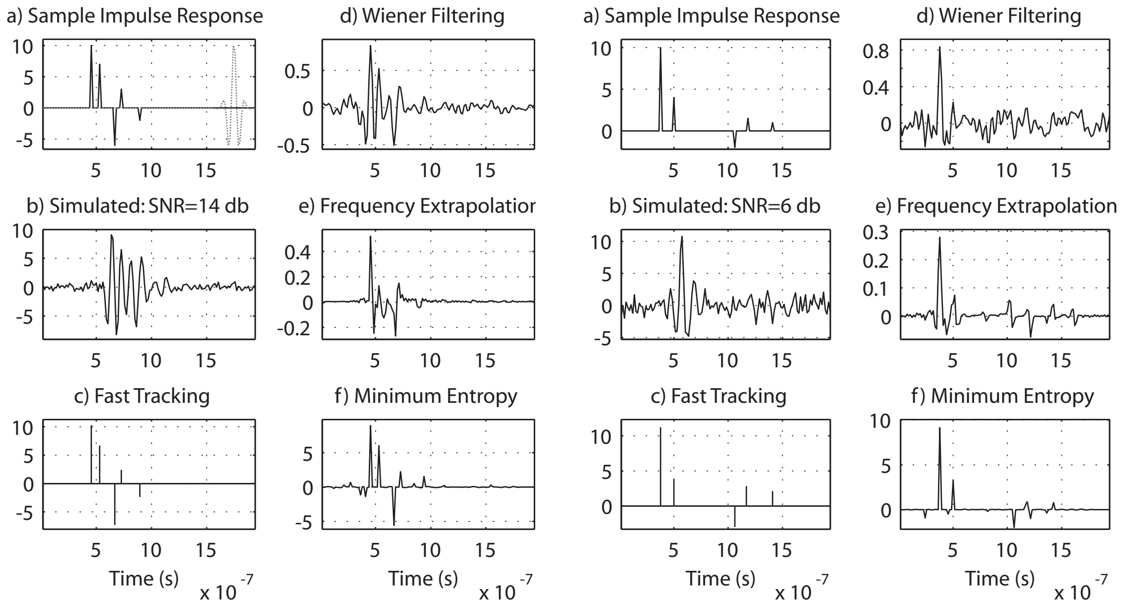

(a) (b)

Figure 4.3: a) Sample impulse response and Gaussian pulse. b) Convolved signal with additive white Gaussian noise. c) Result of fast tracking with M=5, d) Weiner filtering, e) Frequency Extrapolation on Wiener filtered signal with auto regressive order=20, f) Minimum Entropy deconvolution with 8 iterations and $\sigma_r = 0.1298$ and $\sigma_r = 0.1568$..

4.2.7.2 Low SNR Signals

Another, more critical, aspect to examine is the performance in noisy measurements. Fig. 4.3b shows a simulated scan corrupted with significant noise (SNR=6db) and the results processed with the same algorithms shown in Fig., 4.3a. Even when the signal amplitude is near the noise amplitude, the fast tracking algorithm can still resolve the pulse locations, amplitude and phase.

4.2.7.3 Frequency Attenuation

for a final comparison, the reflector sequence of Fig. 4.3b was modified using the discrete-time attenuation model found in [8], where the attenuation impulse response assumes the simple form:

$$p(n) = \begin{cases} 0 & n = 0 \\ 1 - a & n = 1 \\ a & n = 2 \\ 0 & otherwise \end{cases} \tag{4.8}$$

where $0 < a << 1$. A reflection at depth $n = l$ then has the cumulative attenuation impulse response $p_l(n) = p(n) * ... * p(n)$, or l convolution of equation 4.8. The reflector sequence is then expressed as:

$$\mathbf{h} = \mathbf{Pr} \tag{4.9}$$

where for reflector sequence $\mathbf{r}$ of length N, $\mathbf{P}$ is $N \times N$ with $A_n, l = p_l(n)$ and $\mathbf{h}$ is the new attenuated system impulse response of the system.

Fig. 4.4 shows the results for a modified system impulse with $a = 0.01$. The primary drawback of the fast tracking method becomes evident since the first attenuated pulse is resolved as two unattenuated reflectors. In this case, the number of iterations for fast tracking was increased to allow for detection of true pulses below the maximum cross correlation of false detections.

Of the methods compared in Fig. 4.4, only Maximum Entropy Deconvolution inherently accounts for prorogation in an attenuative media and hence performs well when the exact attenuation parameter a used to generate the signal is also used to process the signal. In practice, determining a for a real system is more involved and not suitable for the dynamic welding environment where attenuation not only changes from weld to weld, but during the welding process as well.

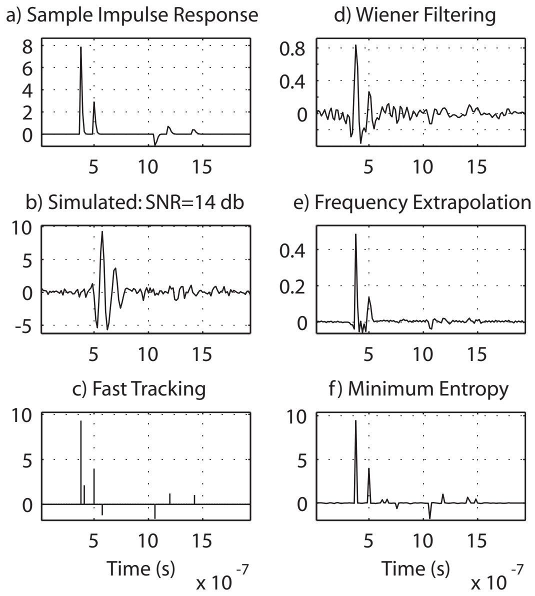

Figure 4.4: a) Sample impulse response with attenuation model a=0.01. b) Convolved signal with additive white Gaussian noise. c) Result of fast tracking with M=7, d) Weiner filtering, e) Frequency Extrapolation on Wiener filtered signal with auto regressive order=20, f) Minimum Entropy deconvolution with 8 iterations and $\sigma_r = 0.1253$ and attenuation factor a=0.01.

4.2.8 Real Welding Results

M-scans of the resistance welding process were taken for a series of resistance spot welds using 0.7 mm thick high strength steel plates, using a 10 MHz single element transducer with a sampling frequency of 66 MHz and a pulse repetition rate of 400 Hz or equivalently 2.5 ms between A-scans. Copper electrodes with a contact face diameter of 5.7 mm were used and welding current was varied from 5 kA to 11 kA in order to control the heating rate and resulting nugget size. M-scans for an undersized weld, good weld and expulsion event were processed using Fast Tracking, Frequency Extrapolation and Minimum Entropy Deconvolution to detect the interfaces outlined in Fig. 2.5. A-scans were truncated to 128 samples and up sampled 2 times to improve the time resolution of the pulse locations, since a 1 sample shift at 66 MHz sampling could mean a error of up to 100 K in temperature calculations. In the future, faster data acquisition will permit faster sampling without the need to up sample a-scan measurements.

Fig. 4.5 shows an example of a processed M-scan using Fast tracking, Minimum Entropy Deconvolution and Frequency Extrapolation. It is cleat that the fast tracking approach is still able to detect the major reflectors x_1, x_2 and x_3 and even resolve the location of the weak reflectors x_4 and x_5 with minimal noise. Minimum Entropy Deconvolution, at it's best, detected multiple relfections at a given reflector position and had difficulty resolving x_5 while Frequency Extrapolation, although successfully highlighted all major and minor reflections, was unable to resolve the location to a finite point.

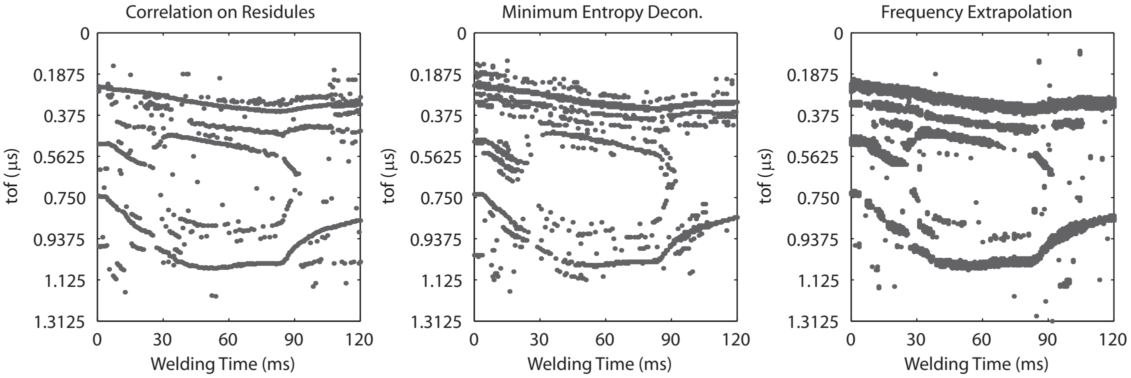

(a) (b) (c)

Figure 4.5: a) using cross correlation on residules with N=5 and predictive biasing for the phase of the lower nugget reflection, b) using minimum entropy deconvolution [8] with 8 iterations, $S_0 = 0.008$, $\sigma_{noise} = 0.4$ and no attenuation, c) using frequency extrapolation [3] with $Q = 0.1$, $dB1 = 3$, $dB2 = 15$ and an auto regressive order of 40.

4.2.9 Performance and Implementation

The current implementation of sparse signal decomposition was implemented in MATLAB and is capable of identifying four reflectors in a 128 sample A-scan in 1.5 ms. This permits 500 μ s for tracing the interfaces for their final position, which in the next Section, is shown to be more than sufficient. Optimized C++ implementation was not considered at this point in time as timing constraints have been met. Final implementation is far better suited for an FPGA so that real-time feedback in hardware can be considered in the future.

4.3 An Efficient Hough Transform Variant

Tracing segments of curves in M-Scan images is critical to real-time analysis of the image. Real-time, in this instance, refers to the processing of data during it's acquisition with minimal latency (defined in this case as the number of A-scans required to produce an output.) In the previous section, it was shown how noisy, non-linear ultrasound reflections were detected and reduced to a sparse representation of the reflector sequence. This spares data held the binary locations of detected pulses at specific TOF indices and can be presented as a binary image. Of course, the presence of false detections and missed detections adds gaps and noise along the interfaces in this image. These broken, noisy interfaces must still be traced to determine the precise TOF from the reflectors as they change over time. To be useful for real-time prediction and detection of expulsions, these interfaces must be tracked as data is acquired (2-3 ms delay between A-scans), thus a very fast method must be employed.

When divided into small segments, a curve can be approximated as a series of straight lines. The slope of these straight lines is useful for predicting the location of the next partial line segment along the curve. Although a number of methods exist for detecting straight line segments in an image, the Hough transform [20] is one of the most widely used and is especially useful for discriminating 'meaningful' segments, even in the presence of stray points and noisy pixels. The main drawback of the Hough transform is that it can be very time consuming to compute, especially for large images.

The Hough transform exploits the point-line duality by mapping (x, y) points of an image to a 2D parameter space using (ρ, θ) parameterization. For each pixel of an image the normal equation of a line is computed for a range of theta values by:

$$\rho = xcos(\theta) + ysin(\theta) \tag{4.10}$$

where ρ is the distance from the origin perpendicular to the line passing through (x, y) at angle θ. To represent all possible lines uniquely, Hough space can be restricted to:

$$\theta \in [0, \pi) \tag{4.11}$$

$$\rho \in [-R, R], R = \sqrt{w^2 + h^2} \tag{4.12}$$

where w and h are the width and height of the image respectively.

In Hough space, ρ and θ are quantized such that $H(\rho, \theta)$ acts as a set of accumulator bins for:

$$\rho = n\Delta\rho, \quad n \in \mathbb{I} \tag{4.13}$$

$$\theta = n\Delta\theta, \quad n \in \mathbb{I} \tag{4.14}$$

In this way, every active pixel $I(x, y)$ in a binary image maps to a series of $H(\rho, \theta)$ bins, adding 1 to each Hough space index that satisfies (4.10). The next stage of the Hough transform involves searching the 2D hough space for peaks in $H(\rho, \theta)$. A peak is essentially a (ρ, θ) pair that was common to the most number of pixels on the image. In order to obtain any further information regarding the number of line segments or the length of the lines that may have contributed to a peak in Hough space, the image must be traced pixel by pixel along the (ρ, θ) line in the image space. This can also be a slow operation, especially for large images with a great number of lines.

The main drawback of the standard Hough transform for line finding is that for certain quantization levels $\Delta\rho$ and $\Delta\theta$, approximately collinear points may not intersect at the appropriate $H(\rho, \theta)$ accumulator bins. Optimal quantization of ρ and θ have been reported on in [21]. In addition, there has been a great number of implementation and architectures for the Hough transform proposed in literature to both reduce the computational intensity and improve upon the brute force voting scheme described above. Many of these methods are designed for medium sized images with maximum images sizes of 512×512 pixels. Very few methods are suitable for larger images. The fastest of these algorithms rely on heavy parallelization in ASIC designs and CPU based methods lack comparable performance [22, 23, 24].

At very low resolution images, the complexity of the transform is dominated by the density of the 2D Hough space required to detect lines accurately. Since such a small number of pixels are used, the chances of collinear lines intersecting at the same (ρ, θ) index decreases substantially. Thus, motivation for a new Hough transform approach comes from the need to determine straight lines in very low resolution, noisy images for a small number of lines (mostly for the dominate line). To the best of this authors knowledge, little work has been done for optimizing the Hough transform for image sizes on the order of 5×5 to 15×15 pixels, and the method proposed in this section could not be found in literature of recent papers [25, 26].

The main premise behind the Hough transform technique used in this work is that finding the maximums in the the 2D $H(\rho, \theta)$ accumulator space is reduced to finding the minimum difference in ρ values between pixels in a $\rho(I,\theta)$ space, where I is an active pixel in the image. The complexity is immediately reduced from: $N_f \times N_\rho \times N_\theta$ to $N_f \times N_\theta$, where N_f is the number of feature pixels (active pixels in the binary image).

Unlike the accumulator space of the standard Hough transform that consist of an $N_\rho \times N_\theta$ array of integers, the new Hough space consist of $N_f \times N_\theta$ values of ρ. The typical value of N_f is generally accepted as $N_f = 0.1wh$ [26] and so for small images is always quite low compared to the optimal value of $\Delta\rho$. The minimum difference between ρ values for pairs of pixels is used to determine intersecting curves on the standard $H(\rho,\theta)$ space instead of peaks in the accumulator bins. This has a number of added advantages as will be discussed.

4.3.1 The Method

Fig. 4.6 shows the complete Efficient Hough transform Variant algorithm that was implemented in this work.

The fist step in the proposed method is to remove singular pixels from the image. This optional step reduces clutter in the final Hough space and reduces the number of feature pixels, but does not have an effect on the detection of dominate lines.

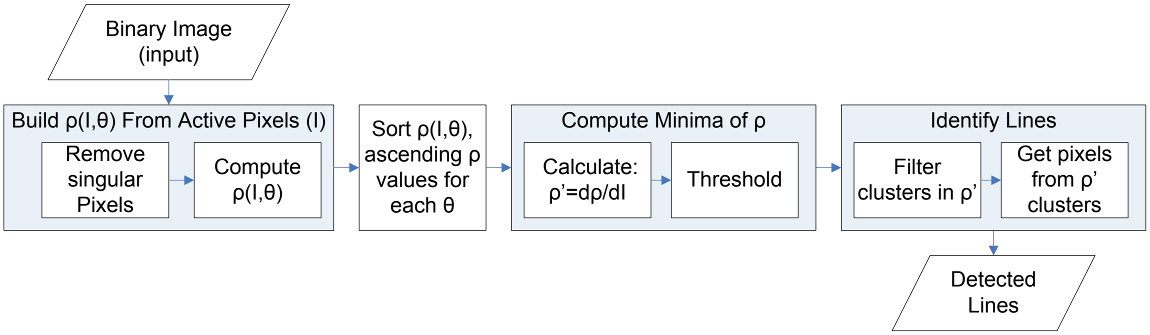

Figure 4.6: Flow diagram for the Hough transform Variant.

For discrete variable representation, let I represent the binary image as a $H \times W$ matrix. A single pixel $I_k = [x_k \; y_k]$ has co-ordinates defined by:

$$\begin{aligned} x_k &= \lfloor k/H \rfloor \\ y_k &= k - Hx_k \end{aligned} \tag{4.15}$$

Let the active pixels of I be represented as a list of indexes A such that A_i denotes the i^{th} active pixel with coordinates determined by I_{A_i}. Since we focus only on active pixels, let us consider a mapping $I(A_i) \rightarrow [x_i \; y_i]$ such that $k = A_i$ in (4.15).

Given N active pixels in I, the corresponding co-ordinate matrix is:

$$P_i = I(A_i) = [x_i \; y_i], \quad i < N, i \in \mathbb{N} \tag{4.16}$$

and the following parameter transform from (4.10) for M values of θ:

$$T_j = \begin{bmatrix} cos(\theta_j) \\ sin(\theta_j) \end{bmatrix}, \quad j < M, j \in \mathbb{N} \tag{4.17}$$

the new Hough parameter space $\boldsymbol{\rho}$ (an $N \times M$ matrix) can be formed by apply T to each active pixel coordinate in P by:

$$\boldsymbol{\rho}_{ij} = P_i T_j = \begin{bmatrix} P_0T_0 & P_0T_1 & \cdots & P_0T_M \\ P_1T_0 & P_1T_1 & & \vdots \\ \vdots & & \ddots & \vdots \\ P_NT_0 & P_NT_1 & \cdots & P_NT_M \end{bmatrix} \tag{4.18}$$

The columns of $\boldsymbol{\rho}$ are the same as the quantized θ of the standard Hough space while the rows of $\boldsymbol{\rho}$ hold the non-quantized ρ value of each active pixel.

Fig. 4.7a shows the $\boldsymbol{\rho}$ space after applying the above procedure to a 15 x 15 binary image with a 135 degree diagonal from corner to corner. In order to easily obtain the minimum difference between pairs of pixels, the rows of $\boldsymbol{\rho}$ are sorted in ascending order for each θ column to form $\boldsymbol{\rho}^S$. In this way, the pixels with the closest ρ values along a given column will be neighbored and their difference when taken across rows may produce a minimum for each θ column.

The un-sorted $\boldsymbol{\rho}$ space of Fig. 4.7a is shown after sorting in Fig. 4.7b. It is also shown in Fig. 4.7b that the corresponding active pixel index is preserved in $\boldsymbol{\rho}^S$ as this index is the map back to the active pixels location in I. Line detection in $\boldsymbol{\rho}^S$ involves identifying the regions (groups of pixels) with the closest ρ value. To evaluate this, the difference is taken down a column of $\boldsymbol{\rho}^S$ such that:

$$\boldsymbol{\rho}'^S_{k,j} = \boldsymbol{\rho}^S_{k+1,j} - \boldsymbol{\rho}^S_{k,j}, \quad k < N-1, k \in \mathbb{N} \tag{4.19}$$

A threshold is then applied to $\boldsymbol{\rho}'^S$ so that neighboring pixels that are ‘close enough’ are considered to have the same ρ value. This produces a binary mask of pixel pairs that make up lines in the image. A series of pixel pairs in this mask make up a line segment and so the number of lines, and the number of pixels that make up a line, can be immediately identified by counting the number of continuous regions (or clusters) on this mask and the number of pixel pairs in each cluster.

To eliminate lines with too few pixel pairs, a filter is applied to the binary mask of $\boldsymbol{\rho}'^S$ so that only clusters of at least N pixels pairs are retained. The final stage is to extract the pixel indexes from each cluster and retain the minimum and maximum pixel index to use as the end points of a line in the image.

Fig. 4.9 shows another example where two lines at different angles (0 and 135 degrees) are present.

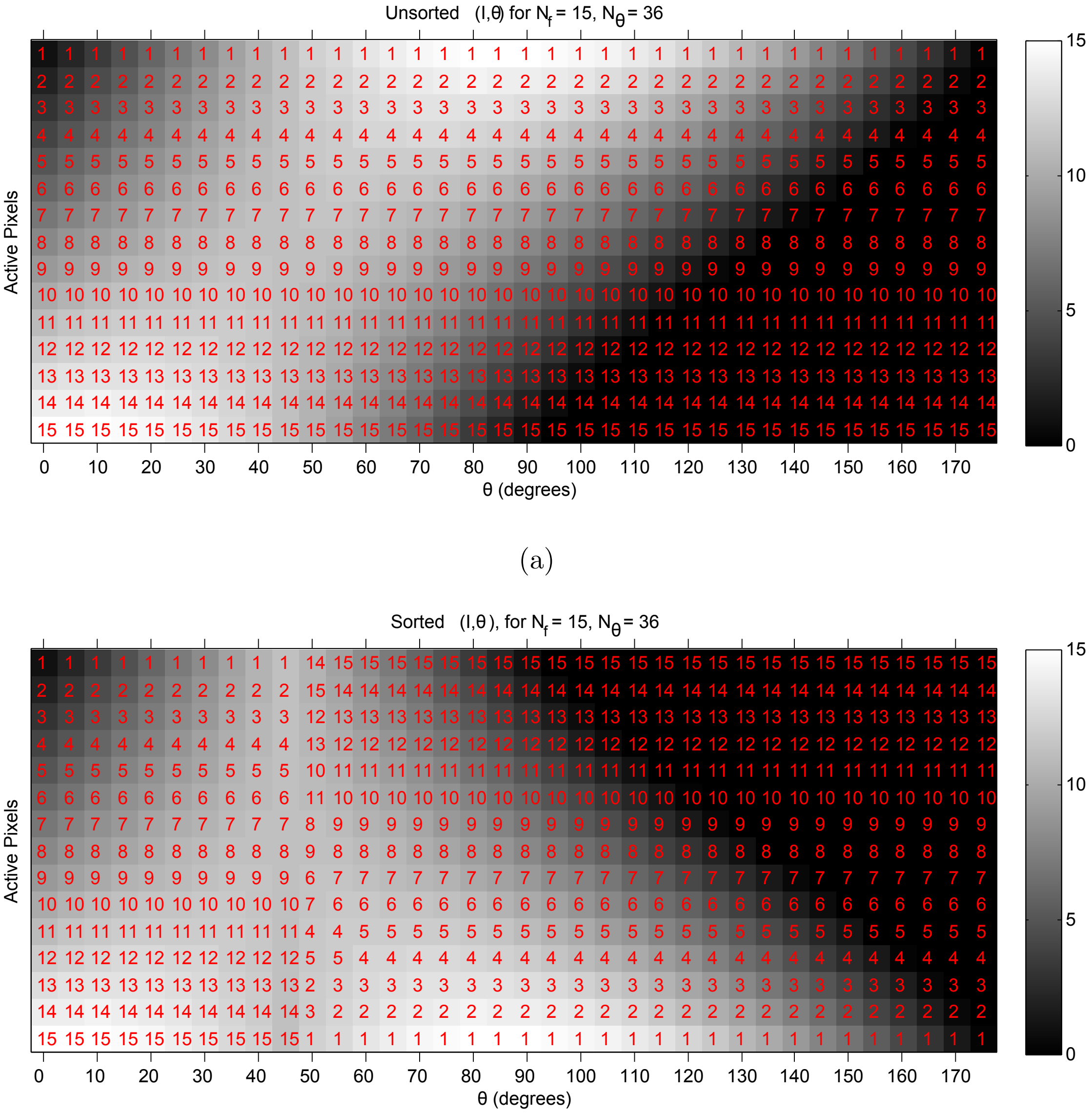

1	1	1	1	1	1	1	1	1	1	1	1	1	1	1	1	1	1	1	1	1	1	1	1	1	1	1	1	1	1	1	1	1	1	1	1
2	2	2	2	2	2	2	2	2	2	2	2	2	2	2	2	2	2	2	2	2	2	2	2	2	2	2	2	2	2	2	2	2	2	2	2
3	3	3	3	3	3	3	3	3	3	3	3	3	3	3	3	3	3	3	3	3	3	3	3	3	3	3	3	3	3	3	3	3	3	3	3
4	4	4	4	4	4	4	4	4	4	4	4	4	4	4	4	4	4	4	4	4	4	4	4	4	4	4	4	4	4	4	4	4	4	4	4
5	5	5	5	5	5	5	5	5	5	5	5	5	5	5	5	5	5	5	5	5	5	5	5	5	5	5	5	5	5	5	5	5	5	5	5
6	6	6	6	6	6	6	6	6	6	6	6	6	6	6	6	6	6	6	6	6	6	6	6	6	6	6	6	6	6	6	6	6	6	6	6
7	7	7	7	7	7	7	7	7	7	7	7	7	7	7	7	7	7	7	7	7	7	7	7	7	7	7	7	7	7	7	7	7	7	7	7
8	8	8	8	8	8	8	8	8	8	8	8	8	8	8	8	8	8	8	8	8	8	8	8	8	8	8	8	8	8	8	8	8	8	8	8
9	9	9	9	9	9	9	9	9	9	9	9	9	9	9	9	9	9	9	9	9	9	9	9	9	9	9	9	9	9	9	9	9	9	9	9
10	10	10	10	10	10	10	10	10	10	10	10	10	10	10	10	10	10	10	10	10	10	10	10	10	10	10	10	10	10	10	10	10	10	10	10
11	11	11	11	11	11	11	11	11	11	11	11	11	11	11	11	11	11	11	11	11	11	11	11	11	11	11	11	11	11	11	11	11	11	11	11
12	12	12	12	12	12	12	12	12	12	12	12	12	12	12	12	12	12	12	12	12	12	12	12	12	12	12	12	12	12	12	12	12	12	12	12
13	13	13	13	13	13	13	13	13	13	13	13	13	13	13	13	13	13	13	13	13	13	13	13	13	13	13	13	13	13	13	13	13	13	13	13
14	14	14	14	14	14	14	14	14	14	14	14	14	14	14	14	14	14	14	14	14	14	14	14	14	14	14	14	14	14	14	14	14	14	14	14
15	15	15	15	15	15	15	15	15	15	15	15	15	15	15	15	15	15	15	15	15	15	15	15	15	15	15	15	15	15	15	15	15	15	15	15

(a)

1	1	1	1	1	1	1	1	1	1	14	15	15	15	15	15	15	15	15	15	15	15	15	15	15	15	15	15	15	15	15	15	15	15	15	15
2	2	2	2	2	2	2	2	2	2	15	14	14	14	14	14	14	14	14	14	14	14	14	14	14	14	14	14	14	14	14	14	14	14	14	14
3	3	3	3	3	3	3	3	3	3	12	13	13	13	13	13	13	13	13	13	13	13	13	13	13	13	13	13	13	13	13	13	13	13	13	13
4	4	4	4	4	4	4	4	4	4	13	12	12	12	12	12	12	12	12	12	12	12	12	12	12	12	12	12	12	12	12	12	12	12	12	12
5	5	5	5	5	5	5	5	5	5	10	11	11	11	11	11	11	11	11	11	11	11	11	11	11	11	11	11	11	11	11	11	11	11	11	11
6	6	6	6	6	6	6	6	6	6	11	10	10	10	10	10	10	10	10	10	10	10	10	10	10	10	10	10	10	10	10	10	10	10	10	10
7	7	7	7	7	7	7	7	7	7	8	9	9	9	9	9	9	9	9	9	9	9	9	9	9	9	9	9	9	9	9	9	9	9	9	9
8	8	8	8	8	8	8	8	8	8	9	8	8	8	8	8	8	8	8	8	8	8	8	8	8	8	8	8	8	8	8	8	8	8	8	8
9	9	9	9	9	9	9	9	9	9	6	7	7	7	7	7	7	7	7	7	7	7	7	7	7	7	7	7	7	7	7	7	7	7	7	7
10	10	10	10	10	10	10	10	10	10	7	6	6	6	6	6	6	6	6	6	6	6	6	6	6	6	6	6	6	6	6	6	6	6	6	6
11	11	11	11	11	11	11	11	11	11	4	4	5	5	5	5	5	5	5	5	5	5	5	5	5	5	5	5	5	5	5	5	5	5	5	5
12	12	12	12	12	12	12	12	12	12	5	5	4	4	4	4	4	4	4	4	4	4	4	4	4	4	4	4	4	4	4	4	4	4	4	4
13	13	13	13	13	13	13	13	13	13	2	3	3	3	3	3	3	3	3	3	3	3	3	3	3	3	3	3	3	3	3	3	3	3	3	3
14	14	14	14	14	14	14	14	14	14	3	2	2	2	2	2	2	2	2	2	2	2	2	2	2	2	2	2	2	2	2	2	2	2	2	2
15	15	15	15	15	15	15	15	15	15	1	1	1	1	1	1	1	1	1	1	1	1	1	1	1	1	1	1	1	1	1	1	1	1	1	1

(b)

Figure 4.7: a) Unsorted and b) sorted $\rho(I, \theta)$ space with active pixel indexes shown in red.

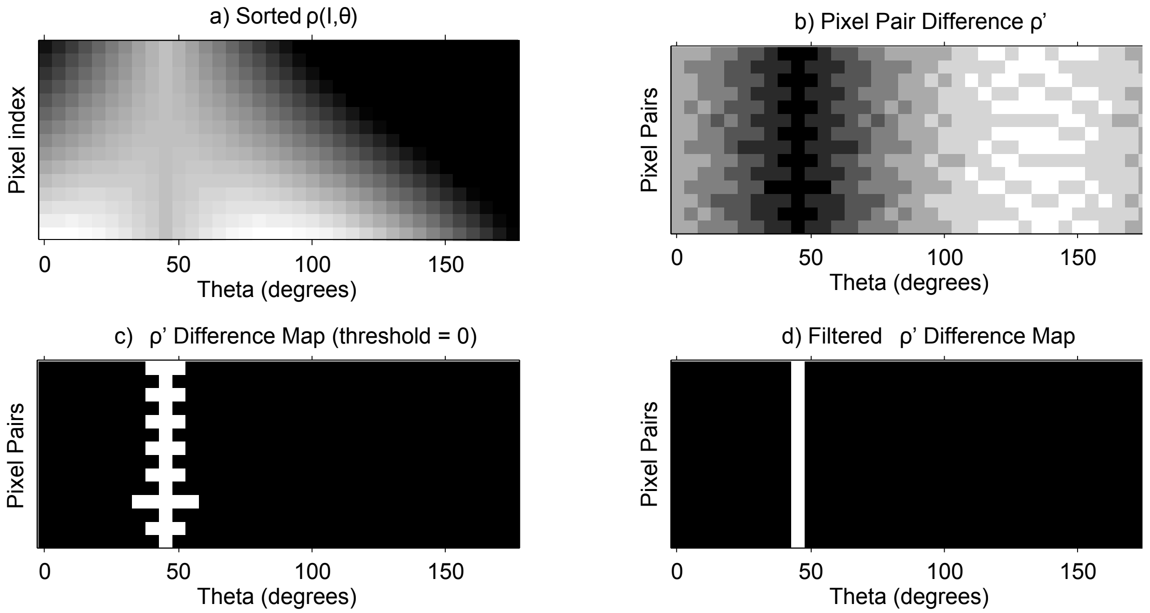

Figure 4.8: Hough transform Variant showing: a) Sorted ρ space, b) difference of neighboring pixels in sorted ρ space, c) mask of pixel pairs with a difference $\leq$ threshold, d) filtered pixel difference map eliminating lines made up of only 2 pixels.

4.3.2 Optimization of the Hough Transform Variant

Reducing the parameter space as well as eliminating the need to detect pixels on a line by back tracing through the image already improved the speed of the Hough transform to exceed the standard implementation in PCs as reported in [26] and compared to the compiled MATLAB functions. The final performance is presented in the following section. Still, the arduous task of sorting the active pixel list poses a significant bottle neck in this method. Thus, further optimization was performed to further accelerate the Hough Transform. The main optimization comes from a suitable trade-off of memory for computational efficiency. In the optimized method, the $\rho(I, \theta)$ space is pre-computed for every possible active pixel for the desired image size. For small images, this is not a significant trade-off, however, the memory demands do increase significantly with increased image size.

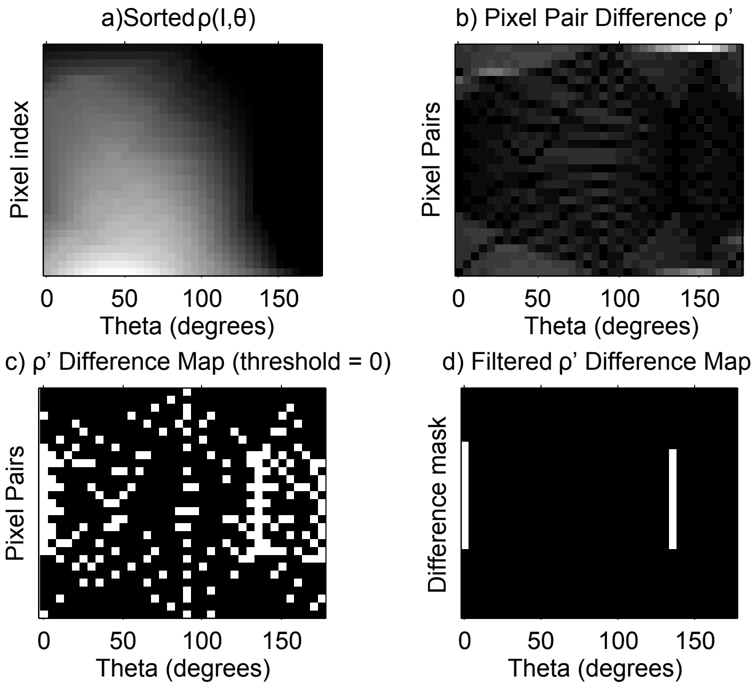

Figure 4.9: Real-time Hough showing: a) Sorted ρ space, b) difference of neighboring pixels in sorted ρ space, c) mask of pixel pairs with a difference $\leq$ threshold, d) filtered pixel difference map eliminating lines made up of only 2 pixels.

The comprehensive, pre-computed ρ space was then pre-sorted and a pixel map $I \rightarrow I'$ was created so that the appropriate ρ values could still be extracted for active pixels while retaining the order of the ρ values for each θ. This improves the performance of the proposed method significantly since the computation and sorting problem is replaced with a memory access problem of substantially lower complexity.

Once ρ space is calculated and sorted with a corresponding I' map, there is never a need to re-calculate this and the same space can be used for multiple images at different times. Fig. 4.10 shows the proposed optimized method.

A second optimization was made by reducing the storage size of the comprehensive pre-computed ρ space. Instead of storing floating point values of ρ, quantized values of ρ were used instead. In this way, the large ρ space required fewer bits to represent

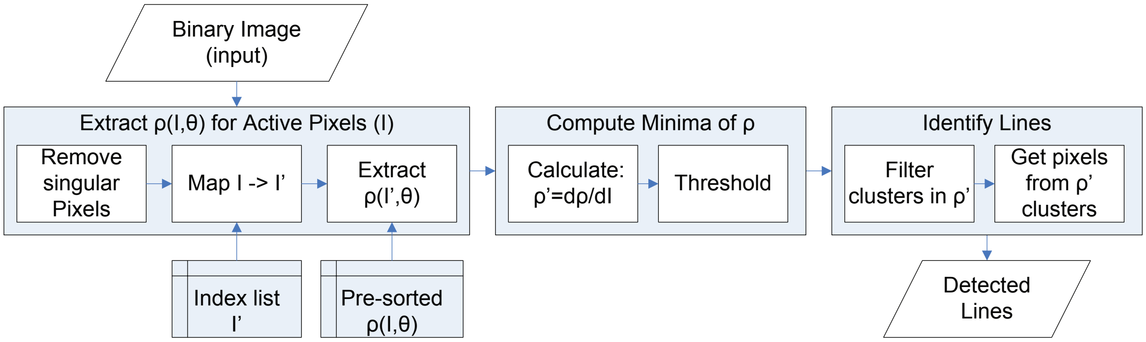

Figure 4.10: Flow diagram for the Optimized Hough transform Variant.

the values. In fact, using 8-bit positive integers permits 256 quantized values of ρ which far exceeds the minimum required quantization levels as reported in [27]. This additionally reduced the complexity of calculating ρ' as the difference is now performed on small integers instead of floating point values.

4.3.3 Filtering and Finding Clusters

After the optimizations of Fig. 4.10, the next bottleneck falls on filtering and finding clusters in $\boldsymbol{\rho}'^S$. This is actually quite a simple operation because of the nature of the $\boldsymbol{\rho}'^S$ space. In $\boldsymbol{\rho}'^S$, a near zero value results when two pixels have a similar ρ value after being sorted. The next closest pixel will have a 'zero' difference if it also has a similar ρ value, and so a series of n 'zeros' for a given θ value in $\boldsymbol{\rho}'^S$ space represents a line with $n+1$ pixels that share a similar (ρ, θ) representation in parameter space. This would be similar to an accumulation of $n+1$ points in the standard Hough transform at $H(\rho, \theta)$. The idea of a series of zeros representing the number of pixels on a line can be exploited to filter out 'lines' that are not considered significant, or in simpler terms, 'lines' that are not made up of enough pixels.

The filtering process is simply retaining pixels in the difference map that are apart of a group of n or more zeros. This was done with a series of linear convolutions according to Algorithm 1.

Algorithm 1 Filtering $\boldsymbol{\rho}'^S$ space.

```
$P_n \leftarrow n \times 1$ unit matrix
for each column vector $\theta$ in $\boldsymbol{\rho}'^S$ do
    $\theta \leftarrow \theta \otimes P_n$ , counts number of pixels in $n \times 1$ window
    $\theta \leftarrow \theta \geq n$ , thresholds pixels with counts of n or greater
    $\theta \leftarrow \theta \otimes P_n$ , restores the window of 1's around pixels above
end for
```

The result of Algorithm 1 is shown in Fig. 4.8 for $n = 2$ and in Fig. 4.9 for $n = 3$.

Once $\boldsymbol{\rho}'^S$ is filtered, finding lines is a matter of finding the largest groups of pixels. This can be accomplished any number of ways, but in this work, the focus was finding the dominate line and so the following method was applied to distinguish the most meaningful line.

First, $\boldsymbol{\rho}''^S = d\boldsymbol{\rho}'^S/dI$ was computed, where the sum of each column of $\boldsymbol{\rho}''^S$ indicates the number of lines found for a given θ value. The θ value with the most meaningful lines was determined by:

$$\theta_{max} = \max_{\theta} \left(\sum_{dI} \boldsymbol{\rho}'^S(dI, \theta) - \sum_{d^2I} \boldsymbol{\rho}''^S(d^2I, \theta) \right) \tag{4.20}$$

from which the corresponding ρ value is taken as the mean ρ value of each pixel in the dominate line by:

$$\rho_{max} = \sum_{i \in dI} \boldsymbol{\rho}^S \left(i, \theta_{max}\right) / \sum_{i \in dI} \boldsymbol{\rho}''^S \left(i, \theta_{max}\right) \tag{4.21}$$

4.3.4 Performance and Implementation

The optimized Hough transform Variant was implemented in both MATLAB and C++ to ensure that performance was gained over compiled MATLAB execution of the Hough transform and methods reported in [26]. Table 4.1 shows the timing results for computing the Hough transform on various size windows, including the retrieval of the finite line segment.

			Proposed	
Window Size	θ step	MATLAB	MATLAB	C++
16×16	5	1.1 ms	2 ms	**0.165** ms
	1	2.4 ms	2.4	**0.726** ms
32×32	5	1.3 ms	2 ms	**0.242** ms
	1	3.5 ms	2.8	**1.755** ms
32×32	5	1.8 ms	1.9 ms	**1.242** ms
	1	6 ms	**3.9** ms	7.246 ms

Table 4.1: Processing time for the standard Hough transform versus the Hough transform Variant implemented in MATLAB and C++.

The performance of the Non-optimized Hough Variant 'm' file already showed faster performance with theta resolution of 1 degree than the pre-compiled MATLAB Hough function even when excluding the houghlines call required to locate line segments in the image. To evaluate the true performance of the optimized Hough transform Variant, the method was coded in C++ and the timing requirements for processing various window sizes and space resolutions was determined and shown in Table 4.1. Note, the optimized Hough transform Variant was not coded in MATLAB and implemented directly in C++. The reason the C++ method performs slower for larger windows is because MATLAB processes on multiple cores whereas the implemented method only operates on a single core. The true speed improvement of the optimized C++ implemented algorithm is present in the small windows sizes used in this work.

The accuracy of the Hough transform and the Hough transform Variant was determined for small window sizes and shown in Fig. 4.11.

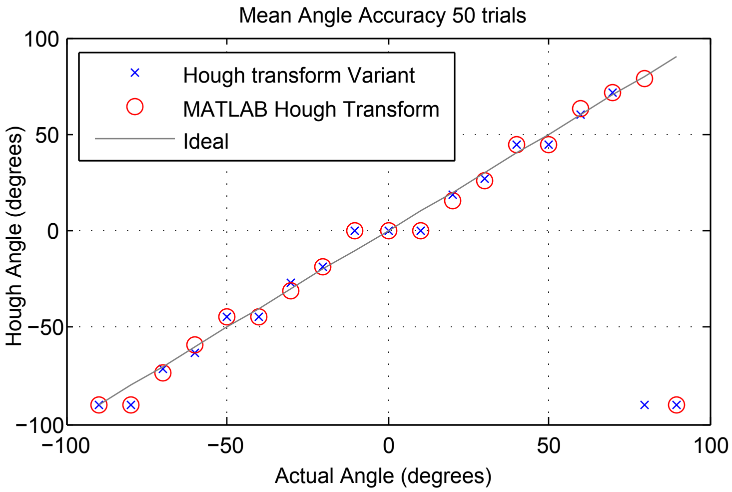

Figure 4.11: Detected line angles for 50 lines at each angle from -90 degrees to 90 degrees in 10 degree increments with 5 pixel noise in a 15×15 window where ρ resolution was 0.25 and θ resolution was 1 degree. Mean processing time in MATLAB was 0.0023 s for the Non-optimized Hough Variant 'm' file and 0.0033 s for the execution of MATLAB functions 'hough' and 'houghpeaks' under these conditions.

Thus, the performance and accuracy of the Hough transform Variant and it's current single core C++ implementation is more than sufficient to be integrated as part of the real-time processing of an M-scan.

4.3.5 Spares M-scan Data Interface Tracing using the Hough Transform Variant

The primary purpose of developing this efficient variant of the Hough transform was to reliably trace the sparse interface of the M-scan image after signal decomposition was performed. Once the M-scan data has been reduced to a sparse form, shown in Fig. 4.12 a), the individual interfaces need to be traced. Of specific interest for the purpose of determining the melting time and precise TOF measurements required for indentation measurement and expulsion prediction of Chapter 3, are the reflection from the upper, lower and faying interface (x_1, x_2 and x_3 respectively.) The Hough transform provides a very robust way of detecting a line through sparse and noisy data, and so, a disjoint interface, or interface contaminated with false reflector locations can still be accurately traced. This is often the case for the lower interface, especially at the melting point.

The starting point of each interface is determined in the time prior to welding. The positions of the reflection are accumulated over the first A-scans and the thee peak of N summed sparse A-scans provides the starting point for each interface. The sparse M-scan data is then segmented by a fixed window size determined by the distance between reflections, such that the end of each window is an offset of the start of the next window. For the range of 2T plate thickness used in practical industry (2 - 6) mm workpieces, the front reflection will never increase in TOF past the start of the faying interface and the same applies for the faying interface with respect to the lower interface.

The segmented windows are each assigned a tracking window. Depending on the size of the segmented windows, the tracking window can range from (5-7) pixels wide by (10-20) samples tall. A common size used in (3-5) mm workpieces is 5×15. This acts as a sliding window that advances through the welding time of the M-scan with each new A-scan (after being decomposed in Section 3.2.) Within this sliding window, the interfaces are approximated by the dominate straight line determined by the Hough Transform above. The actual point on the curve for a given window position is the midpoint of the dominate line in the window.

The window position is then updated for the next A-can by adjusting the vertical position to be centered around the next point on the current detected line. If there is no line present, the window continues to move in the last direction for a set number of steps. If no data is found within a set number of steps, the interface is considered

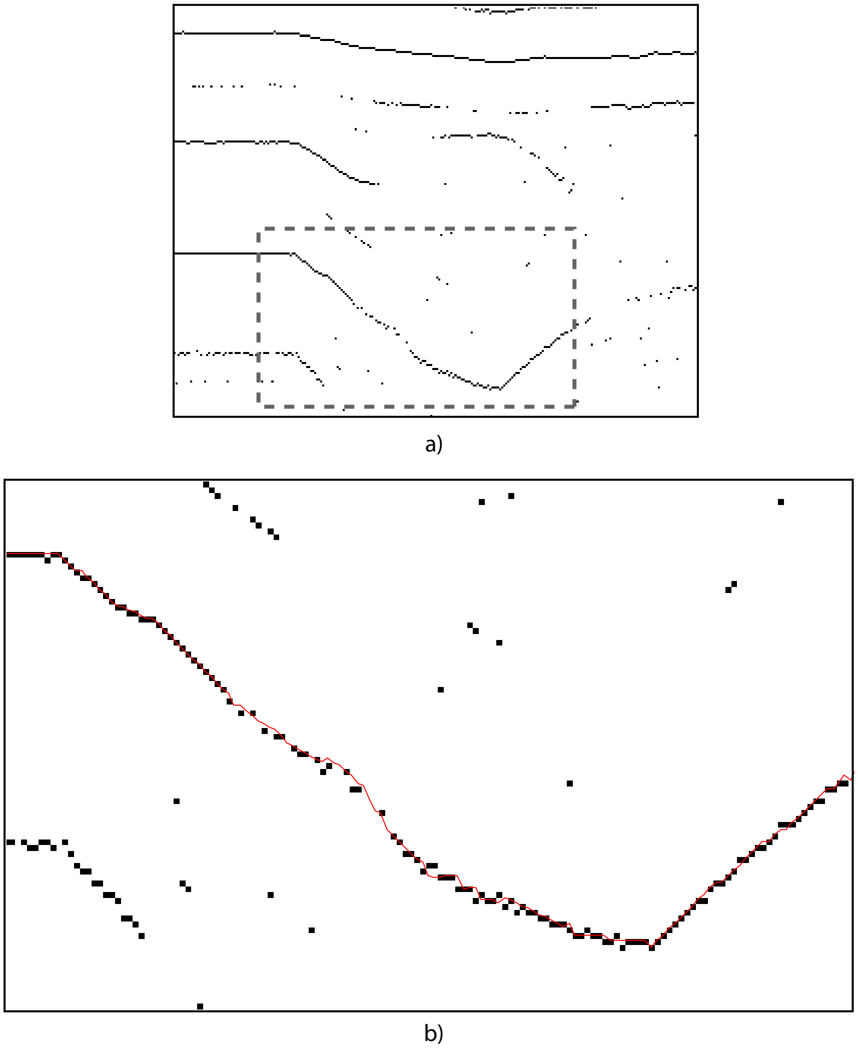

Figure 4.12: a) Sparse M-scan with lower interface segment outlined in a gray dashed box. b) Lower interface traced in the segmented window of a) shown in a thin solid line.

lost and tracing stops. This is often the case for the faying interface as the interface disappears after melting occurs. Occasionally, the lower interface may disappear due to poor contact conditions and can alternatively be used to diagnose a problem with the setup.

Fig. 4.12b) shows the lower interface of a noisy M-scan after the sparse signal decomposition was performed. The interface was tracked with a 5×15 window constrained to the segmented region shown in Fig.4.12a). Even in the disconnected region around the melting point of the workpiece, the interface tracking plots a reasonable estimate of the pulse location with little to no variation from stray pixels.

4.4 Detection of Weak Dynamic Interfaces

One of the more difficult issues to deal with when processing M-scan data is identifying the weak interfaces resulting from the solid steel to liquid nugget interfaces x_4 and x_5. These interfaces are often below the level of noise and overpowered by multiple reflections from the other interfaces. A method to enhance these interfaces was developed to permit tracking the cooling process as was required to measure indentation in Chapter 3.

4.4.1 Removing Undesired Reflection

A strong source of error in the detection of x_4 and x_5 is due to long, overlapping tails from the first interface reflection. An example is shown in Fig. 4.13 a). To counter this effect, Wiener filtering is applied to the A-scan data to remove the tails from the overlapping pulses that obscure the weaker reflections, resulting in Fig. 4.13 b).

4.4.2 Line Detection

After filtering, a directional filter is applied to enhance vertical edges in the B-scan, enhancing the reflections from the low intensity solid steel to liquid nugget interfaces during the cooling process. For simplicity, the Sobel gradient approximation was applied in the horizontal direction. The result is often multiple lines for each interface, corresponding to pulse zero crossings. The effects of both inverse filtering and Sobel

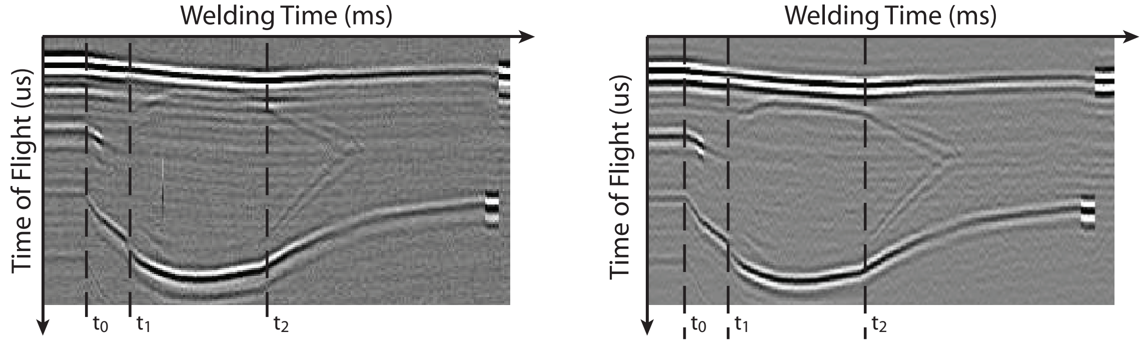

Figure 4.13: Results of Inverse Filtering and M-scan to remove undesired pulse tails and interference before filtering (left) and after filtering (right).

edge enhancement are shown in Fig. 4.14.

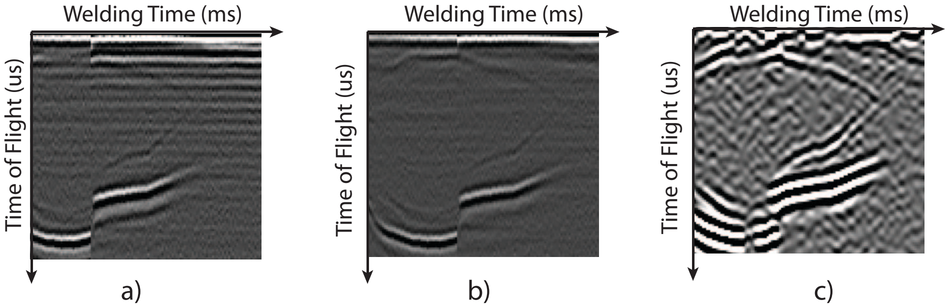

Figure 4.14: The weak solid-liquid nugget reflections after an expulsion are enhanced via inverse filtering and Sobel edge detect. a) M-scan before filtering. b) Result of Wiener filtering. c) Result after horizontal Sobel gradient is applied.

A threshold is then applied to the image at half max, retaining the white and light gray regions of the image. The Hough transform Variant is then applied to the region between the upper and lower interfaces, finding straight lines at the cooling liquid interface reflections. Lines are sorted by angle to correspond with the upper and lower interfaces of the nugget. Multiple lines for a given interface are averaged and extended to identify a point of intersection between both, representing the point in time the weld nugget solidified. Fig. 4.15 shows the result of averaged Hough lines and the ability to locate the solidification time t_{ind}.

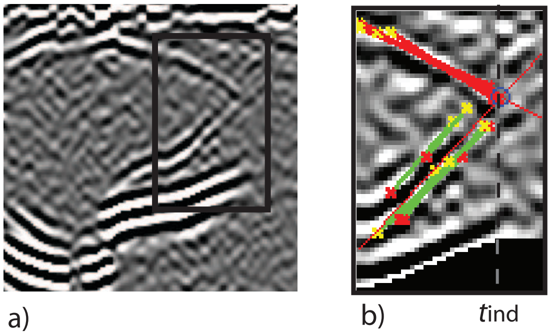

Figure 4.15: a) The interface highlighted by the Sobel gradient and b) the line from the Hough transform Variant. Hough lines are averaged and the intersection point gives the welding time in which indentation can be measured t_{ind}.

The main problem with relying heavily on these interfaces for expulsion detection is that poor acoustic contact with the workpiece due to strong expulsions eliminates the appearance of the interfaces. The main purpose of detecting these interfaces is not to detect expulsion as much as classify the effects of a potentially minor expulsion as explained in Chapter 3, and thus interfaces too weak to detect can be ignored as this is a strong indicator of a move severe event.

4.5 Summary

In this Chapter, four methods of image and signal processing used in the processing of M-scan data were described. The necessity to average and filter A-scan data was demonstrated in Section 4.1. In Section 4.2, a fast method of identifying the interfaces of an M-scan presented. This method used principals of more sophisticated techniques, only optimized the task to be suitable for real-time implementation without loss of performance. Section 4.3 presented a new, fast method of detecting lines in a modified, sorted, hough space. This was developed since the Hough transform was used in multiple parts of this work including interface tracing of Section 4.2 and weak interface detection of Section 4.4. Finally, Section 4.4 demonstrated how very weak, and often hidden, reflections from the liquid nugget could be enhanced by a combination of image and signal processing. Inverse filtering via. a Wiener filter removed the parasitic echoes that overlapped the desired reflection. Edge gradients were then enhanced with a Sobel edge detect, revealing the otherwise invisible reflection. Another application of the Hough transform Variant is used to find lines in these weak reflection, where the intersection point between the average line through x_4 and the average line through x_5 yields the time of solidification in which indentation can be measured using Method 3 of Chapter 3.

References

[1] G. Hayward and J. Lewis, "Comparison of some non-adaptive deconvolution techniques for resolution enhancement of ultrasound data," *Ultrasonics*, vol. 27, pp. 155–164, 1989.

[2] T. Miyashita, H. Schwelick, and W. Kessel, "Recovery of ultrasonic impulse response by spectral extrapolation," in *Acoustical Imaging 14*, 1985, pp. 247–257.

[3] F. Honarvar, H. Sheikhzadeh, M. Moles, and A. N. Sinclair, "Improving the time-resolution and signal-to-noise ratio of ultrasonic nde signals," *Ultrasonics*, vol. 41, pp. 755–763, 2004.

[4] S. K. Sin and C. H. Chen, "A comparison of deconvolution techniques for the ultrasonic non-destructive evaluation of materials," *IEEE Trans. on Image Processing*, vol. 1, no. 1, pp. 3–10, 1992.

[5] S. Dasgupta and R. L. Nowack, "Frequency extrapolation to enhance the deconvolution of transmitted seismic waves," *J. Geophys. Eng.*, vol. 5, pp. 118–127, 2008.

[6] M. Hajian and F. Honarvar, "Reflectivity estimation using an expectation maximization algorithm for ultrasonic testing of adhesive bonds," *Materials Evolution*, pp. 208–219, February 2011.

[7] S. W. Wan, B. I. Raju, and M. A. Srinivasan, "Rhobust deconvolution of high-frequency ultrasound images using higher-order spectral analysis and wavelets," *IEEE Trans. UFFC*, vol. 50, no. 10, pp. 1286–1295, 2003.

[8] T. Olofsson and T. Stepinski, "Minimum entropy deconvolution," *J. Accoust. Soc. Am.*, vol. 109, no. 6, pp. 2831–2839, 2001.

[9] T. Olofsson and E. Wennerstrom, "Sparse deconvolution of b-scan images," *IEEE Trans. UFFC*, vol. 54, no. 8, pp. 1634–1641, 2007.

[10] T. Olofsson, "Semi-sparse deconvolution robust to uncertainties in the impulse responses," *Proc. Ultrasonics Int.*, vol. 42, no. 1-9, pp. 969–975, 2003.

[11] S. Mallat and Z. Zhang, "Matching pursuits with time-frequency dictionaries," *IEEE Trans. Signal Process*, vol. 41, pp. 3397–3415, 1993.

[12] G. Schwarzenberg, M. Weber, T. Hopp, and N. Ruiter, "Model based pulse detection for 3d ultrasound computer tomography," in *IEEE Int. Ultrasonics Symp.*, October 2007, pp. 1255–1258.

[13] J. J. Kormylo and J. M. Mendel, "Maximum likelihood detection and estimation of bernoulli-gaussian processes," *IEEE Trans. Info. Theroy*, vol. 28, no. 3, pp. 482–488, 1982.

[14] R. Demirli and J. Saniie, "Model-based estimation pursuit for sparse decomposition of ultrasonic echoes," *IET Signal Processing*, vol. 6, no. 4, pp. 313–325, 2012.

[15] Y. Lu, R. Demirli, G. Cardoso, and J. Saniie, "A successive parameter estimation algorithm for chirplet signal decomposition," *IEEE Trans. Ultrason. Ferroelectr. Freq. Control*, vol. 53, no. 11, pp. 2121–2131, 2006.

[16] Y. Lu, R. Demirl, G. Cardoso, and J. Saniie, "A comparative study of echo estimation techniques for ultrasonic nde applications," in *IEEE Int. Ultra. Symp.*, October 2006, pp. 436–439.

[17] R. Demirli and J. Saniie, "Model-based estimation of ultrasonic echoes part i: Analysis and algorithms," *IEEE Trans. Ultrason. Ferroelectr. Freq. Control*, vol. 48, no. 3, pp. 787–802, 2001.

[18] J. Lewis, "Fast normalized cross-correlation," Vision Interface, 1995.

[19] S. Mitra and J.F.Kaiser, *Handbook for Digital Signal Processing.* New York: Wiley, 1993.

[20] P. Hough, "Method and means for recognizing lines." US Patent 3 069 654, 1960.

[21] P. Palmer and M. Petrou, "An optimizing line finder using a hough transform," *Computer Vision and Image Understanding*, vol. 67, no. 1, pp. 1–23, 1997.

[22] K. Mayasandra, S. Salehi, W. Wang, and H. Ladak, "A distributed arithmetic hardware architecture for real-time hough-transform-based segmentation," *Can. J. Electr. Comput. Eng.*, vol. 30, no. 4, pp. 201–205, 2005.

[23] M. Albanesi, M. Ferretti, and D. Rizzo, “Benchmarking hough transform architectures for real-time,” *Real-Time Imaging*, vol. 6, no. 2, pp. 155–172, 2000.

[24] L. Lin and V. Jain, “Parallel architectures for computing the hough transform and ct image reconstruction,” in *International Conference on Application Specific Array Processors*, 1994, pp. 152–163.

[25] S. Guo, T. Pridmore, Y. Kong, and X. Zhang, “An improved hough transform voting scheme utilizing surrounded surppression,” *Pattern Recognition Letters*, vol. 30, pp. 1241–1252, 2009.

[26] L. Fernandes and M. Oliveira, “Real-time line detection through an improved hough transform voting scheme,” *Pattern Recognition*, vol. 41, pp. 299–314, 2008.

[27] V. Leavers and M. Sandler, “An efficient radon transform,” in *Proc. 4th Int. Conf. on Pattern Recognition*, 1988, pp. 380–389.

Chapter 5

Expulsion Testing and Results

The current methods of expulsion detection (outlined in Chapter 1) provided at best a vague metric on which expulsion detection was achieved. Many setups biased welding setups towards expulsion where severe expulsions could easily be detected and many works fail to mention the workpiece, weldgun or welding schedules used. Since this work is the first to investigate the problem of expulsion detection using real-time ultrasound evaluation, it is very difficult to compare it directly to current methods, thus, the raw data regarding expulsion detection and classification using Inline ultrasound is presented and the performance with respect to weld quality is discussed. To validate expulsion detection, prediction and classification using ultrasound, results are presented with threshold values for particular setups. These thresholds show that detection, prediction and classification using one or more of the three proposed methods (detailed in Chapter 3) is successful in a wide variety of materials, coatings, workpieces and weld guns.

5.1 Detection by Phase Delay

To assess the effectiveness of expulsion detection by phase delay more than 200 welds were made in the lab using mixed workpieces of 1.2 mm, 1.5 mm and 2.0 mm 2T GA HSS and mild steel plates. All welds were performed with 5/8 inch electrodes each with $d_e = 2$ mm tip face. M-scan data for each weld was recorded at $f_s = 66$ MHz and $t_p = 2$ ms. In each case a transducer with $f_c = 10$ MHz was used. To avoid biasing the results towards severe expulsions, the welding current was varied to produce good welds and welds on the threshold of expulsion, generally a range of (9-11) kA with 12-14 cycles DC current. the electrode was allowed to degrade throughout the process of welding producing both expulsions at lower welding currents and good welds at higher welding currents. Measurements for different workpieces were taken throughout the electrode life. To assess the quality of the welds, the following was performed for each weld completed in the lab.

1. Average diameter measurement via SAM C-scan.
2. Average indentation measurement via. B-Scan.
3. SAM C-scan inspection for voids.
4. Weld thickness measurement via micrometer
5. Nugget diameter measurement via peel test.
6. Expulsion verification via peel test.

The purpose of the redundant physical and SAM measurements was to minimize measurement error. Weld quality was assessed using the industry standards for acceptable nugget diameter given by:

$$d_{\text{nugget}} > 5\sqrt{d_{\text{workpiece}}} \tag{5.1}$$

Expulsion events that appeared in M-scans as minor interface shifts but did not have a reduced nugget diameter where labeled “weak” expulsions. The detection of “weak” expulsions is not relevant as these can result from sputtering of the coating layer, or of very short duration events that have no adverse affect on weld quality with regards to nugget diameter or indentation. The effectiveness of phase delay detection of the upper interface is best displayed as a histogram with the phase delay separated into bins of 0.5×10^{-9} s. This data is shown in Fig. 5.1.

Figure 5.1: Phase delay for expulsions, weak expulsions and no expulsions plotted for 200 welds done in the lab. Results are displayed as a percentage of total welds.

In Fig. 5.1 there is a clear threshold in phase delay between expulsions and no expulsion at 8×10^{-9} s. At the upper limit of phase delay, in the range $> 1.9 \times 10^{-8}$ s, there are a small cluster of weld events that have all been classified and verified as severe expulsions. Thus, another clear threshold at 1.8×10^{-8} exists, suitable for classifying the expulsion event as severe. These welds with severe expulsions not only had a drastically reduced nugget diameter, but also had voids present in the interior of the nugget detectable by the SAM and in some cases visible after peel testing (shown in Chapter 1.) The phase delay technique was then implemented in both Mini-Cooper and Chrysler installations where the M-scans were analyzed in the same manner as the labs scans. The results of this industrial trial are listed in Table 5.1 and compared to the lab results.

Installation	Lab	Mini Cooper	Chrysler CNH
Expulsions	68	135	9
Detected	68	132	9
Missed	0	3	0
False Detected	0	39	1
# of Welds	200	9250	258

Table 5.1: Phase Delay Expulsion Results

The main reason for the false detections present at Mini Cooper is that the current hardware was limited to a PRR of 3.6 ms. As determined in Chapter 3, the maximum PRR should be 2 ms, otherwise the natural heating of the plates could appear as a discontinuity similar to the over heating of the interface detected by phase delay in x_1. In these cases the measured phase delay between two A-scans can be larger than the expulsion threshold but this would likely not be the case at a lower PRR. This is especially evident where Mini Cooper welds with AC current, meaning that this kind of brief overheating not resulting from expulsion is frequently occurring.

The M-scans for missed detections at both Mini Copper and Chrysler WAP showed a phase delay less than the threshold determined by lab scans. This only indicates that either the threshold need to be adjusted for a specific installation due to additional noise or setup parameters, or more likely, the expulsions in these missed detections were weak and the final quality of the weld was not compromised. in this case, these missed detections should not actually be considered as such. Since there was no means of physically assessing the welds, the exact condition remains indeterminate and an area for future investigation.

5.2 Detection by Heating Rate Thresholds

Expulsion detection by heating rate was applied to a series of lab scans to determine if expulsion thresholds could be established for this method, much like phase delay. Unlike phase delay, heating rate thresholds differed for each setup.

A series of welds was made and the heating rate of each was tracked by Method 2 of Chapter 3. Fig. 5.2 shows a few examples of the heating rate curves for 2T 1 mm and 1.8 mm GA HSS plates welded with 3/4” electrodes with tip face $d_e = 6mm$, with welding current varied from (9 - 12) kA. The surface of the electrode was polished after every weld to assure a constant thermal contact conductance coefficient between the electrode and plates. In both Fig. 5.2a and Fig. 5.2b, welds that exhibited an expulsion showed a faster heating rate (shorter melting time) than normal welds, and stick welds showed a slower heating rate (longer melting time) than normal welds. The minimum and maximum welding time for good welds is indicated on the figures.

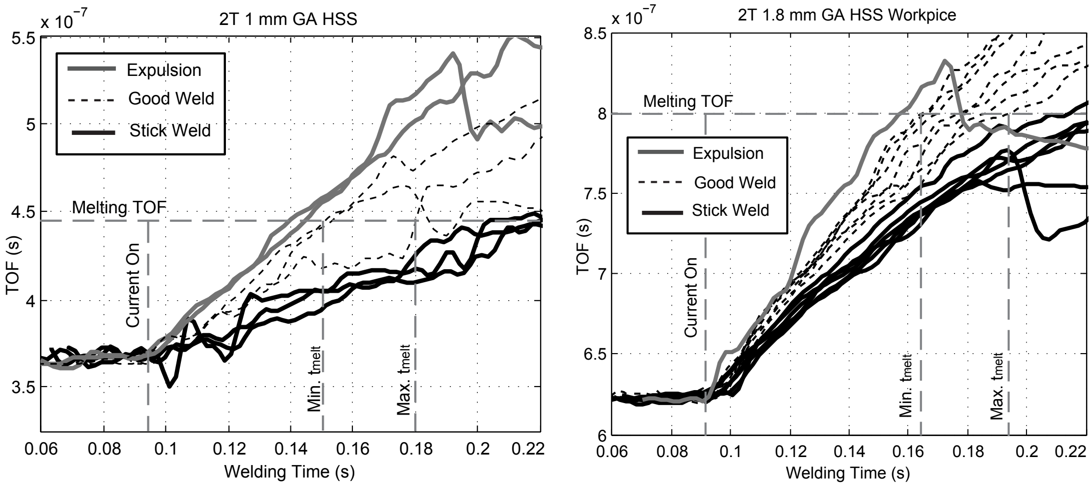

(a)

(b)

Figure 5.2: Heating rates for 1 mm and 1.8 mm 2T workpieces showing expulsions, normal welds and stick welds.

To investigate if similar thresholds were present in other setups, additional materials used by Chrysler and Mini Cooper were also obtained and welded with a similar setup to the welds of Fig. 5.2. The melting time for each, as determined by Method 2, are shown in Fig. 5.3. In all cases, the welding current was controlled to induce expulsions and in all cases, melting time was lower for expulsions than good welds and stick welds (not plotted). This linear separation provides the thresholds for expulsion for each case.

In Fig. 5.3 the melting time was plotted against welding current as the amount of heat generated is a function if I_{weld} squared. The unknown value in all cases is the precises co-efficient of thermal conductivity h_c, which is responsible for differing heating rates at fixed welding currents. The error in melting time for all cases is given by the A-scan PRR of 2 ms, as discussed in Chapter 3.

5.3 Detection by Indentation

An additional investigation was performed to see if severe expulsions (likely resulting from surface expulsions as discussed in Chapter 1), normal expulsions and weak expulsions could be reliably classified by measuring indentation. An additional sixty welds were performed using 1.5 mm and 2 mm GA HSS plates with the same setup as the previous lab scans. The ultrasonically measured indentation was plotted in Fig.5.4a and Fig. 5.4b, and shows a clear distinction in the amount of indentation between good welds and welds with expulsion. Surface expulsions exhibited the greatest amount of indentation over both, but were not always distinguishable from faying interface expulsions.

In all cases, expulsions generated more indentation than normal welds, but classifying weak expulsions from severe expulsions shows no distinct separation and only an industry determined standard regarding an acceptable amount of indentation (such as that presented in Chapter 3), can classify the quality of a weld based on the inden-

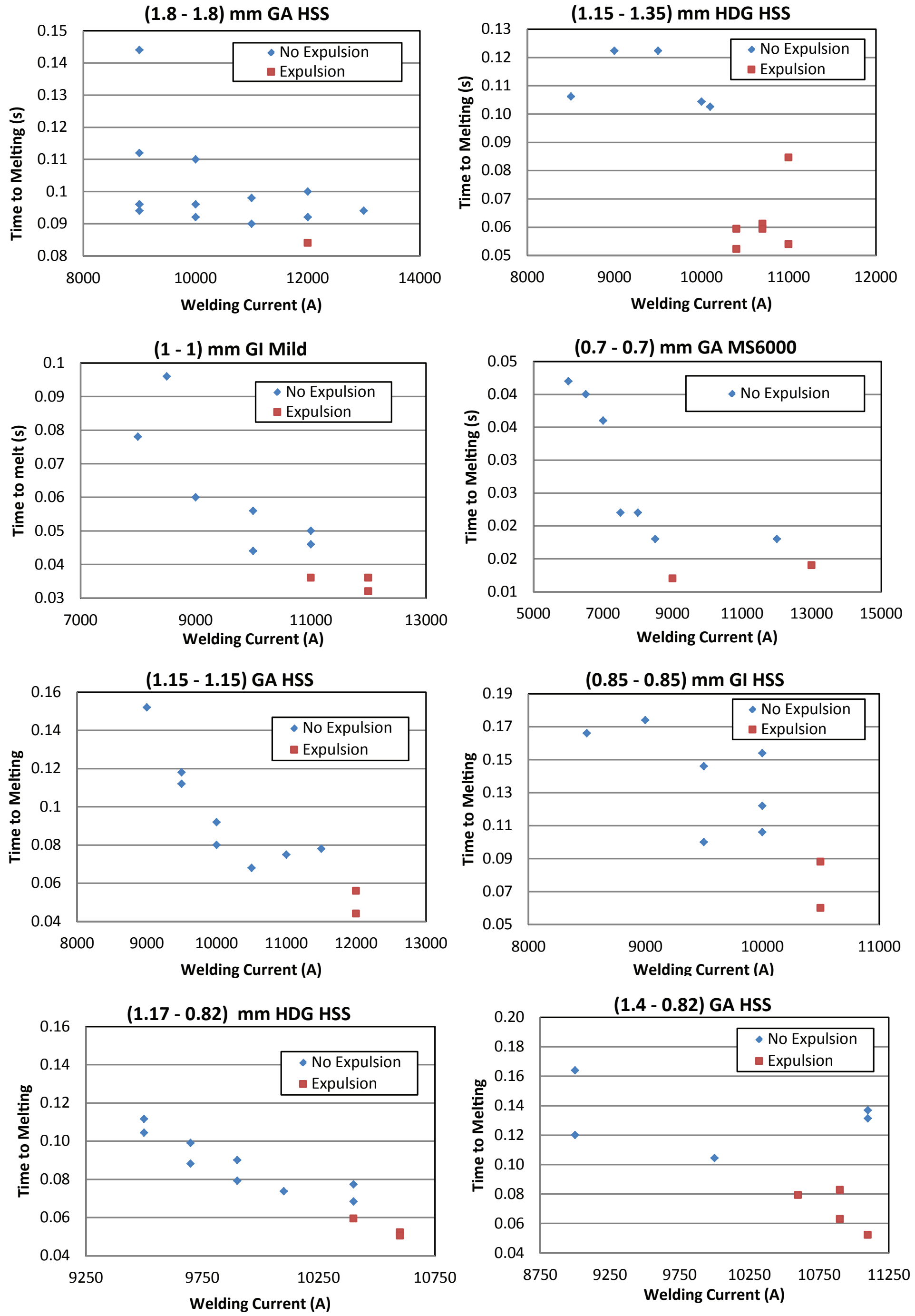

Figure 5.3: Heating rates for various materials and thicknesses.

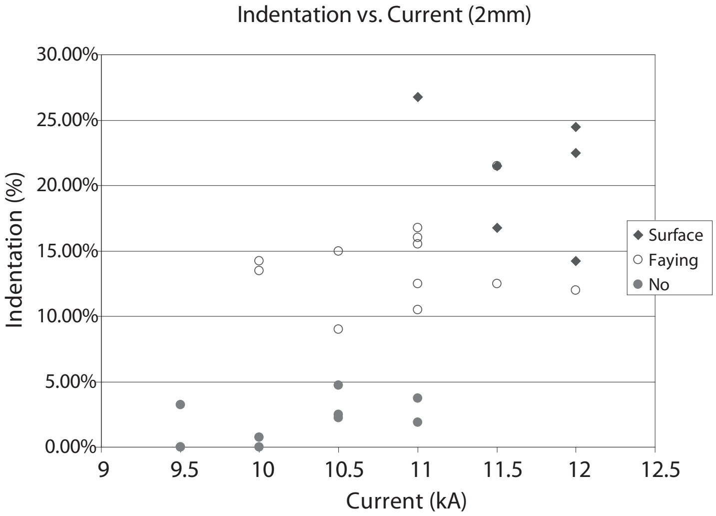

(a) Indentation for 2T 1.5 mm GA HSS plates
at different welding currents.

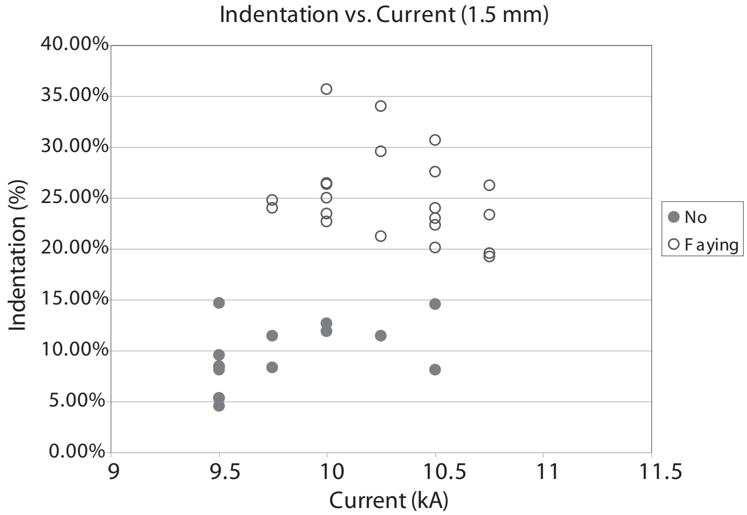

(b) Indentation for 2T 2.0 mm GA HSS plates
at different welding currents.

Figure 5.4: Percentage indentation as determined by Inline ultrasound for different expulsion types in 2T HSS plates. Points are plotted by the type of expulsions that was physically observed.

tation measurement from expulsion. Applying the thresholds of 10% to 2 mm plates and 20% to 1.5 mm plates can indeed separate the weak expulsions from the normal expulsion in terms of indentation. Sill, the best classification for severe expulsions is still given by the change in phase delay generated by the event.

5.4 Conclusion and Future Work

In this work, a very unique approach to expulsion detection of resistance spot welds was investigated. To date, this is the first ultrasonic look at the expulsion event and significant insight into the event and its detection was gained. Three methods for evaluating the ultrasound M-scan of a resistance spot weld were proposed for the detection, prediction and classification of expulsion events based on their effect on weld quality (indentation and nugget diameter.)

The first method relied on phase delay changes of the reflection from the contact between the welding electrode and plate. This phase delay was speculated to result from momentary overheating of the electrode for surface expulsion, but is more likely a result of changes in the non-linear reflection characteristics of the rough contacting surfaces under pressure. The abrupt and instantaneous change in phase delay at the moment of expulsion was found to be a strong indicator that an expulsion event had occurred, however, the detection of weak expulsions by phase delay alone cannot separate weak expulsions from good welds. This is not a concern for NDE since weak expulsions do not have a significant effect on the nugget diameter and weld quality. It was shown in lab scans that even for varying workpiece thicknesses and plate coatings, a threshold was determined that distinguishes expulsions affecting the weld nugget size. In addition, a number of severe expulsions were detected in lab scans that had a detrimental effect on the weld quality, resulting in highly undersized welds and welds that contained large voids and cracks. All of these severe welds showed a phase delay significantly greater than normal expulsion, such that expulsion events could be further classified as normal or severe.

The same phase delay method was applied to M-scans acquired from installations at Chrysler WAP and Mini Cooper and the detection of expulsions via. phase delay showed very promising results. Mini Cooper, however, was unable to acquire M-scan at the required 2 ms PRR and so it appears a number of false detections were made where natural heating fluctuations as a result of AC welding were mistaken as expulsions. This was not observed in DC welding setups or setups operating at the 2 ms PRR such as the impulse welding performed at Chrysler WAP.

The second method predicted the occurrence of expulsion events by ultrasonically monitoring the heating rate of the workpiece. It was reported in literature that overheating is a cause of expulsion and results from high welding currents and/or insufficient heat removal from the workpiece. Cooling of the workpiece is a function of the contact area and more importantly, the thermal contact conductance coefficient h_c, which is likely to vary from weld to weld. This explains how welding with the same setup and same welding current can produce such a variety of different welds, including expulsion events. A simple heating model of the workpiece was derived to work with ultrasonic TOF measurements through the workpiece in order to track the heating of the plates. This model was verified both by plotting the modeled heating curve over the measured heating curve in Chapter 3, and again by matching the predicted and measured time it took to melt a variety of plates. As per theoretical projections, tracking the heating rate of the workpiece to determine the melting time was successful at predicting expulsions since, even for a variety of different plate thicknesses and coatings, an expulsion event resulted when melting time was below a particular threshold. Although this method shows promise for predicting expulsions, it has much greater applications in preventing expulsions and stick welds. Even if the threshold between good welds and expulsions is very narrow for certain setups, tracking the heating rate of the plates and providing feedback to the weld controller has potential to ensure every weld is good. Table 5.2 shows the heating rate thresholds in terms of the melting time for the variety of workpieces and coatings tested in this work that was able to predict 100% of expulsions in each case.

Workpiece	Threshold
(1.8-1.8) mm GA HSS	0.085 s
(1.15-1.35) mm HDG HSS	0.095 s
(1 - 1) mm GI Mild Steel	0.04 s
(0.7-0.7) mm GA MS6000	0.021 s
(1.15-1.15) mm GA HSS	0.06 s
(0.85-0.85) mm GI HSS	0.095 s
(1.7-0.82) mm HDG HSS	0.062 s
(1.4-0.82) mm GA HSS	0.090 s

Table 5.2: The threshold for the time to melting for a variety of workpieces.

In order to ensure that future work using real-time feedback was possible, the ultrasound analysis required to measure heating was performed in an efficient manner such that data could be processed at the desired PRR of 2 ms. A highly efficient sparse signal decomposition technique combined with line tracking via an efficient Hough transform Variant was implemented. The processing time of these methods for a 128 sample A-scan and 5×15 Hough transform Variant window is shown in Table 4.1 of Chapter 4.

Finally, to classify any potential expulsions that are in the weak to normal range by indentation, a method for determining the indentation of the heated workpiece was used. This third method provided a means of detection and classification of expulsion since it was well reported that the amount of indentation has a direct effect of the yield strength of the weld

citexiaoyun1,stocco04. This method was performed after the welding current was removed and traces the weak reflections from the top and bottom of the molten steel nugget to the point where they converge, which indicates the complete solidification of the molten steel. This point was determined in this work to provide precise and highly stable results for the measurement of indentation since the temperature distribution in the workpiece is mostly constant from weld to weld and variation in the temperature distribution does not introduce significant error in the measurement of indentation (reported in Chapter 3.) The TOF through the workpiece was first correlated to the final thickness of the workpiece for a range of indentation resulting from stick welds to expulsions. Finally, a model was proposed for determining the temperature distribution with consideration to thermal expansion and was verified. The results for classifying an expulsion as weak or normal by indentation were presented in Chapter 3 and the indentation results that separate expulsions from normal welds were shown in Fig 5.4.

Overall, the effects the phase delay of ultrasonic reflection can not only be observed, but used to quantify the severity of the event. More significantly, the effects of heat on the speed of sound has allowed the heating rate of the material to be monitored directly by probing the interior of the workpiece during the welding process. This work has now shown that the heating rate is indeed a very strong indicator of the future welds quality. Monitoring this heating rate during welding, especially for the prediction of expulsion, is a novel application for ultrasonic NDE. Finally, indentation resulting from expulsion events can be measured ultrasonically in the heated workpiece despite the effects of thermal expansion, decreased sound speed and indentation on the TOF through the workpiece This provides yet another quality control variable for assessing the effects of expulsion on weld quality.

Although the detection of expulsion in ultrasound M-scans is of substantial value to the existing Inine system's purpose of performing real-time quality control of spot welds, the most significant contributions to future work are: ultrasound monitoring of spot weld heating rates using a suitable heating model and supporting evidence that excessive heating is a primary factor in generating expulsions. Since it was shown that the heating rate can be accurately monitored using the Inline device in a real-time manner, the next natural step is to use the device as a means of providing real-time feedback to the weld controller. The implication is that 100% of expulsions can be eliminated using this kind of feed-back system. The distinction in heating curves between expulsions and stick welds, demonstrated in this dissertation, is evidence that real-time feedback based on ultrasound monitoring of the internal heat generation in the workpiece is indeed possible and should definitely be an avenue explored in future research.

Vita Auctoris

Anthony Christopher Karloff was born in Windsor, Ontario, Canada in 1982. He received his B.A.Sc. and M.A.Sc Degree in Electrical Engineering in 2006 and 2008 respectively from the University of Windsor, Windsor, ON. His masters work involved the design, build and testing of a compact, low-cost and high-speed digital camera with an embedded image processing unit for the quality inspection of two-part gelatin pill capsules. This work was awarded the ITAC Industrial Collaboration Award (Canada wide) by CMC Microsystems at the 2009 Annual Symposium.

Anthony is currently a Ph.D. candidate in the Department of Electrical and Computer Engineering at the University of Windsor. His is working under the supervision of Dr. Roman Maev in the Department of Physics in collaboration with Chrysler Canada, the Institute of Diagnostic Imaging Research (IDIR) and Tessonics Inc., researching real-time ultrasonic monitoring of the resistive spot welding process for quality control and system feedback. This work focuses on high-speed ultrasound imaging using single element and array transducers, development and implementation of real-time image and signal processing algorithms, and hardware and system design for integration into industrial welding environments.